Measurement of the top quark mass in the fully hadronic top antitop decay channel with the ATLAS detector

vorgelegt von

Stefanie Adomeit

geboren in Erding

München, den 1.7.2013

Erstgutachter: Prof. Dr. Otmar Biebel
Zweitgutachter: Prof. Dr. Wolfgang Dünnweber

Tag der mündlichen Prüfung: 30.07.2013

Zusammenfassung

In dieser Arbeit wird eine Messung der Top-Quark Masse im vollhadronischen Top-Antitop Zerfallskanal präsentiert. Die Messung basiert auf Daten des ATLAS Detektors aus Proton-Proton Kollisionen, welche am LHC bei einer Schwerpunktsenergie von $\sqrt{s} = 7$ TeV durchgeführt wurde. Der Datensatz wurde im Jahr 2011 aufgezeichnet und entspricht einer integrierten Luminosität von 4.7 fb^{-1}. Die Messung der Top-Quark Masse erfolgt mittels einer Template-Technik, wobei die sogenannte $R_{3/2}$ Variable als Top-Quark-Massen sensitive Größe benutzt wird. Die $R_{3/2}$ Variable errechnet sich hierbei aus dem Verhältnis der invarianten Massen des hadronisch zerfallenden Top-Quarks und W-Bosons. Die Zuordnung von Jets zu den jeweiligen $t\bar{t}$ Zerfalls-Partonen ergibt sich anhand einer Wahrscheinlichkeitsvorhersage, welche die kinematischen Eigenschaften der Jets berücksichtigt. Der Multijet Untergrund des vollhadronischen $t\bar{t}$ Signals wird mittels Daten abgeschätzt, wodurch eine präzise Vorhersage der kinematischen Verteilungen von Untergrund-Ereignissen ermöglicht wird. Die Messung der Top-Quark Masse ergibt

$$\text{m}_{top} = 175.1 \pm 1.4 \text{ (stat.)} \pm 1.8 \text{ (syst.) GeV/c}^2 \ ,$$

wobei die dominanten Beiträge zur systematischen Unsicherheit von der Jet-Energie-Skala sowie von der b-Jet-Energie-Skala stammen.

Abstract

A measurement of the top quark mass in the fully hadronic top-antitop decay channel is presented. The measurement uses data recorded with the ATLAS detector from proton-proton collisions provided by the LHC in 2011. The data were taken at a centre-of-mass energy of $\sqrt{s} = 7$ TeV and correspond to an integrated luminosity of about 4.7 fb^{-1}. To measure the top quark mass a template technique is used, based on the so-called $R_{3/2}$ estimator which is built from the invariant mass ratio of the hadronically decaying top quarks and W bosons. A kinematic likelihood fit is performed to properly reconstruct the $t\bar{t}$ decay. The multijet background to the fully hadronic $t\bar{t}$ signal is modelled from data by means of an ABCD method, allowing for a precise prediction of kinematical distributions in background events. The top quark mass is measured to be

$$m_{top} = 175.1 \pm 1.4 \text{ (stat.)} \pm 1.8 \text{ (syst.) GeV/c}^2 \ ,$$

with the dominant sources of systematic uncertainty coming from the jet energy scale and the residual b-jet energy scale.

Contents

1. Introduction

Since its development in the second half of the 20th century the Standard Model of elementary particle physics has remarkably contributed to the understanding of the fundamental structure of matter. It has predicted a wide range of phenomena, nearly all of which have been validated and confirmed by means of particle physics experiments. Even though the Standard Model leaves certain unresolved issues, such as the dark matter problem, all attempts to find deviations from its predictions have failed so far.

The remarkable achievements in elementary particle physics during the last 50 years are closely connected to the interplay of theory predictions and particle physics experiments. To test the predictions of the Standard Model and to search for signatures of new physics particle accelerators have been built. Between 2010 and 2012 the Large Hadron Collider at CERN has delivered proton-proton collisions at a centre-of-mass energy of 7 and 8 TeV, allowing to probe the Standard Model at energy scales never reached before. Four detectors are located at the LHC collision points, one of them being the multi-purpose detector ATLAS (A Toroidal LHC ApparatuS).

The analysis presented in this thesis is focused on the measurement of the top quark mass in the fully hadronic $t\bar{t}$ channel, using $\sqrt{s} = 7$ TeV collision data recorded with the ATLAS detector during 2011. Studying the top quark properties is a fundamental task at the LHC. The large top quark production cross section at LHC centre-of-mass energies provides excellent statistical conditions to repeat and complement the measurements in the top quark sector carried out so far at Tevatron, where the top quark was discovered only 18 years ago [1, 2]. Besides its short lifetime – allowing to study the top quark and its properties more precisely via its decay products compared to any of the other quarks which are permanently bound into hadrons – the top quark also plays an important role in studies involving the recently discovered Higgs boson [3, 4]. Not only is $t\bar{t}$ production a major background to various Higgs analyses, its large Yukawa coupling close to unity makes the top quark itself an important tool in shedding light on the mechanism of spontaneous electroweak symmetry breaking. Various theoretical calculations in the Higgs boson sector heavily rely on the top quark mass. As outlined in [5], experimental results on the Higgs boson and top quark masses – together with the strong coupling constant α_s – are, for instance, a critical input to theoretical predictions on the electroweak vacuum (in)stability. The measurement of the top quark mass in the fully hadronic $t\bar{t}$ channel does not only provide a cross check of its equivalent measurements in the lepton+jets and dilepton channels, it moreover provides input to the combination of top quark mass results obtained in the various $t\bar{t}$ decay channels allowing for an increased overall precision.

The analysis presented in this thesis makes use of the $R_{3/2}$ variable for the top quark mass measurement. It is defined as the ratio of the invariant masses of the top quark and the W boson stemming from the electroweak top quark decay. The $R_{3/2}$ variable has been shown to be sensitive to the top quark mass, while its sensitivity to variations in the jet energy scale – one of the major sources of systematic uncertainty contributing to the top quark mass measurement – is reduced due to the usage of the invariant mass ratio. A template technique is applied to measure the top quark mass in the data. Special focus is set on the modelling of multijet background events, which is one of the major challenges when analysing fully hadronic $t\bar{t}$ events. A data-driven technique is applied to extract the background shapes as well as the expected background normalisation.

A brief introduction into the Standard Model of particle physics is given in Chapter 2, followed by an overview over the ATLAS detector and its subsystems in Chapter 3. The reconstruction of physics objects from detector measurements is outlined in Chapter 4, together with the quality criteria imposed on the reconstructed object candidates. Also discussed are the event selection criteria applied to discriminate the fully hadronic $t\bar{t}$ signal from background events. The modelling of signal and background events is detailed in Chapter 5, followed by validation studies based on data to background+signal model comparison studies, see Chapter 6. The $R_{3/2}$ variable together with the template method used to extract the top quark mass are discussed in Chapter 7. In addition, the kinematical likelihood fit used to reconstruct the fully hadronic $t\bar{t}$ decay topology is explained. Chapters 8 and 9 give an overview over the sources of systematic uncertainties affecting the top quark mass measurement. Finally, the results are summarised in Chapter 10.

2. Theoretical framework

2.1. The Standard Model of elementary particle physics

In the framework of the Standard Model of elementary particle physics [6–12] all matter is built from elementary spin $\frac{1}{2}$ fermions. Those fermions occur in three generations. Within each generation there are two quarks - one up-type and one down-type quark - as well as one charged lepton and its corresponding neutrino. In quantum field theory each of the fermions is represented by a field ψ. Local gauge invariance requires the Standard Model Lagrangian to remain invariant when transforming the fermion fields in the following manner:

$$\psi \rightarrow \psi \exp(-i\alpha^j(x)f^j). \tag{2.1}$$

This principle is only valid in the presence of (massless) fields which transform in the same manner as the fermion fields thus compensating the fermion field transformations in each point of space and time. Based on the choice of the local gauge symmetry group the strong and electroweak interaction theories emerge - introducing a set of bosonic particles intermediating the corresponding forces. Following Noether's theorem, each symmetry group introduces field-charges which are conserved under local gauge transfromation. An overview over the Standard model particles and their properties is given in figure 2.1.

2.1.1. Electroweak interaction theory

The unified theory of electromagnetic and weak interactions is based on the $SU(2)_L \times U(1)$ symmetry group. In the framework of the weak interaction theory fermions are arranged in left-handed doublets with respect to the third component of the weak field charge - the weak isospin:

$$\begin{pmatrix} \nu_e \\ e^- \end{pmatrix}_L, \begin{pmatrix} \nu_\mu \\ \mu^- \end{pmatrix}_L, \begin{pmatrix} \nu_\tau \\ \tau^- \end{pmatrix}_L, \begin{pmatrix} u \\ d' \end{pmatrix}_L, \begin{pmatrix} c \\ s' \end{pmatrix}_L, \begin{pmatrix} t \\ b' \end{pmatrix}_L$$

where d', s' and b' denote superposition states of the (left handed) quarks [1]. The Cabibbo-Kobayashi-Maskawa Matrix connects these superposition states to the single quarks via:

---

[1]Flavour mixing also occurs in the lepton sector in the case of non-zero neutrino masses. In its original formulation the Standard Model assumes neutrinos to be massless. Experiments with solar, atmospheric, reactor and accelerator neutrinos, however, have provided evidence for oscillations of neutrinos as a result of non-zero neutrino masses. A summary on neutrino oscillation measurements can be found in [14].
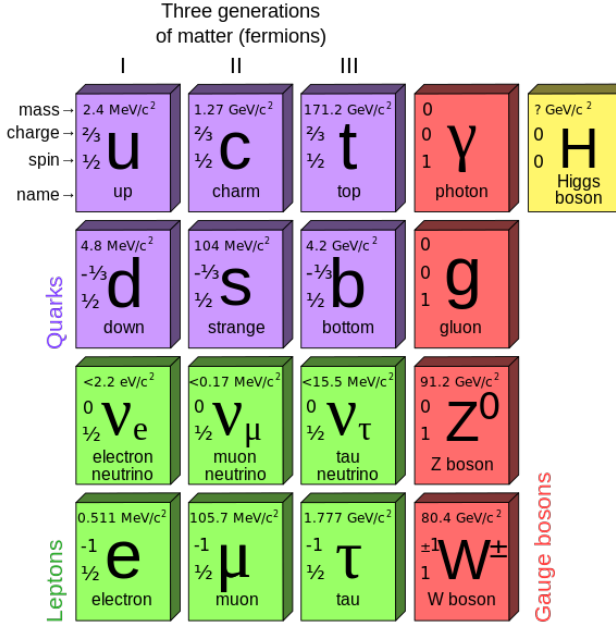
Figure 2.1.: The elementary particles of the Standard Model: shown are the tree genera-
tions of fermions, including one up-type and one down-type quark as well as
one charged lepton and its corresponding neutrino. The gauge bosons inter-
mediating the fundamental forces are shown in the fourth column, as well as
the Higgs boson. Taken from [13]

$$\begin{pmatrix} d' \\ s' \\ b' \end{pmatrix} = \begin{pmatrix} V_{ud} & V_{us} & V_{ub} \\ V_{cd} & V_{cs} & V_{cb} \\ V_{td} & V_{ts} & V_{tb} \end{pmatrix}_{CKM} \begin{pmatrix} d \\ s \\ b \end{pmatrix}. \tag{2.2}$$

Right handed fermions do not couple to charged weak currents which transform fermions
into their isospin partner. These are hence represented by isospin singlets:

$$e_R^-, \mu_R^-, \tau_R^-, u_R, d_R, s_R, c_R, t_R, b_R.$$

$SU(2)_L$ transformations with respect to the weak isospin require the presence of 3 com-
pensating massless vector boson fields - W_1^μ, W_2^μ and W_3^μ - ensuring the invariance of
the electoweak Lagrangian density. $U(1)$ transformations with respect to the weak hyper-
charge Y give rise to a fourth massless vector field B^μ, where the hypercharge is connected
to the weak isospin via the Gell-Mann-Nishijima relation:

$$Q = I_3 + Y/2. \tag{2.3}$$

The physical observable vector bosons $W^{(\pm)\mu}$, Z^μ and the photon A^μ can be written as
linear combination of the gauge fields $\mathbf{W}^\mu = (W_1^\mu, W_2^\mu, W_3^\mu)$ and B^μ:

$$W^{(\mp)\mu} = \frac{1}{\sqrt{2}} \left(W_1^\mu \pm i W_2^\mu \right) \tag{2.4}$$

$$Z^\mu = -B^\mu \sin \theta_W + W_3^\mu \cos \theta_W \tag{2.5}$$

$$A^\mu = B^\mu \cos \theta_W + W_3^\mu \sin \theta_W \tag{2.6}$$

with the weak mixing angle θ_W which is connected to the weak charges g and g' and the electric charge e via:

$$\tan \theta_W = \frac{g'}{g} \tag{2.7}$$

$$e = g \sin \theta_W. \tag{2.8}$$

Local gauge invariance, however, requires the presence of **massless** fields which is opposed to the experimentally observed massive vector bosons $W^\pm$ and Z. Also, the fermions need to be massless as mass terms in the electroweak Lagrangian combine left and right handed states. A solution is provided via the Englert-Brout-Higgs-Guralnik-Hagen-Kibble mechanism [15–18] where an additional isospin doublet of scalar fields is introduced:

$$\phi = \begin{pmatrix} \phi^+ \\ \phi^0 \end{pmatrix} = \begin{pmatrix} \phi_1^+ + i\phi_2^+ \\ \phi_3^0 + i\phi_4^0 \end{pmatrix} \tag{2.9}$$

with vacuum expectation values

$$\langle \phi^+ \rangle = 0 \text{ and } \langle \phi^0 \rangle = v \neq 0, {}^2 \tag{2.10}$$

where the non-zero expectation value of ϕ^0 has its origin in the self-coupling of the Higgs field. Expanding the Higgs potential around the minimum yields

$$\phi(x) \propto \begin{pmatrix} 0 + \eta^+(x) + i\zeta^+(x) \\ v + \eta^0(x) + i\zeta^0(x) \end{pmatrix}. \tag{2.11}$$

The $\eta^+(x)$, $\zeta^+(x)$ and $\zeta^0(x)$ fields result in massless Goldstone bosons, which, after gauge transformation, are absorbed into the longitudinal components of the massive vector boson fields. Finally, the remaining field $\eta^0(x)$ represents the (massive) Higgs boson. The masses of the elementary spin $\frac{1}{2}$ fermions are generated based on the Yukawa coupling of the Higgs bosons to the fermions. As an interesting aspect in the light of top quark physics (see Section 2.2) the Yukawa coupling is proportional to the fermion masses themselves: $\widetilde{g}_\mu \sim m$.

In 2012 the ATLAS and CMS experiments at LHC announced the observation a new particle in the mass range 125 - 126 GeV consistent with the Higgs boson [3, 4]. Further measurements [19] are performed to study further the properties of the recently observed boson, which will shed light on the question whether the new particle is consistent with the Standard Model Higgs boson.

---

[2]Photons couple to the charged component of the Higgs field. To make sure the photon remains massless the vacuum expectation value of ϕ^+ is set to 0.

2.1.2. Quantum Chromodynamics

Quantum Chromodynamics (QCD) describes interactions of coloured quarks and gluons. Local $SU(3)_C$ transformations are performed with respect to the 'coloured part' of the quark wave functions - the colour spinors - which can take three different states:

$$\chi_R = \begin{pmatrix} 1 \\ 0 \\ 0 \end{pmatrix}, \chi_G = \begin{pmatrix} 0 \\ 1 \\ 0 \end{pmatrix}, \chi_B = \begin{pmatrix} 0 \\ 0 \\ 1 \end{pmatrix}$$

According to the 8 generators of the $SU(3)_C$ group eight vector fields need to be introduced - represented by the 8 different gluons.

Similar to photons in QED, gluons are massless. When computing scattering cross-sections this leads to divergences for higher order terms. To obtain finite results a **renormalisation** procedure is applied, which introduces counterterms through which these infinities are effectively subtracted. As a consequence, the renormalised parameter gets dependent on the renormalisation scale μ_R^2 and on the scale of the momentum transfer Q^2, resulting in so-called running parameters.

In QCD the renormalised strong coupling constant α_s yields:

$$\alpha_s(Q^2) = \frac{\alpha_s(\mu_R^2)}{1 + \alpha_s(\mu_R^2)\beta_0 \ln(Q^2/\mu_R^2)}, \tag{2.12}$$

where $\beta_0 = \frac{33-2n_f}{12\pi}$ with n_f representing the number of quark flavours. The Q^2 dependence of α_s is illustrated in Figure 2.2.

At large values of Q^2 - or small distance scales -, α_s is small, usually referred to as **asymptotic freedom**. As a consequence, quarks and gluons can be treated as quasi-free particles within hadrons. As $Q^2 \rightarrow \Lambda_{QCD}^2$, perturbative QCD breaks down. Typically, the prescription of those low momentum transfer processes relies on phenomenological models. Based on experimental results it has been found that α_s takes sizeable values at large distance scales, known as **confinement**. Two partons ejected from a hadron through a hard scatter process can therefore not travel arbitrarily large distances. The further the partons move away from each other, the larger the strong force acting on the parton pair. At sufficiently large energies a new parton-antiparton pair is produced. The various partons produced in this process finally recombine to hadrons. Quarks and gluons can therefore not be observed as single particles but will rather initiate collimated showers of particles - so-called **jets** - via **hadronisation** processes.

2.2. Top quark physics

It was only in 1995 that the top quark was directly observed by the DØ and CDF experiments at Tevatron [1, 2]. The discovery of the top quark can be understood as
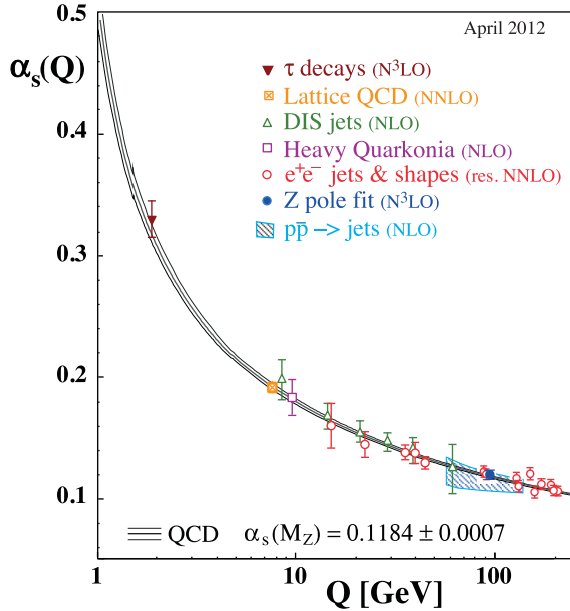
Figure 2.2.: Summary of measurements of α_s as a function of the respective energy scale Q, taken from [14]

great success of the Standard Model, which already anticipated its existence as Q=2/3 and I_3=+1/2 weak-isospin partner of the bottom quark, observed in 1977 [20]. With a mass of about 35 times the *b*-quark mass and a corresponding large width the top quark decays before it is confined into hadrons. As a consequence, information on the top quark properties, such as spin or helicity, can be assessed via its decay products, allowing to study the top quark more precisely than any of the light quarks which are permanently bound in hadrons. Furthermore, the large top quark mass indicates a Yukawa coupling to the Higgs boson close to unity, making the top quark a promising tool in gaining a better understanding of the mechanism of electroweak symmetry breaking. Finally, top quark production is a major background in many searches for physics beyond the Standard Model. A profound understanding of the top quark signal is hence an essential key ingredient to detect new physics processes.

A concise summary on the top quark production and decay as well as on the top quark mass measurement is given in the following sections. For a detailed overview on top quark physics - including measurements involving top quarks - see [21, 22].

2.2.1. Top quark production at LHC

At hadron colliders the dominant fraction of top quarks is produced via the strong interaction - resulting in a short-lived top-antitop pair. In lowest order the $t\bar{t}$ production can be understood as $2 \rightarrow 2$ process, where the outgoing $t\bar{t}$ pair is produced via the hard scatter process involving two of the sea or valence partons of the colliding protons.

For a more detailed view on the strong $t\bar{t}$ production process it is convenient to describe hadron-hadron collisions by means of the factorisation concept which separates short distance (= hard) from long distance (= soft) QCD processes. The short distance process is represented via the hard scattering partonic cross section σ^{ij}, which needs to be specified for all partons of type i and j involved in the scattering process. All short distance processes are factorised into parton distribution functions (PDFs) $f_i(x_i, \mu_F^2)$. PDFs can be understood as probability density function to observe a parton of type i carrying the momentum fraction x_i of the incoming hadron when evaluated at a certain factorisation scale μ_F. Since PDFs represent soft, non-perturbative processes they need to be extracted from global fits to deep inelastic scattering, Drell-Yan and other data. Combining soft and hard processes the overall production cross-section for a final state AB=$t\bar{t}$ can be written as:

$$\sigma^{t\bar{t}} = \sum_{i,j} \int dx_i dx_j f_i\left(x_i, \mu_F^2\right) \bar{f}_j\left(x_j, \mu_F^2\right) \times \left[\sigma_0 + \alpha_s(\mu_R^2)\sigma_1 + ...\right]_{ij \to t\bar{t}} \tag{2.13}$$

where $\sum_{i,j}$ denotes the sum over all parton pairs.

The dependence on the normalisation and factorisation scale parameters μ_R and μ_F in formula 2.13 remains when truncating the perturbation series expansion at a given order [3]. Usually, the scale dependence of the cross section is parameterized using one common value $\mu_R^2 = \mu_F^2 = Q^2$ which is typically chosen to be in the order of the momentum scale of the hard scatter.

To produce a $t\bar{t}$ pair at rest, the momentum fraction carried by both partons involved in the hard scatter must exceed

$$x_i x_j \geq 4m_{top}^2/s. \tag{2.14}$$

Assuming $x_i \approx x_j$ yields $x \approx 0.05$ using $m_{top} = 175$ GeV and $\sqrt{s} = 7$ TeV. As demonstrated in Figure 2.3 this low x-region is highly dominated by gluons. The major fraction of $t\bar{t}$ pairs at LHC is hence produced via gluon-gluon fusion, while only $\approx 20\%$ of the top pairs originate from quark-antiquark annihilation (see Figure 2.4), whereas the latter only exist as sea quarks within the colliding protons at LHC. The $t\bar{t}$ production cross-section in pp collisions at $\sqrt{s} = 7$ TeV calculated at NLO order yields ≈ 165 pb (see Section 5.1) [4].

---

[3]The cross section dependence on the scale parameters gets weaker as more higher order terms get included into the perturbation series and finally gets invariant on changes in μ_F and μ_R when calculated to all orders in perturbation theory. Hence, truncating the perturbation series at a given order yields different results for different choices of the scale parameters - reflecting the uncertainty on the cross section due to the lack of higher order corrections.

[4]The number is based on the world average top quark mass of 172.5 GeV
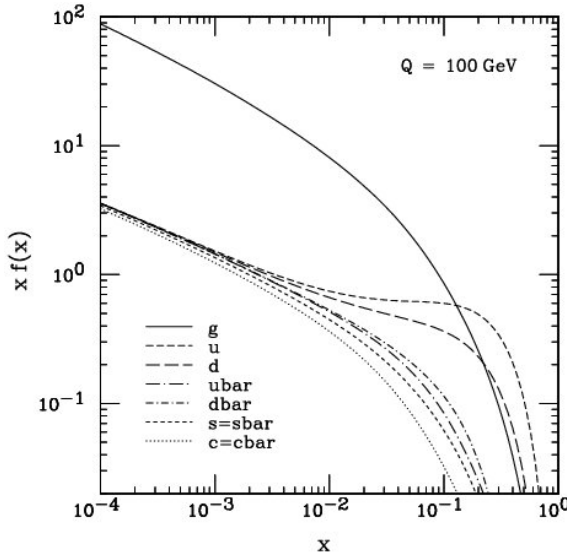
Figure 2.3.: CTEQ6M parton distribution functions at Q = 100 GeV, taken from [23]
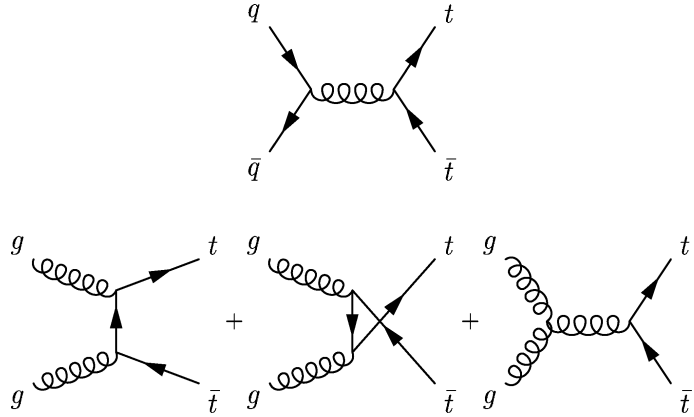
Figure 2.4.: LO Feynman diagrams for $t\bar{t}$ production via the strong interaction through gluon-gluon fusion (bottom) and quark-antiquark annihilation (top), taken from [21].

Besides the strong top-pair production, electroweak processes can give rise to the production of single top quarks. Single top quark production occurs via three processes: W-gluon fusion (t-channel production), quark-antiquark annihilation (s-channel production) and Wt-production, shown in Figure 2.5. The single top quark production cross sections have been measured with $\sqrt{s}$ =7 TeV data in ATLAS to be 83±20 pb [24] (t-channel), < 26.5 pb [25] (s-channel) and 17±6 pb [26] (Wt-production). All three single top production cross sections are proportional to $|V_{tb}|^2$, allowing for a direct measurement of the CKM matrix element $|V_{tb}|$.
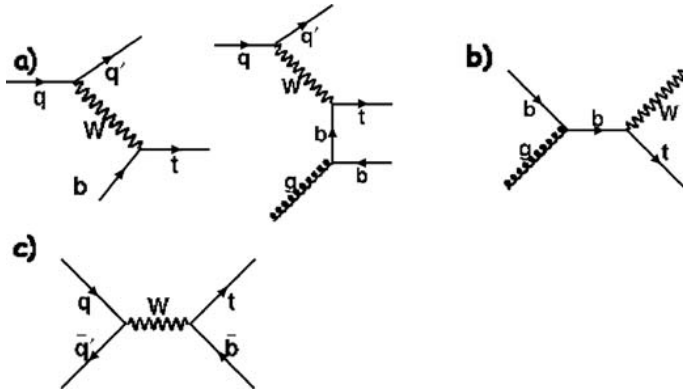
Figure 2.5.: Feynman diagrams for the electroweak single top quark production: t-channel (a), Wt production (b) and s-channel (c), taken from [21].

2.2.2. Top quark decay

Due to its large width of $\Gamma \approx 1.7$ GeV, which is about an order of magnitude larger than the strong-interaction energy scale $\Lambda_{QCD} \approx 200$ MeV, the top quark decays before being confined into hadrons. The top quark decay - driven by electroweak processes - almost exclusively occurs via the $t \to Wb$ channel. Final states including light quarks - namely $t \to Ws$ and $t \to Wd$ - are suppressed by the square of the corresponding CKM matrix elements $|V_{ts}|$ and $|V_{td}|$ with respect to $|V_{tb}|$. Depending on the consecutive W-boson decay, $t\bar{t}$ final states can be categorised as follows:

1. fully hadronic / all-jets channel: $t\bar{t} \to W^+bW^-\bar{b} \to q\bar{q}'bq''\bar{q}'''\bar{b}$

2. lepton+jets channel: $t\bar{t} \to W^+bW^-\bar{b} \to q\bar{q}'bl\bar{\nu}_l\bar{b}(q\bar{q}'\bar{b}\bar{l}\nu_l b)$

3. dilepton channel: $t\bar{t} \to W^+bW^-\bar{b} \to \bar{l}\nu_l bl\bar{\nu}_l\bar{b}$

Based on the leading order W-decay scenario - resulting in 1/3 leptonic and 2/3 hadronic final states - the largest branching fraction is expected for fully hadronic decays (46.2%), while the lepton+jets and dilepton branching ratios yield 43.5% and 10.3% [5].

The lepton + jets channel is often referred to as 'golden channel', providing the best trade-off in terms of a pure signal signature and a reasonable branching ratio among all channels. Similarly, a good separation with respect to background processes is given in the dilepton channel. However, due to the neutrinos involved in the leptonic W-decays, the top invariant mass spectrum cannot be reconstructed directly in this channel. Fully hadronic $t\bar{t}$ final states occur most frequently with respect to all decay channels and, combined with the large $t\bar{t}$ cross section, provide excellent statistical conditions for measurements. The large challenge is related to the fully hadronic decay signature of at least

---

[5]Typically, when analysing $t\bar{t}$ final states including leptons only the e and μ channels are considered - hence, to obtain the branching ratio of effectively analysed $t\bar{t}$ final states the numbers must be corrected for the contribution of τ decays.

6 jets [6], resulting in a large contribution of multi-jet background events. Hence, one of the major tasks when analysing fully hadronic $t\bar{t}$ events is the precise understanding and modelling of background processes.

2.2.3. Top quark mass

In the electroweak theory the top quark is involved in higher order loop diagrams, making the top quark mass a fundamental parameter of the Standard Model. Precise measurements of the top quark mass are thus an important tool to gain a better understanding of the mechanism leading to electroweak symmetry breaking. Together with other parameters of the electroweak theory the top quark mass can, for instance, provide indirect constraints on the mass of the Higgs boson.

Within field theory the definition of mass is scale dependent. Strictly speaking, the so-called pole-mass scheme is only applicable to particles travelling asymptotic large distances, such as leptons. Quarks, however, are typically confined into hadrons so the pole-mass concept is not really well-defined in this case resulting in an ambiguity of $\mathcal{O}(\Lambda_{QCD})$ introduced by soft, non-perturbative effects, see [27]. Accounting for the short distance behaviour of QCD one can turn to other renormalisation schemes, where the $\overline{MS}$-scheme is most commonly used, introducing the scale dependent, running $m_{top}^{\overline{MS}}(\mu_R)$ quark mass into the QCD Lagrangian.

As outlined in section 2.2.2, the top quark decays before being bound into hadrons. Accordingly, the most natural way of measuring the top quark mass is by means of the invariant mass distribution of its decay products [7]. The question on whether this corresponds to either the top quark pole mass or its $\overline{MS}$ mass is closely connected to the Monte-Carlo top quark mass - m_{top}^{MC} - to which the measurement is calibrated. Due to the use of parton shower MCs at leading logarithmic order no direct connection between m_{top}^{MC} and either of the two mass schemes can be done a priori. [28] uses higher-order QCD calculations to extract the top quark mass from the $t\bar{t}$ cross section in the lepton + jets channel. The extracted top quark pole mass and $\overline{MS}$ mass are compared to the top quark mass obtained from direct measurements showing that m_{top}^{MC} can be identified with the pole mass within 1 GeV.

---

[6]Initial and final state quarks can radiate gluons giving rise to additional jets.

[7]In that sense the large top quark width can be seen as infrared cutoff which somewhat lowers the influence of non-perturbative effects due to the lack of hadronisation and makes the pole-mass concept reasonable for top quarks.

3. Experimental setup

3.1. The Large Hadron Collider

The Large Hadron Collider (LHC) [29, 30], situated at the European Organization for Nuclear Research (CERN) near Geneva, is the largest particle accelerator in the world. It is installed in a tunnel of 27 km diameter at the Swiss-French border which was previously used by the LEP collider.

Being a synchrotron like accelerator the LHC is designed to collide two counter-rotating beams of either protons or heavy ions. Proton beams are delivered by the CERN accelerator chain at an injection energy of 450 GeV and are further accelerated by radio frequency cavities while circulating in two separate vacuum tubes installed in the LHC beam pipe. The protons, which are bundeled in bunches within each beam, are bent on a circular trajectory of constant radius by 1232 dipole magnets and are focused by quadrupole magnets at the so-called collision points.

Four experiments have been designed for the LHC with detectors installed at the different interaction points: the two special purpose detectors ALICE (A Large Ion Collider Experiment) [31] and LHCb (LHC beauty) [32] as well as the two multi-purpose detectors CMS (Compact Muon Solenoid) [33] and ATLAS (A Toroidal LHC ApparatuS) [34]. While ALICE and LHCb are designed to study heavy-ion collisions and to examine *b*-hadron decays, respectively, ATLAS and CMS have wide physics programs including precise (Standard Model) measurements as well as searches for signatures of new physics such as the Higgs boson and supersymmetry.

The LHC is designed to accelerate proton beams up to an energy of 7 TeV before bringing them to collision at a centre-of-mass energy of 14 TeV. However, after the incident of September 19th 2009, caused by a faulty electrical connection between two of the accelerators magnets [35], the LHC was operated at a reduced centre-of-mass energy of 7 TeV in 2010 and 2011 and 8 TeV in 2012, where the data used for the measurement presented in this thesis were recorded in 2011.

3.2. The ATLAS detector

The ATLAS detector, located at the interaction point 1 of the LHC ring, and its subsystems are illustrated in Figure 3.1. A brief summary on the ATLAS subdetectors is presented in this section.
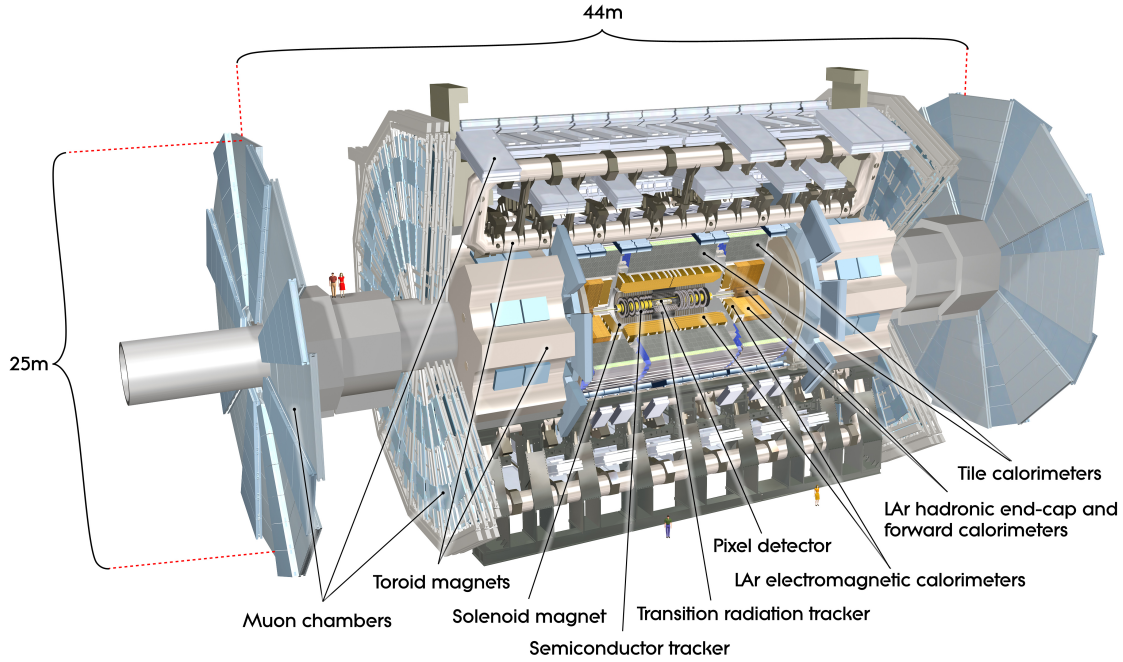
Figure 3.1.: Computer-generated image of the ATLAS detector and its subsystems [36].

The coordinate system of ATLAS is a right-handed coordinate system, with the x-axis pointing towards the centre of the LHC ring, the y-axis pointing upwards and the z-axis following the beam pipe. The origin of the ATLAS coordinate system corresponds to the (nominal) interaction point in the centre of the detector. Cylindrical coordinates are used, where ϕ is the azimuth angle around the beam pipe in the x-y plane. The pseudorapidity is defined as $\eta = -\ln\tan\theta/2$, with θ being the polar angle.

3.2.1. The ATLAS inner detector system

The ATLAS inner detector comprises three subsystems (Figure 3.2) which are located in a 2 T magnetic field generated by a superconducting solenoidal magnet. All three subsystems cover a pseudorapidity region of $|\eta| < 2.5$. The inner detector is designed to precisely locate interaction and displaced decay vertices as well as to provide momentum measurement of charged particles.

Closest to the interaction point is the pixel detector. It consists of three layers of silicon sensors in the barrel region which are arranged in concentrical cylinders at 5 cm, 9 cm and 12 cm from the centre of the beam axis. In the endcap region, three discs of silicon sensors are installed. The pixel detector has a spatial resolution up to 12 μm allowing to precisely measure the interaction vertex as well as displaced vertices from long-lived particles. Similar to the pixel detector, the silicon strip detector (SCT) consists of silicon semiconductors. To cover a larger region long strips are used instead of pixel sensors
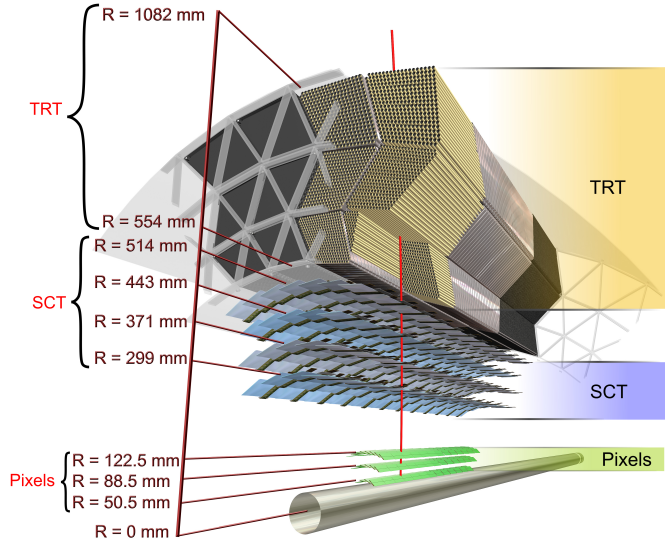
Figure 3.2.: Schematic view of the ATLAS tracking system, taken from [36]

which are arranged parallel to the beam axis in the barrel region and axially in the endcaps. The outermost component of the inner detector system, the transition radiation tracker (TRT) - is comprised of straw tubes filled with a Xenon based gas mixture. The TRT provides continous tracking information and allows to identify charged particles by means of their transition radiation emitted when crossing the tubes [37].

3.2.2. The ATLAS calorimeters

A schematic view of the ATLAS calorimeter system is shown in Figure 3.3, including the electromagnetic and hadronic barrel and endcap calorimeters and the forward calorimeter. All ATLAS calorimeters use a sampling technique which separates energy absorption and measurement.

The electromagnetic calorimeter

The ATLAS electromagnetic calorimeter uses liquid argon (LAr) as active material and accordeon shaped lead absorbers, providing complete ϕ symmetry without azimuthal cracks. The lead absorbers are interleaved with copper electrodes which, in the presence of an electric field, collect the charges produced via ionization of the liquid argon by electromagnetic interacting particles.

The electromagnetic barrel calorimeter consists of two wheels which cover the region of $|\eta| < 1.475$ while the electromagnetic endcap calorimeter extends the coverage from
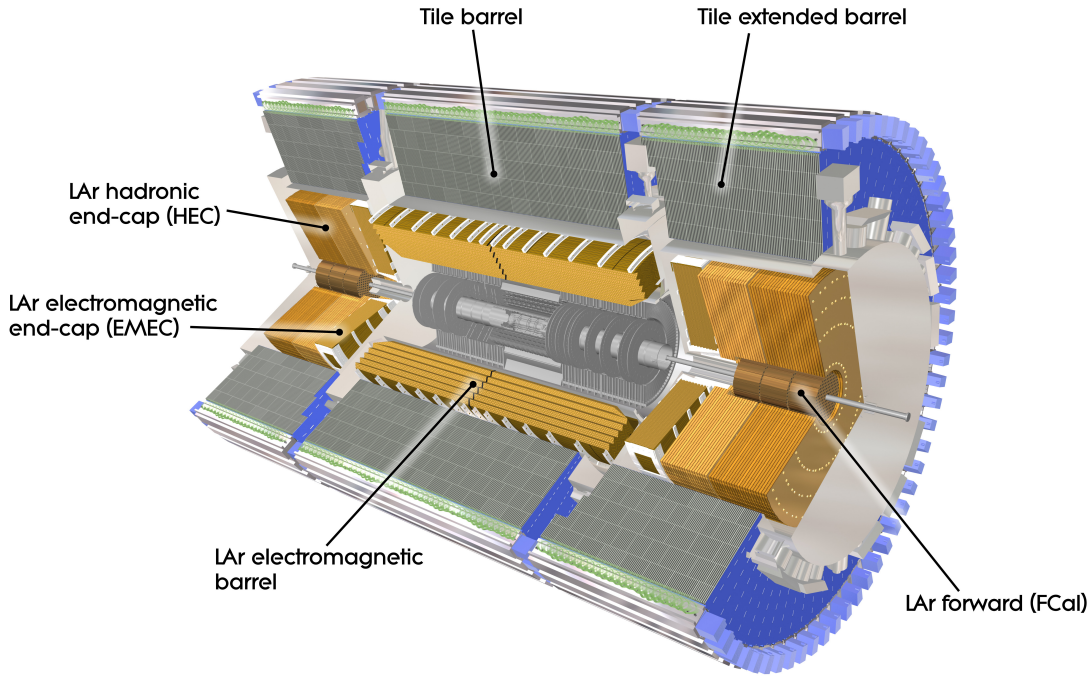
Figure 3.3.: Schematic view of the ATLAS calorimeter system, taken from [36]

$1.375 < |\eta| < 3.2$ and is formed by two concentric wheels in each of the endcaps, respectively. For $|\eta| < 1.8$ a presampler consisting of an active LAr layer is installed directly in front of the EM calorimeters, which provides a measurement of the energy lost upstream. All LAr calorimeters are housed in cryostats ensuring temperature uniformity as fluctuations in the LAr temperature directly impact the energy measurement.

Figure 3.4 illustrates the structure of the LAr barrel calorimeter which is divided into three layers, with granularities of $\Delta\eta \times \Delta\phi = 0.0031 \times 0.098$, $\Delta\eta \times \Delta\phi = 0.0245 \times 0.098$ and $\Delta\eta \times \Delta\phi = 0.05 \times 0.025$, respectively. The innermost layer provides information on the particle identification and, together with the information from the second layer, allows to reconstruct the position of electromagnetic showers. In addition, due to its radiation length of $\approx 16\ X_0$, most of the energy of the electromagnetic shower is collected in the second layer. The design resolution of the electromagnetic calorimeter is $\frac{\Delta E}{E} = 10\%/\sqrt{E\,[GeV]} \oplus 0.7\% \oplus 170\ MeV/E$ [38–40].

Hadronic Calorimeter

The hadronic barrel and extended barrel calorimeters (tile calorimeter), covering a region of $0 < |\eta| < 0.8$ and $0.8 < |\eta| < 1.7$ respectively, use plastic scintillator tiles as active material and steel as absorber. Hadrons interacting with the scintillators produce light, with the light output being approximately proportional to the deposited energy. The light
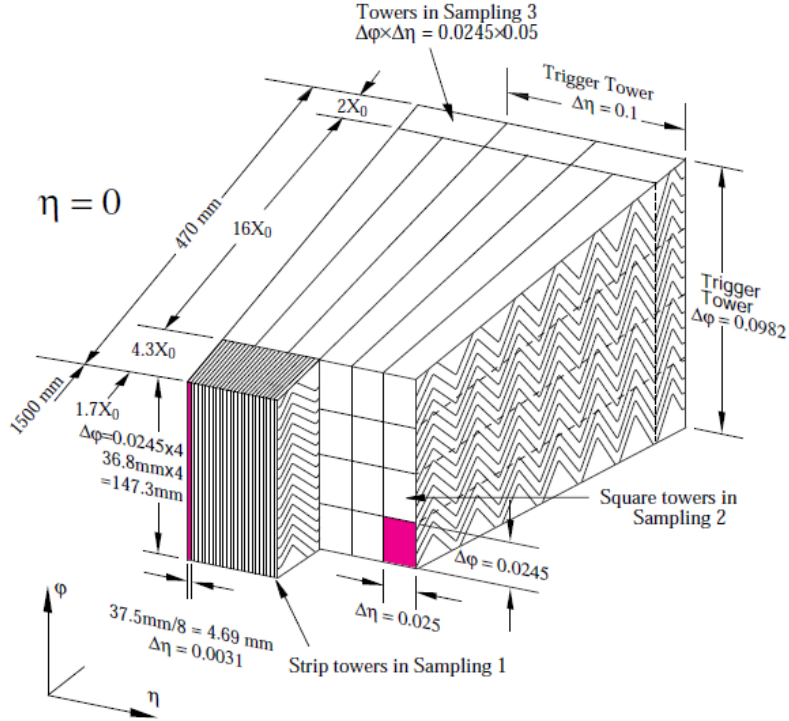
Figure 3.4.: Structure of the LAr calorimeter barrel [34]

is collected and transported to photomultipliers via wavelength shifting fibres which are coupled to either end of the tiles.

The barrel and extended barrel calorimeters are segmented into wedges in ϕ – illustrated in Figure 3.5, corresponding to a granularity of $\Delta\phi = 0.1$. Each of these modules is further segmented into three radial layers, with a granularity of $\Delta\eta = 0.1$ in the first two layers and $\Delta\eta = 0.2$ in the third layer. The design resolution of the tile calorimeter is $\frac{\Delta E}{E} = 50\%/\sqrt{E[GeV]} \oplus 3\%$.

In the endcap cryostats the hadronic LAr endcap calorimeter (HEC) is located, covering the region $1.5 < |\eta| < 3.2$. By contrast to the electromagnetic LAr calorimeter copper is used as absorber. Also integrated in the endcap cryostats is the copper/tungsten LAr forward calorimeter (FCal), covering the region $3.1 < |\eta| < 4.9$. Both electromagnetic and hadronic showers a measured in the FCal [41, 42].

3.2.3. The ATLAS muon spectrometer

The ATLAS muon spectrometer and its subcomponents are illustrated in Figure 3.6. A detailed description can be found elsewhere [43, 44]. A concise summary is given below, closely following [44].
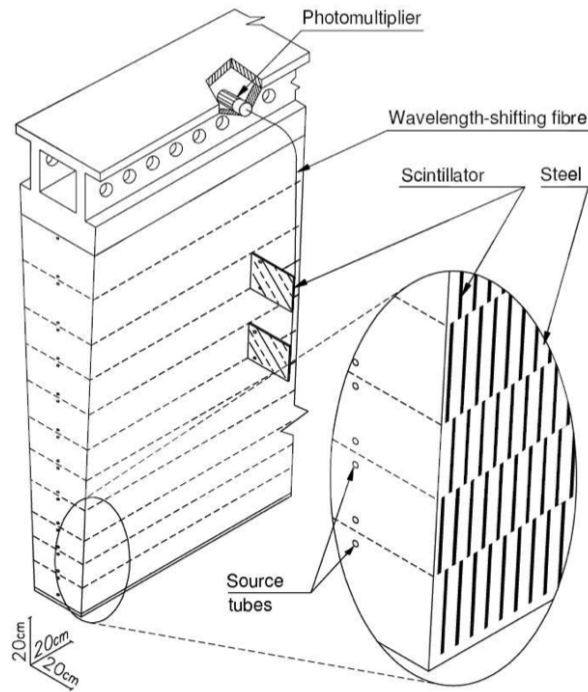
Figure 3.5.: Structure of a tile calorimeter module [41]

Muons, which are the only charged particles escaping the calorimeter, are deflected in the magnetic field provided by three large superconducting air-core toroids located outside the calorimeter system: one in the barrel ($|\eta| < 1.1$) and one for each end-cap ($1.1 < |\eta| < 2.7$). The muon momentum is determined via the track curvature, measured by means of three precision chamber stations allowing for accurate momentum resolution. For most of the acceptance Monitored Drift Tube (MDT) chambers are deployed. In the end-cap inner region ($|\eta| < 2.0$) Cathode Strip Chambers (CSC) are used because of their capability to cope with higher background rates.

The trigger system of the muon spectrometer uses two different chamber technologies with fast response: Resistive Plate Chambers (RPC) located in the barrel region while Thin Gap Chambers (TGC) are used in the higher background environment of the end-cap regions.

3.2.4. The ATLAS trigger system

Due to the high interaction rate at the LHC – which is ≈ 1 GHz at design conditions – the incoming data rate needs to be reduced to an amount which can be sustained by the data acquisition system with minimum dead time. Also, the resulting size of the output data arising from these conditions needs to be reduced to be compatible with the available storage space. A three level trigger system is applied in ATLAS (see Figure 3.7) which
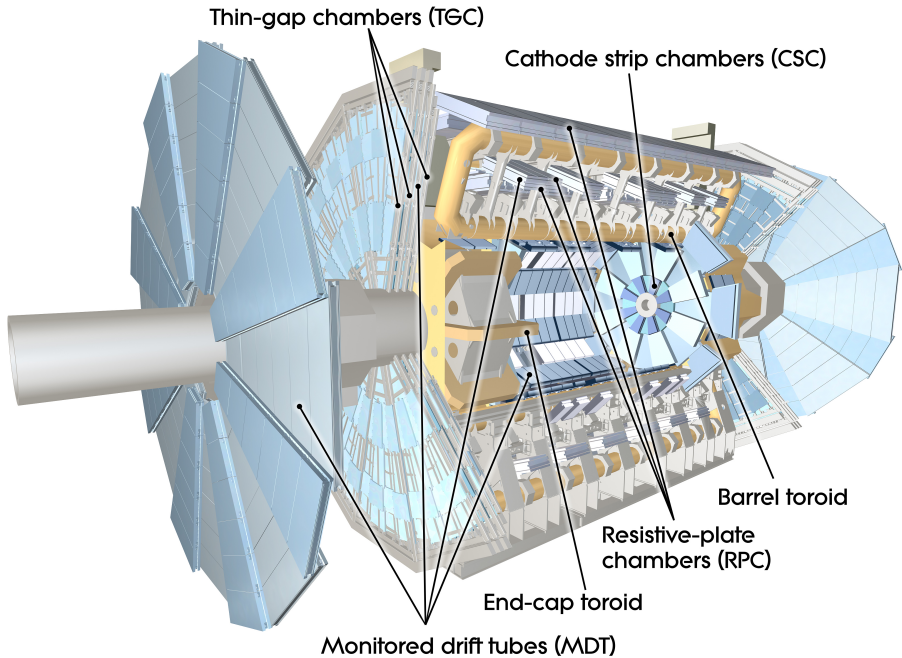
Figure 3.6.: The ATLAS muon spectrometer and its subcomponents [36]

allows to identify interesting physics signatures at high efficiency while rejecting the background of soft interactions.

The first level of the trigger system – the so-called L1 trigger - is purely hardware based. It uses coarse-granularity information provided by the electromagnetic and hadronic calorimeters as well as the muon spectrometer. Based on this information a decision is made in $\approx 2.5 \, \mu s$ whether the event is passed to the so-called high level trigger (HLT).

The HLT comprises the level 2 (L2) trigger system as well as the event filter (EF) which are both software based. The L2 trigger system uses the full granularity information in so-called regions of interest (RoI) defined by the L1 trigger based on the presence of electromagnetic, tau, jet or muon candidates. The event rate is reduced to ≈ 2.5 kHz by the L2 trigger subsystem. By contrast to the L2 trigger the full event information is available to the EF which is run after the so-called event builder. The EF uses the regular ATLAS offline reconstruction software to perform a thorough event selection to finally reduce the data rate to ≈ 400 Hz. Only events passing the EF decision are written to mass storage [45, 46],

3.2.5. Data from the ATLAS experiment

The data used in the measurement presented in this thesis were recorded with the ATLAS detector from proton-proton collision at a centre-of-mass energy of $\sqrt{s} = 7$ TeV in 2011. The dataset fulfilling all data quality criteria (see Section 4.4.1) corresponds to an
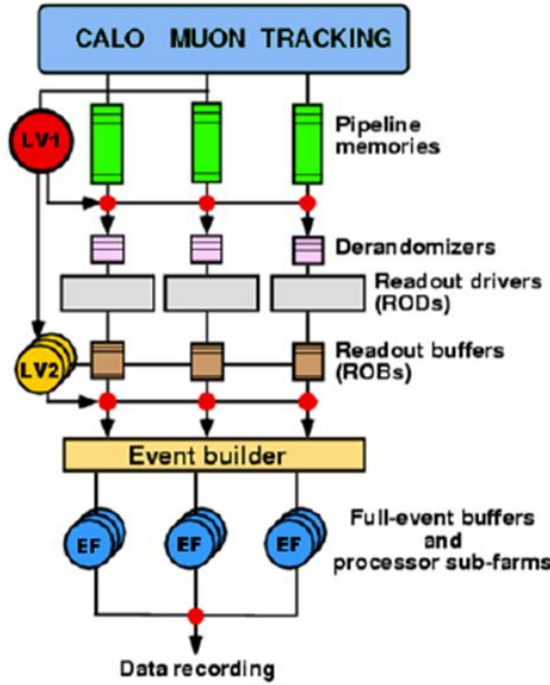
Figure 3.7.: Schematic view of the three-level ATLAS trigger system [45]

integrated luminosity of about 4.7 fb^{-1} [47].

Due to the increase in luminosity with respect to the 2010 runs the contribution of extra proton-proton interactions, other than the primary hard scattering, increased. These extra interactions, denoted as pile-up, are usually specified in the following manner:

- **in-time pile-up**: caused by additional interactions in the same bunch crossing, typically quantified by the number of reconstructed primary vertices per event

- **out-of-time pile-up**: caused by additional interactions from preceding and subsequent bunch crossings, typically quantified by the average number of interactions per bunch crossing ($\langle\mu\rangle$)

4. Reconstruction and selection of physics objects and events

To identify fully hadronic $t\bar{t}$ events in data 'physics objects' need to be defined. These are reconstructed using information from all detector subsystems such as energy deposits in the calorimeters and tracks reconstructed in the muon spectrometer and inner detector. Once a physics object candidate is identified it is required to pass further selection criteria which, for example, include constraints on the transverse momentum, pseudorapidity or isolation. In the first part of the chapter an overview over the various physics objects and their definition used in the analysis is given. These comprise objects being part of the signal signature itself (jets) but also objects which can typically be found in background events (leptons and missing transverse energy $\not{E}_T$) and are hence used to reject background events. After all physics objects are reconstructed event level selection criteria are applied which require, for instance, the presence or absence of certain physics objects. In addition, criteria on the data quality need to be fulfilled by events to be considered in the analysis. The selection critera applied on event level basis are outlined in the second part of this chapter. All selection criteria - apart from those specific to the fully hadronic $t\bar{t}$ signature - follow closely the prescriptions provided by the ATLAS top working group [48].

4.1. Leptons

Electrons are reconstructed from energy deposits in the electromagnetic calorimeter which are matched to tracks from charged particles in the inner detector [49]. Several selection cuts are applied to calorimeter, tracking and combined variables of the reconstructed electron which are implemented in the *tight* set of quality criteria as outlined in [49]. Electrons are required to have transverse energy $E_T > 25$ GeV. Furthermore, the cluster in the electromagnetic calorimeter associated with the electron is required to be within the detector acceptance of $|\eta_{cluster}| < 2.47$, where electrons falling within the transition region between the barrel and end-cap calorimeter $1.37 < |\eta_{cluster}| < 1.52$ are excluded.

Muon candidates are reconstructed from track segments in the different layers of the muon spectrometer and are matched to tracks from the inner detector [50, 51], where the combined muon track is required to have a minimal number of hits in each subdetector [52]. The transverse momentum of the muon is required to have $p_T > 20$ GeV where only muons within the detector acceptance of $|\eta| < 2.5$ are considered.

To reject backgrounds from heavy flavour decays inside jets electron and muon candidates are required to satisfy additional isolation criteria [53]. These criteria include requirements on the maximum energy and transverse momentum of tracks contained in a cone of given size around the lepton candidate. In addition each muon found within a cone of size $\Delta R = \sqrt{\Delta\phi^2 + \Delta\eta^2} = 0.4$ around a jet[1] is removed.

4.2. Missing transverse energy

The calculation of the missing transverse energy $\not{E}_T$ is based upon the momentum balance in the transverse plane. It is evaluated considering energy deposits in all calorimeter cells which are calibrated according to the analysis object with which they are associated. In addition, muons reconstructed in the muon spectrometer are included [54].

The fully hadronic final state does not contain neutrinos giving rise to $\not{E}_T$. However, the missing transverse energy can be used to reject, for instance, lepton+jets $t\bar{t}$ events with two additional gluon jets and a lepton not passing the selection criteria which results in a signature similar to the fully hadronic one. In the analysis a cut on the so-called $\not{E}_T$ significance is applied, defined as the ratio of the missing transverse energy and the scalar transverse momentum sum H_T of all jets passing the object selection criteria.

4.3. Jets

4.3.1. Jet reconstruction

Jets are reconstructed with the anti-k_T algorithm [55] where topological calorimeter clusters [56, 57] are used as input to the jet reconstruction algorithm. Topological clusters are groups of calorimeter cells which are built starting from a seed cell with a signal-to-noise ratio above threshold. Neighbouring cells with energy deposits are then added to the seed cell in an iterative procedure.

Based on an iterative p_T-weighted distance measurement the topological clusters are combined to jets by means of the anti-k_T algorithm. For each pair of calorimeter objects the distances

$$d_{ij} = min(p_{T,i}^{-2}, p_{T,j}^{-2})\frac{\Delta_{ij}^2}{R^2} \tag{4.1}$$

are calculated, where $\Delta_{ij}^2 = (y_i - y_j)^2 + (\phi_i - \phi_j)^2$ and $p_{T,i}$, y_i and ϕ_i are the transverse momentum, the rapidity and the azimuth angle of object i. R denotes the distance parameter of the jet algorithm, where $R = 0.4$ is used for jets in the analysis presented in this thesis. In addition, the distance between object i and the beam is evaluated as

$$d_{i,B} = p_{T,i}^{-2} \tag{4.2}$$

---

[1]For the muon isolation cut only jets with $p_T > 25$ GeV and jet vertex fraction > 0.75 (see Section 4.3.3) are considered.
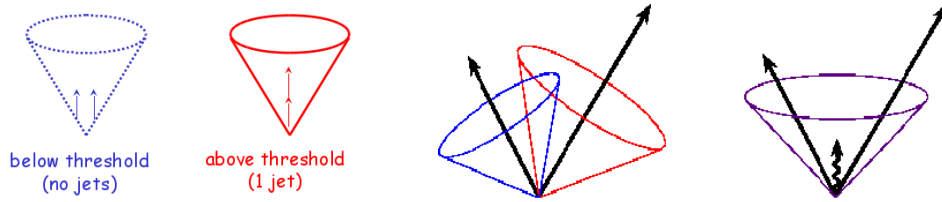
Figure 4.1.: Collinear (left) and infrared safetey (right): The number of reconstructed jets should not be sensitive to collinear parton splitting (left) nor to soft gluon radiation from the primary partons (right), taken from [59].

Two objects are merged if $d_{ij} = min(d_{ij}, d_{i,B})$, otherwise object i is considered a jet and not taken into account in the following iteration steps. The distances are then recalculated and the procedure is repeatead until all objects are merged into jets. The final four-momentum of a jet is given by the sum of the four-momenta of its constituents, usually referred to as four-vector recombination scheme.

Unlike cone algorithms[2] the anti-k_T algorithm is both infrared and collinear safe, i.e. the number of reconstructed jets is neither sensitive to soft gluon radiation from a parton nor to collinear parton splitting, see Figure 4.1.

4.3.2. Jet energy calibration

Jets used in this analysis are built from topological calorimeter clusters at the so-called electromagnetic (EM) scale, which correctly accounts for energy deposits of particles produced in electromagnetic showers [60, 61]. These EM scale jets then undergo the following calibration procedure [61]:

- **Pile-up offset correction**: Correction factors are applied to account for the energy offset caused by in-time and out-of-time pile-up. The correction factors have been studied in simulated events as a function of the number of reconstructed primary vertices - N_{PV} - and the average number of interactions - μ - and are provided in different bins of jet p_T and η.

- **Origin correction**: The direction of the jet is corrected making the jet point back to the primary event vertex instead of the origin of the ATLAS coordinate system.

- **Energy and η calibration**: Monte-Carlo based correction factors are applied correcting the reconstructed jet energies back to particle jet level, where particle jets are built from stable[3] particles in simulated events. The correction factors are derived for an inclusive sample of isolated jets - with pile-up interactions included in the simulated events - in bins of jet p_T and η.

---

[2]Cone algorithms are based on clustering objects within a cone of fixed size R around a seed to build protojets. In an iterative procedure the jet direction is recalculated based on the four-vector sum of the protojet constituents and the cone around the corrected jet direction is redefined accordingly [58].

[3]These include all stable particles with lifetime > 10 ps except for muons and neutrinos.

- **Residual in-situ calibration**: A residual JES correction is applyied to jets reconstructed in data accounting for residual differences in data and Monte-Carlo after the energy and η calibration has been applied. The correction factors are studied using the full 2011 dataset and the inclusive Pythia dijets Monte-Carlo sample based on in-situ techniques making use of the p_T balance between a jet and a reference object. Such reference objects are, for instance, Z bosons or photons in Z+jet [62] and γ-jet [63] events.

4.3.3. Jet selection criteria

Jets are required to have a minimum of 25 GeV of transverse momentum and to lie within $|\eta| < 2.5$.

To identify jets generated from multiple proton-proton interactions, jets are required to have a sufficiently large jet vertex fraction (JVF) [53]. This variable exploits the scalar transverse momentum sum of tracks associated with a specific jet. The contribution of tracks stemming from the primary interaction vertex to the overall sum p_T allows to provide a likelihood for each jet of originating in that vertex. Jets with a jet vertex fraction smaller than 75% are considered to be generated by multiple proton-proton interactions and are thus rejected in the analysis. Scale factors are applied to account for different hard scatter jet selection and pile-up jet rejection (in)efficienies in data and Monte-Carlo simulation.

As electrons deposit energy in the calorimeter they are usually additionally reconstructed as jets. To reject such electron-jet duplicates the closest jet to an electron passing all selection criteria is rejected if the distance between both objects in the η-ϕ plane is smaller than 0.2.

Quality criteria following the loose selection detailed in [64] are applied to jets. These are designed to identify *'bad'* jets reconstructed from energy deposits in the calorimeters originating from non-collision events. Events are rejected if at least one jet with $p_T > 20$ GeV fails the quality criteria.

4.3.4. b-jet identification

To discriminate the fully hadronic $t\bar{t}$ signal from background events b-jet identification is an important tool, as the dominant fraction of background multijet events comprises light quark and gluon jets. Several b-tagging algorithms are available which exploit the unique properties of b-jets [34, 65] allowing for a good discriminating power against light quark jets.

Due to their relatively long lifetime b-hadrons travel a significant distance from the primary vertex before decaying, resulting in a displaced secondary vertex for b-jets.

In addition, the b-hadron decay in the secondary gives rise to displaced tracks with measurable transverse and longitudinal impact parameters. The transverse impact parameter d_0 is defined as the distance of closest approach of an extrapolated track to the primary vertex in the R-ϕ projection, see Figure 4.2. The z coordinate of the track at this point z_0 is referred to as longitudinal impact parameter. Vertices and impact parameters measured in the inner detector serve as input to b-tagging algorithms which provide a likelihood on whether a jet can be classified as b-jet[4].

The b-jet identification algorithm used in the analysis is the so-called MV1 tagger [65]. This algorithm is based on a neural network using the output weights of three tagging algorithms - JetFitterCombNN, IP3D and SV1 - as input. The SV1 algorithm exploits the reconstruction of the secondary vertex in b-jets, the IP3D algorithm is based on the measurement of impact parameters and JetFitter exploits the topology of weak b and c-hadron decays inside b-jets. The MV1 tagger is used at its 70% working point, where the efficincy has been evaluated in simulated $t\bar{t}$ events. The corresponding light jet rejection factor yields approximately 130. To account for differences in the b-tagging efficiency and mistag rate[5] in data and Monte Carlo simulation b-tagging correction factors are derived per jet [66–69] and are applied to the Monte Carlo events as a function of the jet p_T and η.

4.4. Event selection

4.4.1. Data quality and non-collision background rejection

As outlined in Section 4.3.3 events with at least one 'bad' jet with transverse momentum above 20 GeV are discarded. In addition, events affected by noise bursts in the LAr calorimeter are not considered in the analysis. To exclude non-collision events like cosmic muons and beam background [71] from the analysis the primary vertex per event is required to be formed by at least 5 tracks. From all interaction vertices reconstructed in the inner detector the primary vertex is defined as the one with the highest p_T sum of associated tracks.

Data events are required to fulfill additional data quality (DQ) criteria ensuring that all detector sub-systems relevant for the analysis performed with no major problems during the data taking process [72]. The DQ information is available via lists of runs and luminosity blocks fulfilling all DQ requirements. Only events belonging to runs and luminosity blocks listed in these 'good runs lists' are considered in the analysis.

---

[4]Further tagging algorithms are available which make use of the presence of soft muons or electrons stemming from the b-hadron decay inside b-jets, see for example [34].

[5]i.e. the rate of light quark and c-jets being tagged as b-jets
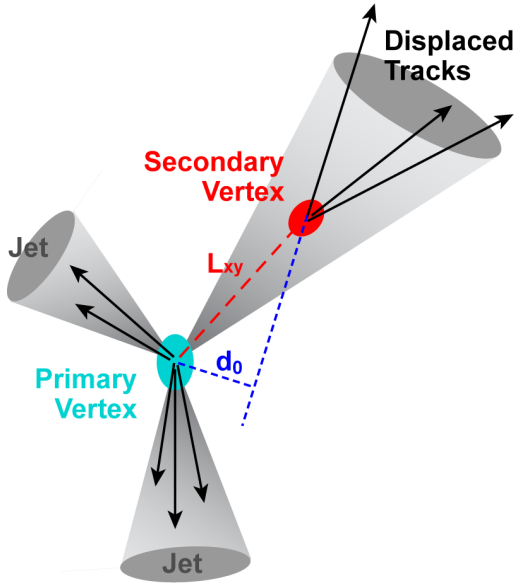
Figure 4.2.: Due to their relatively long lifetime *b*-hadrons travel a significant distance from the primary vertex before decaying, resulting in a displaced secondary vertex with a measurable flight length L_{xy}. In addition, the *b*-hadron decay in the secondary vertex gives rise to displaced tracks with measurable transverse d_0 and longitudinal z_0 (not shown in the picture) impact parameters. Based on the measurement of these variables in the inner detector a likelihood can be provided of a jet being a *b*-jet. Picture taken from [70].

4.4.2. Trigger

Events are required to pass the `EF_5j30_a4tc_EFFS` trigger [73, 74] which uses the so-called `L1_5J10` trigger at L1 level (see Section 3.2.4). The L1 calorimeter trigger searches for jet signatures by means of a sliding-window algorithm [57, 74, 75] which uses a 8 × 8 trigger-tower grid in η and ϕ as input. The trigger towers are located in the electromagnetic and hadronic calorimeters and have a η-ϕ granularity of 0.2 × 0.2 for $|\eta| < 3.2$ and 0.4 × 0.4 for $|\eta| > 3.2$. If 5 jet candidates with transverse energy $E_T > 10$ GeV are identified at level 1 the information is passed to the L2 trigger. At level 2 a three-iteration cone R=0.4 algorithm is run seeded by the L1 region of interests (RoIs, see Section 3.2.4) to identify 5 jets with $E_T > 25$ GeV (`L2_5j25`). At event filter (EF) level a full scan (`EFFS`) of the RoIs is performed [74]. Topological clusters (`tc`) of calorimeter cells calibrated at the electromagneticectromagnetic scale are used as input to the anti-k_T algorithm with distance parameter R = 0.4 (`a4`). The full trigger chain is passed by an event if 5 jets with $E_T > 30$ GeV are identified by the EF trigger subsystem. The acronym `EF_5j30_a4tc_EFFS` summarises their event trigger definition.

To make sure the trigger is fully efficient in data and Monte Carlo simulation, only events are kept where all jets with calibrated $p_T > 20$ GeV are separated by $\Delta R > 0.6$

as outlined in [76]. According to studies presented in [77] the offline p_T threshold of the five leading jets is set to 55 GeV. This value is motivated by the dependence of the `EF_5j30_a4tc_EFFS` trigger on the 5th leading jet p_T where a 90% efficiency is reached for $p_T^{5th} > 55$ GeV.

4.4.3. Analysis specific event selection criteria

Besides the data quality and trigger requirements a further set of event selection criteria is applied which is specific to the fully hadronic $t\bar{t}$ analysis as it aims to select signal events out of the data sample while keeping the amount of selected background events low. Those cuts are therefore closely related to the decay toplogy of the fully hadronic $t\bar{t}$ channel and to the kinematic properties of the $t\bar{t}$ final state jets. The various event level selection criteria are summarised below - for completeness the list also includes the data quality and trigger requirements:

- Events are required to pass all data quality and non-collision background rejection cuts listed in Section 4.4.1.

- Events are required to pass the `EF_5j30_a4tc_EFFS` trigger. All jets with transverse momentum above 20 GeV are required to be isolated as outlined in Section 4.4.2.

- The $\not{E}_T$ significance (see Section 4.2) is required to be smaller than 3 to reject backgrounds with neutrino signature, such as lepton+jets $t\bar{t}$ events or W+jets events where the W boson decays leptonically.

- Events with one or more identified leptons (electrons, muons) are rejected.

- The event needs to contain at least 6 reconstructed jets. To ensure 90% efficiency of the multijet trigger the five leading jets are required to have transverse momentum larger than 55 GeV. The sixth leading jet is required to have $p_T^{6th} > 30$ GeV. Additional jets with $p_T > 25$ GeV are conisdered in the analysis, i.e. these are included in all control plots and are input to the kinemtatic likelihood fit used for the reconstruction of the $t\bar{t}$ decay topology. All jets are required to have $|\eta| < 2.5$.

- Events are required to have exactly two b-tagged jets, where the MV1 tagging algorithm at its 70% working point is used, see Section 4.3.4.

After applying the above selection criteria the expected multijet background contribution is $\approx 88\%$ (see Section 5.2.3). Thus, for the validation of the background modelling – detailed in Chapter 5 – only the above set of cuts was used. For the analysis presented in this thesis additional selection criteria were applied:

- The centrality – defined as the scalar sum of the transverse energy of all jets j passing the event selection criteria divided by the invariant mass of these jets

$$centrality = \frac{\sum_j^{jets} E_{T,j}}{\sum_j^{jets} m_j} \qquad (4.3)$$

– is required to be larger than 0.6. This cut is used to further suppress the contribution from background events whose jets on average are less central compared to jets in signal events.

- The likelihood output of the kinematic likelihood fit applied to reconstruct the fully hadronic $t\bar{t}$ decay is required to be larger than -44 to further reduce the background contribution.

- Given the relatively large CPU consumption of the kinematic likelihood fit, only events with a maximum of eight jets with transverse momentum above 25 GeV are considered.

Control plots illustrating the data to Monte-Carlo simulation and background agreement after the final set of event selection criteria are shown in Chapter 6.

5. Modelling of signal and background processes

5.1. Modelling of signal processes

Fully hadronic $t\bar{t}$ final states are modelled using simulated data. To simulate pp interactions Monte-Carlo generators make use of the factorisation theorem, see Section 2.2.1, allowing to separate hard short distance processes from soft non-perturbative processes. For the nominal signal sample the hard parton-parton scatter interaction is described by the next-to-leading order matrix element provided by PowHeg [78], which is used together with the NLO parton distribution function set CT10 [79].

For the simulation of parton shower and hadronisation processes Powheg needs to be interfaced to a full event simulation generator, such as Pythia [80] or Herwig [81]. Pythia makes use of the so-called Lund string model [82] where the colour field between two distant partons is described as string whereas Herwig is based on the cluster fragmentation model. The nominal Monte-Carlo signal samples are simulated using Pythia as parton shower Monte-Carlo, while a reference sample is simulated using Herwig to study systematic uncertainties related to the fragmentation modelling.

Besides the hard parton-parton scatter, pp interactions also include a soft component. The so called **underlying event** originates from **beam-remnants**, i.e. partons which do not directly take part in the hard interaction but are colour connected to the hard scatter partons. Furthermore, **multiple parton interactions** between the remaining partons from the pp pair can give rise to additional semi-hard processes accompanying the hard scatter. Due to their non-perturbative nature underlying event processes require phenomenological models that need to be tuned to data. To build underlying event **tunes**, distributions sensitive to soft activity - such as charged particle distributions - are studied in the region perpendicular to the axis defined by the hard scatter. This so-called transverse region is defined via the azimuthal angular difference $60° < |\Delta\phi| < 120°$ relative to the direction of the hard scatter products approximated by the leading p_T object. A summary on soft QCD measurements performed in ATLAS is given in [83]. The simulation of underlying event activity is already included in Pythia, while Herwig makes use of the Jimmy package [84]. The nominal signal Monte-Carlo simulation uses Pythia together with the Perugia 2011C tune [85] to model underlying event processes, while Jimmy together with the ATLAS AUET2 [86] is used for the PowHeg+Herwig reference sample.

To simulate the interaction of the generated particles with the detector material, the event information is passed to the GEANT4 [87] framework. Energy deposits in the active detector material are converted into detector signals, which are provided as input to the same trigger and object reconstruction software used for the data. **Full simulation** of the detector geometry and material distribution is used for one signal sample generated with the world average top quark mass $m_{top}^{in,MC} = 172.5$ GeV. The remaining samples, including all 7 mass point samples ($m_{top}^{in,MC} = 165, 167.5, 170, 172.5, 175, 177.5$ and 180 GeV) as well as samples to study systematic uncertainties, use **fast simulation** allowing to generate larger samples of Monte-Carlo events.

The Monte-Carlo samples are normalised to the predicted top-antitop cross-section at $\sqrt{s} = 7$ TeV, which for $m_{top} = 172.5$ GeV yields $166.8^{+16.5}_{-17.8}$ pb [88]. This value has been calculated at approximate NNLO in QCD with the Hathor 1.2 package [89] using the MSTW2008 90% NNLO PDF sets [90] incorporating PDF + α_S uncertainties, according to the MSTW prescription [91], added in quadrature to the scale uncertainty. This value was verified using the NLO+NNLL calculation [92] as implemented in Top++ 1.0 [93].

5.2. Data-driven background modelling

In the fully hadronic $t\bar{t}$ decay channel the dominant background contribution comes from multijet events with at least 6 reconstructed jets. As the matrix elements have only been calculated for interactions involving up to 6 partons, high jet multiplicity final states cannot be simulated accurately. A data driven technique, called ABCD method, is therefore applied to model kinematic distributions of multijet events passing the analysis selection criteria.

5.2.1. The ABCD method

Figure 5.1 illustrates the basic idea of the ABCD method. Two observables are chosen to divide the data sample - typically after applying a certain set of preselection cuts - into four regions. Region D (signal region) includes all events passing the whole chain of analysis selection cuts, the remaining three regions include events which fail the event selection with respect to observable 1 (region C), observable 2 (region B) or observable 1 and observable 2 (region A).

If observable 1 and observable 2 are uncorrelated for background events the fraction of events passing the cut with respect to observable 1 is the same in both the combined A+B and C+D regions, hence:

$$\frac{n_D^{background}}{n_C^{background}} = \frac{n_B^{background}}{n_A^{background}} \tag{5.1}$$

where $n_i^{background}$ is the number of background events in region i. To extract the background distribution of a third observable x (m_{jjj}, m_{jj}, p_t^{1st},...) formula 5.1 can be rewritten in its
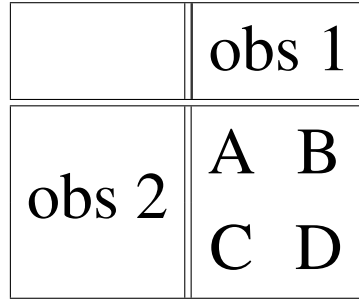
Figure 5.1.: Basic idea of the ABCD method: the data sample is divided into 4 regions by means of 2 variables obs1 and obs2.

differential form:

$$\frac{dn_D^{background}}{dx} = \frac{n_C^{backgrpund}}{n_A^{background}} \frac{dn_B^{background}}{dx} \tag{5.2}$$

the underlying assumption being, again, that x is correlated with neither of the two observables. The shape of x is thus taken from region B (i.e. the number of events per dn/dx bin in region B), whereas the region yields in A and C are used for the overall normalisation of the background distributions. The background yields - both the differential ones per dx bin as well as the overall yields per region (integrated over the full dx range in the region of interest) - typically rely on the signal MC via $n_i^{background} = n_i^{data} - n_i^{signal\ MC}$. It is hence crucial to keep the signal contamination in regions A,B,C small avoiding that uncertainties connected to the signal MC modelling propagate to large uncertainties on the background shapes and normalisation.

5.2.2. Background modelling for the fully hadronic $t\bar{t}$ event topology - 'extended' ABCD method

Starting from data events passing a specific set of analysis selection criteria but

- ≥ 5 jets with $p_T > 55$ GeV

- 6th jet with $p_T > 30$ GeV

- exactly 2 b-tagged jets

6 regions are defined specified by the transverse momentum of the 6th leading jet as well as the number of b-tagged jets as detailed in table 5.1. To reduce correlations between the b-tag multiplicity and the transverse momentum of the 6th leading jet (see Section 5.2.4) - introduced due to the p_T dependence of the b-tagging algorithm - only the four leading jets are considered to extract the number of b-tagged jets.

The extension of the 4-region ABCD method to the 6-region ABCDEF method provides additional regions for the evaluation of the background shapes and normalisation accord-

	$p_T^{6th\ jet} \leq 30$ GeV	$p_T^{6th\ jet} > 30$ GeV
0 *b*-tagged jets	A	B
1 *b*-tagged jet	C	D
2 *b*-tagged jets	E	F

Table 5.1.: Regions used for the background modelling of the fully hadronic mass analysis.

ing to:

$$\frac{dn_F^{background}}{dx} = \left(\frac{1}{n_A^{background}} \frac{dn_B^{background}}{x} + \frac{1}{n_C^{background}} \frac{dn_D^{background}}{dx} \right) \frac{n_E^{background}}{2} \qquad (5.3)$$

The factor 2 in the denominator of the last term in equation 5.3 arises from the additional region used to extract the background shapes in the ABCDEF method.
The yields per dx bin ('shapes') in regions $i = B, D$ are estimated via

$$\frac{dn_i^{background}}{dx} = \frac{dn_i^{data}}{dx} - \frac{dn_i^{signal(MC)}}{dx}, \qquad (5.4)$$

while the overall yields in regions $i = A, C, E$ are evaluated using

$$n_i^{background} = n_i^{data} - n_i^{signal(MC)}. \qquad (5.5)$$

5.2.3. Expected data and signal yields in the background regions

The data and signal yields per region depend on the set of preselection cuts applied before subdividing the data into the various regions. For the validation of the background modelling only basic selection criteria were applied, as detailed in Section 4.4.3, allowing to investigate the data vs. Monte-Carlo simulation+background agreement in samples highly dominated by background events. The data and signal yields per region after preselection criteria are summarised in Table 5.2. In addition, the corresponding signal fractions per region are given. The second set of selection criteria comprises all cuts applied in the final analysis, including criteria related to the reconstructed $t\bar{t}$ system, e.g. the likelihood output of the kinematic likelihood fit, see Section 7.2. The data and signal yields as well as the signal fractions per region for the final set of analysis selection criteria are given in Table 5.3. In both cases the signal yields have been studied using the nominal PowHeg+Pythia full simulation Monte-Carlo sample, where the number of events passing the various selection criteria has been scaled to the integrated luminosity of 4.7 fb^{-1}.

region	data events	signal events	signal fraction
A: 0 b-tagged jets, $p_T^{6th\ jet} \leq 30$ GeV	99138±315	257.1±5.5	0.259±0.006%
B: 0 b-tagged jets, $p_T^{6th\ jet} > 30$ GeV	433052±658	2750.0±17.9	0.635±0.005%
C: 1 b-tagged jet, $p_T^{6th\ jet} \leq 30$ GeV	23603±154	555.0±7.7	2.35±0.05%
D: 1 b-tagged jet, $p_T^{6th\ jet} > 30$ GeV	108502±329	5186.9±23.7	4.78±0.04%
E: 2 b-tagged jets, $p_T^{6th\ jet} \leq 30$ GeV	4370±90	313.8±7.3	7.2±0.3%
F: 2 b-tagged jets, $p_T^{6th\ jet} > 30$ GeV	20590±194	2532.9±21.1	12.3±0.2%

Table 5.2.: Data and signal (Monte-Carlo simulation) yields as well as the signal fractions per region after applying a reduced set of selection criteria to the data. Also given are the statistical errors.

region	data events	signal events	signal fraction
A: 0 b-tagged jets, $p_t^{6th\ jet} \leq 30$ GeV	52374±229	204.2±4.9	0.39±0.01%
B: 0 b-tagged jets, $p_t^{6th\ jet} > 30$ GeV	216142±465	1829.2±14.6	0.846±0.009%
C: 1 b-tagged jet, $p_t^{6th\ jet} \leq 30$ GeV	13316±115	453.1±7.0	3.40±0.08%
D: 1 b-tagged jet, $p_t^{6th\ jet} > 30$ GeV	58143±241	3679.2±20.0	6.33±0.06%
E: 2 b-tagged jets, $p_t^{6th\ jet} \leq 30$ GeV	2650±70	266.1±6.7	10.0±0.5%
F: 2 b-tagged jets, $p_t^{6th\ jet} > 30$ GeV	12055±149	1918.4±18.4	15.9±0.3%

Table 5.3.: Data and signal (Monte-Carlo simulation) yields as well as the signal fractions per region after applying the final set of selection criteria used for the top quark mass analysis to the data. Also given are the statistical errors.

To reduce the signal fraction as well as to improve the background statistics (signal events subtracted from data) in regions A-D, scenarios have been tested where cuts being part of the final analysis selection but not of the preselection were applied to the 2-tag regions only. However, these have been found to be correlated with most of the variables of interest resulting in different shapes in regions B and D with respect to the signal region F, making it necessary to apply the additonal cuts to the data sample before subdividing events into the regions.

Comparing the signal fractions in the regions used to extract the background shapes, the expected signal contamination rises from $\approx 0.6\%$ to $\approx 0.8\%$ in region B and from $\approx 4.8\%$ to $\approx 6.3\%$ in region D [1] when applying the additional selection cuts, which can still be regarded as reasonably small. After preselection cuts, about ≈ 530000 background events are left in regions B and D which is about 30 times the backround yield expected in the

---

[1]When measuring the top quark mass the fraction of background events is used as a free parameter in the binned likelihood fit. Thus, the background regions by means of which the shapes are extracted play a more important role in this analysis. The overall background normalisation, however, is used to produce data vs. MC+background comparison plots allowing to test the performance of the method.

signal region F (≈ 18000 events). The number of background events in region B and D decreases to ≈ 270000 after applying all analysis cuts, which is, however, still about 27 times larger compared to the number of background events in the signal region (≈ 10000 events).

5.2.4. ABCD method and correlations

Formula 5.3 is only applicable if correlations between

1. the b-tag multiplicity and the 6th leading jet p_T

2. between the distribution of interest (x) and the b-tag multiplicity / the 6th leading jet p_T

are marginal. The following sections discuss the degree of correlation expected for the variables needed for the background modelling as well as the impact of correlations on distributions needed for the top quark mass measurement.

b-tagging efficiency and transverse momentum

To extract the number of b-tagged jets the MV1 tagging algorithm [65] at 70% efficiency is used. As illustrated in Figure 5.2 the actual efficiency of identifying a b-jet by means of the MV1 algorithm increases with the transverse momentum of the jet, introducing a correlation of $\rho = 0.03$ between the b-tagged jet multiplicity and the 6th leading jet p_T, while this correlation is reduced to $\rho = 0.006$ when only considering the four leading jets to evaluate the number of b-tagged jets. The p_T distributions of the 6th leading jet - normalised per b-tag multiplicity bin - are illustrated in Figure 5.3, where the b-tag multiplicty has been evaluated considering only the four leading jets (left) and considering all jets (right). Even though the correlation coefficients are comparatively small in both cases, it should be noticed that these are valid over the whole phase space region under consideration and thus represent an averaged picture. For further clarification the ratios of the p_T distribution in the 2-tag bin with respect to the 0-tag bin and the 2-tag bin with respect to the 1-tag bin are also illustrated in Figure 5.3. When not restricting the b-jet multiplicity to the four leading jets the ratio plots show a raising slope as larger p_T values are favoured in the higher b-tag multiplicity bins. The fraction of background events with $p_T^{6th} > 30\,\text{GeV}$ is hence different for different b-tag multiplicity regions making one of the basic assumptions upon which the ABCD method is built - implemented in equation 5.1 - break down. As a result, the background normalisation predicts a too small number of events when including the 6th leading jet for the evaluation of the b-tag multiplicity. The plots in Figure 5.3 were made applying the reduced set of selection criteria. The corresponding plots for the full chain of analysis cuts are given in Figure B.1, showing a similar trend in the 2-tag to 1-tag and 2-tag to 0-tag ratio plots.

The choice of restricting the number of b-tagged jets to the four leading jets is motivated by means of Figure 5.4 which illustrates the correlations between the p_T of the 6th leading
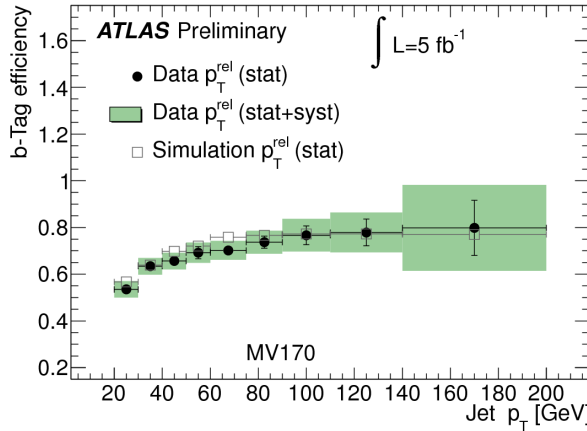
Figure 5.2.: The *b*-tag efficiency in data and simulation for the MV1 tagging algorithm at 70% efficiency obtained with the p_T^{rel} method, taken from [67].

jet with respect to the p_T of the 1st, 2nd, 4th and 5th leading jet [2]. Naturally, the jet transverse momenta are expected to be correlated due to the p_T ordering, i.e. $p_T^{1st} \geq p_T^{2nd} \geq p_T^{3rd} \geq ...$ by definition. Jets lying close together in this ordering scheme are expected to show stronger p_T correlations. While the correlation between the 6th and 5th leading jet momenta yields $\rho = 0.31$ it is already reduced to $\rho = 0.22$ when choosing the 4th leading jet and decreases down to $\approx 11\%$ for the leading jet.

b-tagging efficiency and jet η

In addition to the jet transverse momentum the *b*-tagging efficiency typically depends on the jet η. This dependence gets visible when superimposing the η distributions in data against the Monte-Carlo simulation+background expectation, see Figure 5.5. In the case of the four leading jets, i.e. the jets considered for the *b*-tagging, central jets are more favoured in data compared to the Monte-Carlo simulation+background expectation. This behaviour can be understood as a result of the *b*-tagging efficiency, which is larger for smaller $|\eta|$ values and decreases for forward jets. As the background shapes are taken from the 0 and 1-tag regions while the data distributions are extracted from the signal region, i.e. the 2-tag bin, less central jets are expected to enter the background distributions compared to the data.

For further investigation the normalised η distributions in background events are plotted in Figure 5.6 for the leading p_T jet - separately for regions B (0-tag), D (1-tag) and E (2-tag = signal region). The background shapes are extracted via $n_i^{background} = n_i^{data} -$

---

[2]To guarantee full efficiency of the multijet trigger the transverse momenta of the five leading jets are required to be above 55 GeV. Thus, whenever the transverse momentum of the 6th leading jet exceeds this value, the lower p_T threshold for the leading 1-5 jets is represented by p_T^{6th}, resulting in the not populated triangular region in the plots starting from 55 GeV.
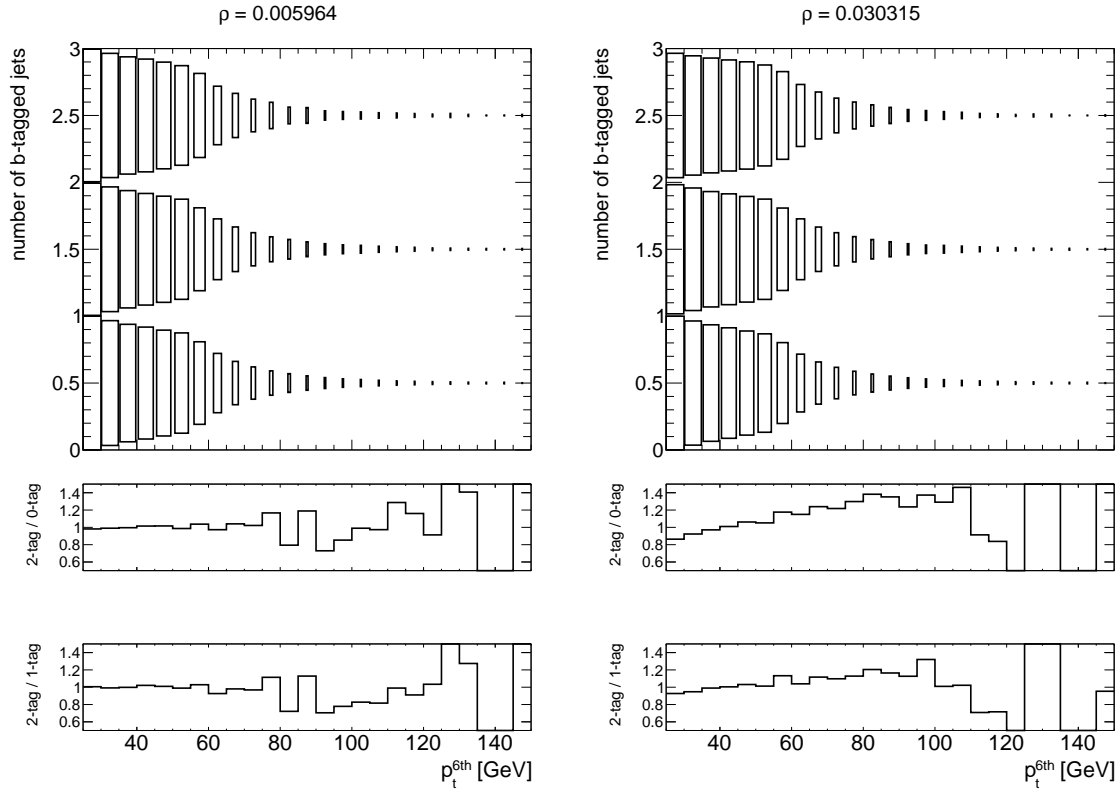
Figure 5.3.: p_T distributions of the 6th leading jet - normalised for each *b*-tag multiplic-
ity bin. The *b*-tag multiplicity has been evaluated considering only the four
leading jets (left) and considering all jets (right). Also shown are the ratios of
the p_T distribution in the 2-tag bin with respect to the 0-tag bin and the 2-tag
bin with respect to the 1-tag bin. Even though the correlation coefficients are
small in both cases, not restricting the *b*-jet multiplicity to the four leading
jets results in a raising slope in the ratio plots as larger p_T values are favoured
in the higher *b*-tag multiplicity bins. Only a reduced set of selection criteria
was applied to the data sample.
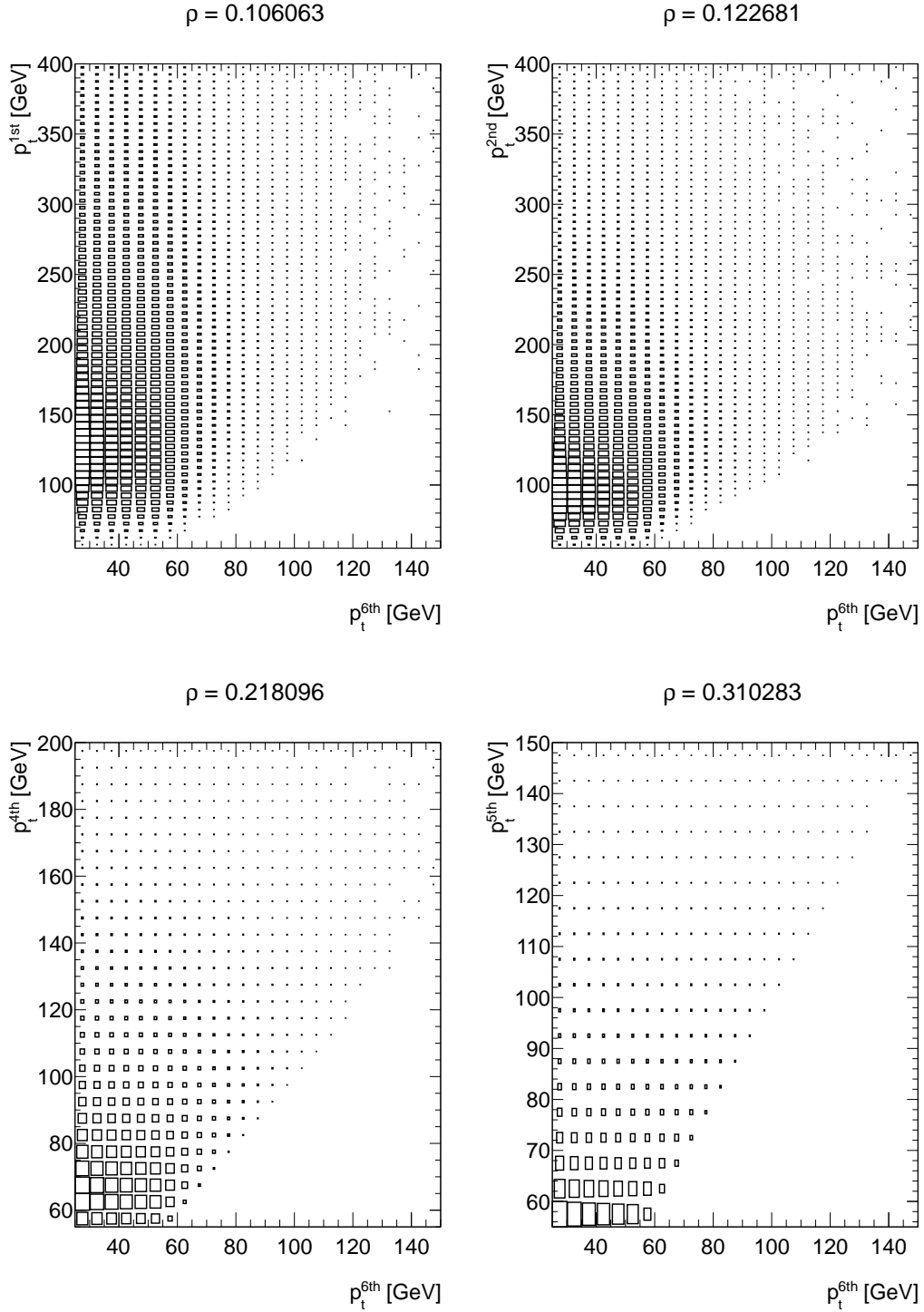
Figure 5.4.: Correlations between the p_T of the 6th leading jet with respect to the p_T of the 1st, 2nd, 4th and 5th leading jet. Jets which are close together in the p_T ordered scheme - $p_T^{1st} \geq p_T^{2nd} \geq p_T^{3rd} \geq$ ... - are observed to show stronger p_T correlations. While the correlation between the 6th and 5th leading jet momenta yields $\rho = 0.31$ it is already reduced to $\rho = 0.22$ when choosing the 4th leading jet and decreases down to ≈ 0.11 for the leading jet.
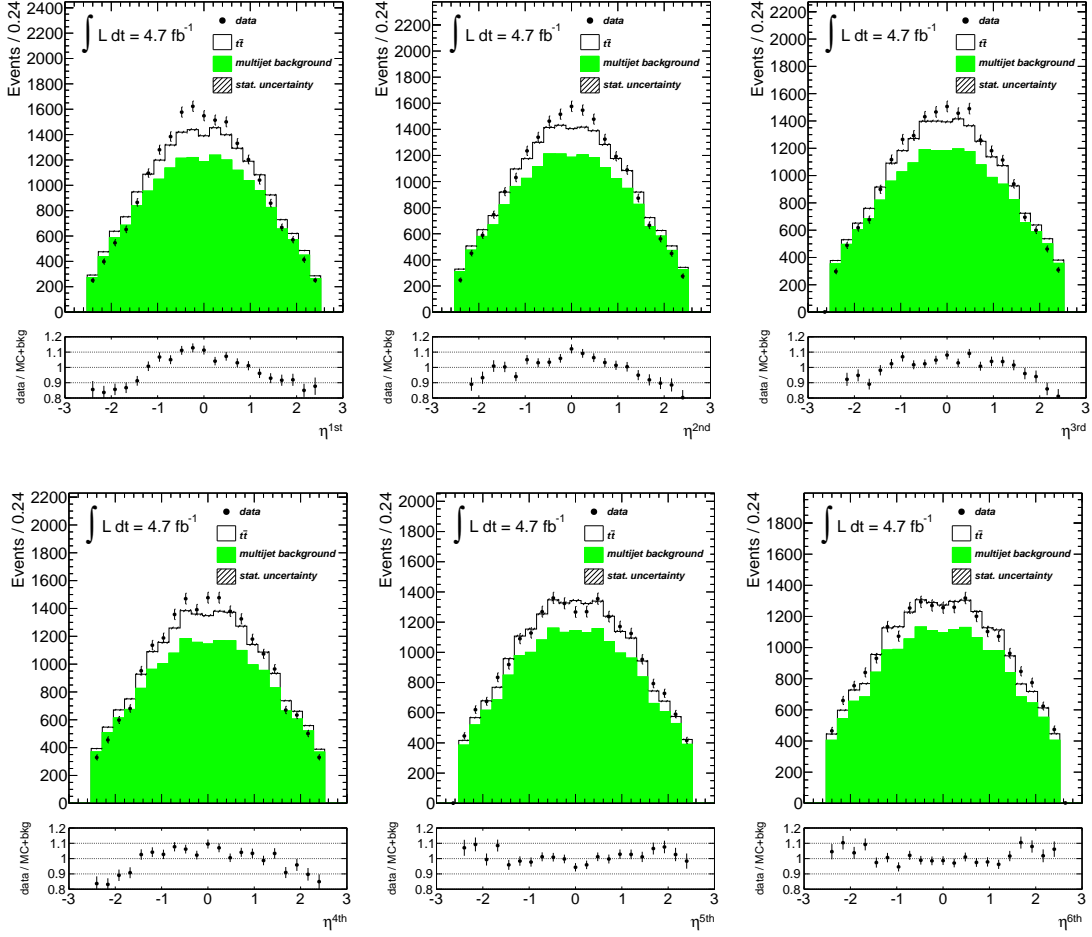
Figure 5.5.: η distributions for the six leading jets. The data distributions are superimposed to the expected signal (Monte-Carlo simulation - white) and background (ABCD method - green) distributions. In the case of the four leading jets the background model predicts too little central jets. This can be understood as a result of the η dependent efficiency of the b-tagging algorithm in combination with extracting the background shapes from different b-tag multiplicity bins.

$n_i^{signal(MC)}$. Compared are the η distributions including all (Figure 5.6 left) and only non-tagged (Figure 5.6 right) jets. While the distributions are in good agreement when not considering any b-tagged jets the differences get visible when including all jets, resulting in a higher contribution of central jets for higher b-tag multiplicity regions. This indicates that the effect observed in the η distributions can indeed be traced back to the performance of the b-tagging algorithm.
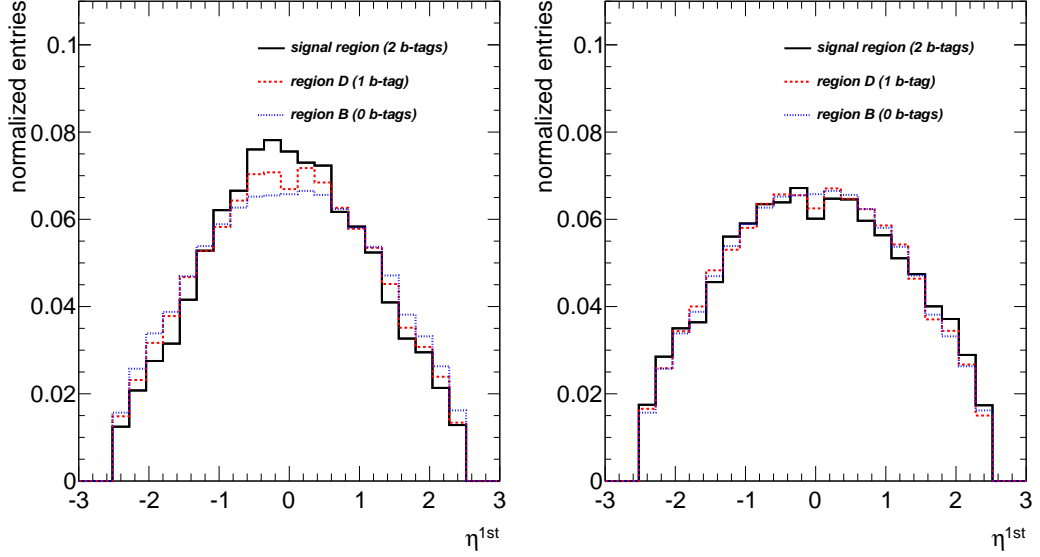
Figure 5.6.: Normalised η distributions in background events of the leading-p_T jet - separately for regions B (0-tag), D (1-tag) and E (2-tag = signal region). The background shapes are extracted via $n_i^{background} = n_i^{data} - n_i^{signal(MC)}$. Compared are the η distributions including all (left) and only non-tagged (right) jets. While the distributions are in good agreement when not considering any b-tagged jets the differences get visible when including all jets, resulting in a higher contribution of central jets for higher b-tag multiplicity regions.

Impact of η-dependent b-tagging efficiency on other variables

The mismatch between data and Monte-Carlo simulation+background model observed in the η distributions is expected to propagate to all η dependent variables. To investigate which distributions are affected and, in particular, whether these include distributions essential for the top quark mass measurement, a simple reweighting procedure is applied:

- The weight factors - to be applied to the background [3] distribution of interest in the 0-tag and 1-tag bin, are evaluated starting from the η distributions in regions A,

---

[3] i.e. $n_i^{background} = n_i^{data} - n_i^{signal(MC)}$

C, E (0, 1 and 2-tag regions with $p_T^{6th} < 30$ GeV [4]. Two sets of weight factors are studied, parameterised as a function of

1. the leading jet $|\eta|$: $w(|\eta^{1st}|)$

2. the leading and subleading jet $|\eta|$: $w(|\eta^{1st}|,|\eta^{2nd}|)$

- For each of the below bins in $|\eta^{1st(2nd)}|$:

    1. $0 \leq |\eta^{1st(2nd)}| < 0.6$

    2. $0.6 \leq |\eta^{1st(2nd)}| < 1.2$

    3. $1.2 \leq |\eta^{1st(2nd)}| < 1.8$

    4. $1.8 \leq |\eta^{1st(2nd)}| < 2.5$ [5]

    the fraction of events per $|\eta^{1st(2nd)}|$ bin is evaluated for regions i=A,C,E:

$$f_i^{backgr}(\eta^{1st(2nd)}) \tag{5.6}$$

- The weight factors are constructed such that the fraction of events per $|\eta^{1st(2nd)}|$ bin in the 0 and 1-tag region is corrected to match the corresponding fraction in the 2-tag bin:

$$w_{0-tag,1-tag}(\eta^{1st(2nd)}) = \frac{f_E^{backgr}(\eta^{1st(2nd)})}{f_{A,C}^{backgr}(\eta^{1st(2nd)})} \tag{5.7}$$

Before building the background distributions according to formula 5.3 the weight factors are applied to the background events in region B and D, depending on the $|\eta|$ of the leading (and subleading) jet per event. The effect of the reweighting procedure is illustrated by means of the leading and subleading jet η distributions in Figure 5.7: shown are the data vs. Monte-Carlo simulation+background distributions (first and third row) and the corresponding η shapes expected for background events in regions B (0-tag), D (1-tag) and the signal region (second and fourth row). The original distributions are shown in the left column, the middle and right column plots illustrate the shapes after applying the weight factors $w(|\eta^{1st}|)$ and $w(|\eta^{1st}|,|\eta^{2nd}|)$, respectively. As expected by construction of the weight factors, the data vs. Monte-Carlo simulation+background agreement is largely improved for the leading jet η after applying the weight factors $w(|\eta^{1st}|)$ - achieved by reweighting the shapes in regions B and D, whereas the subleading jet η distribution remains unchanged. The same effect can be achieved for the subleading jet η when using the weight factors which are parameterised as as function of $|\eta^{1st}|$ and $|\eta^{2nd}|$: $w(|\eta^{1st}|,|\eta^{2nd}|)$.

---

[4]using regions A, C and E instead of B, D and F allows to derive the weight factors without making use of the signal region F

[5]Jets with $|\eta| \geq 2.5$ are rejected corresponding to the object quality criteria.
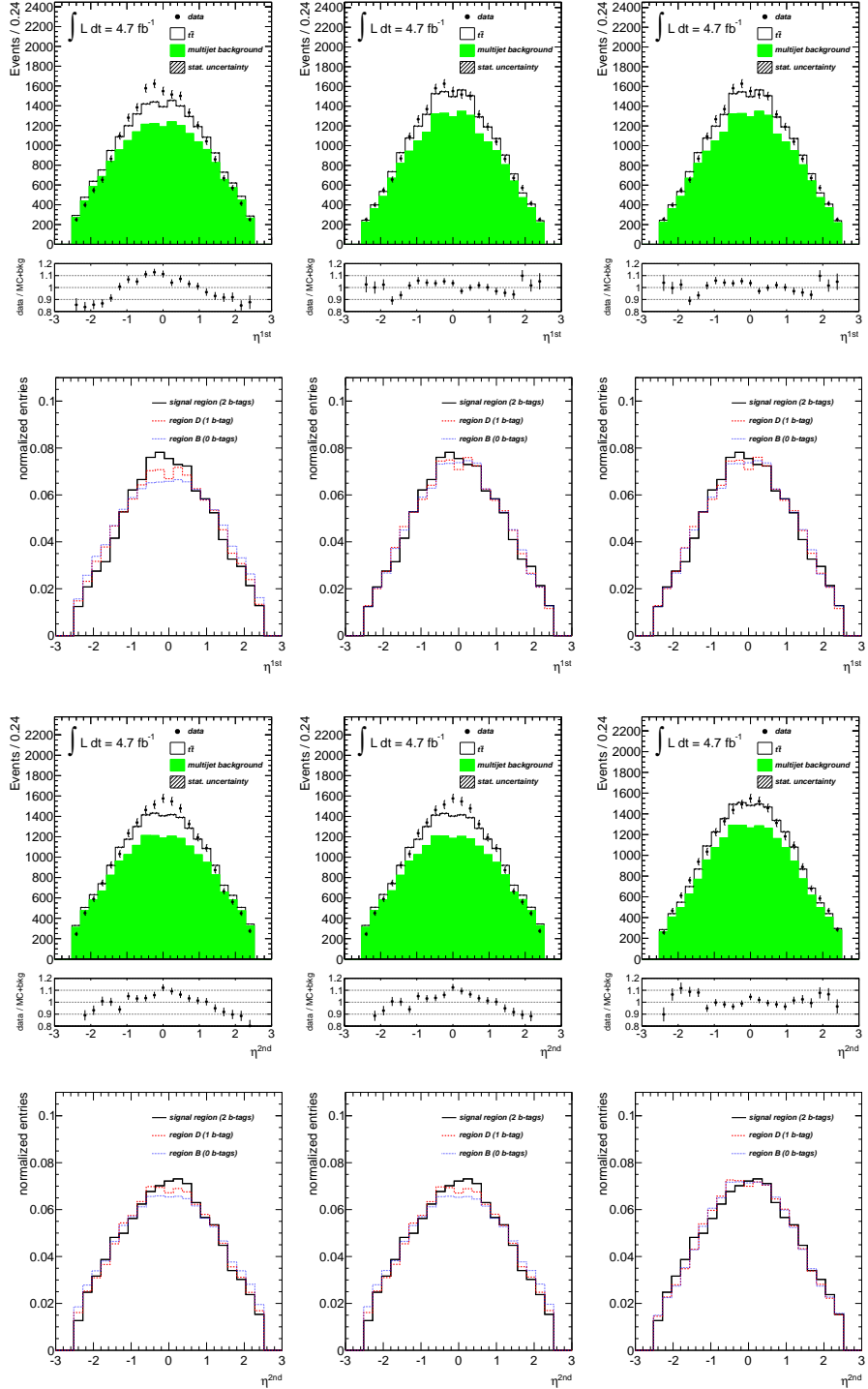
Figure 5.7.: Data vs. Monte-Carlo simulation+background jet η distributions for the leading (first row) and subleading (third row) jet. Also shown are the corresponding η shapes expected for background events in regions B (0-tag) and D (1-tag) as well as in the signal region (second and fourth row). The original distributions are shown in the left column, the middle and right column plots illustrate the shapes after applying the weight factors $w(|\eta^{1st}|)$ (middle) and $w(|\eta^{1st}|, |\eta^{2nd}|)$ (right) to the background distributions.
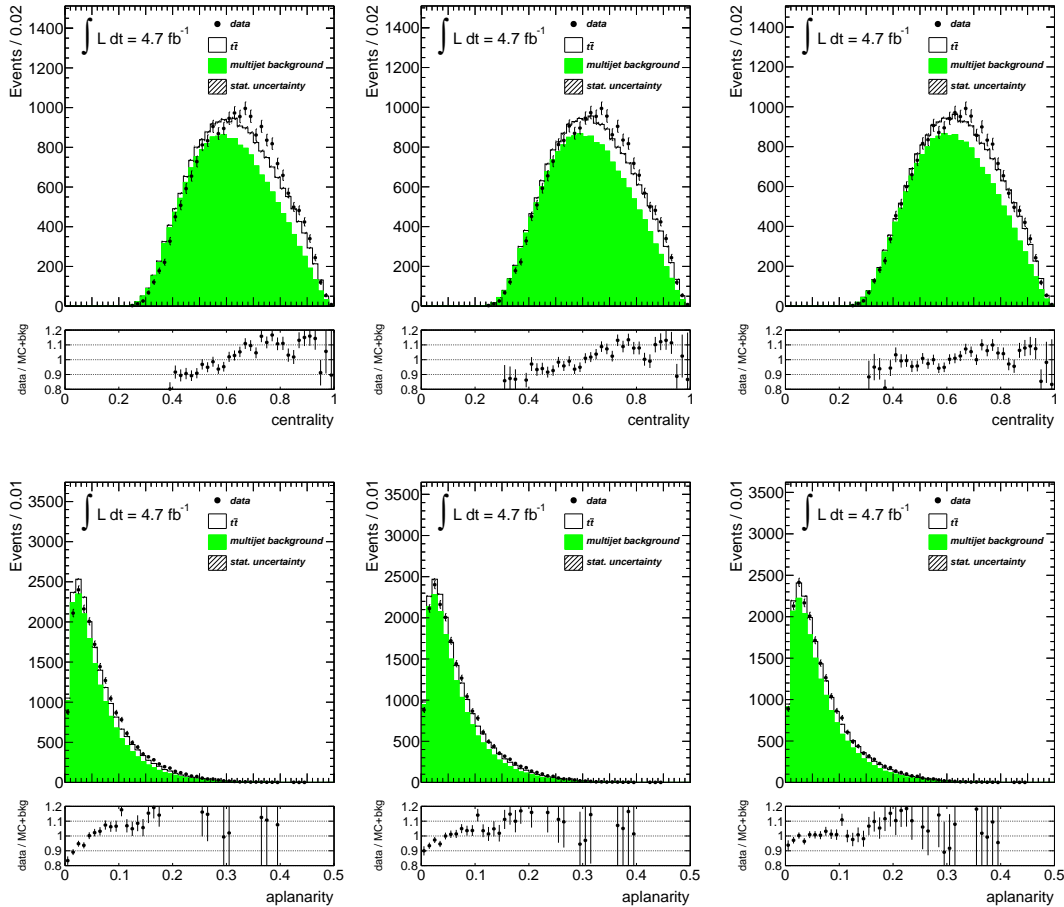
Figure 5.8.: Data vs. Monte-Carlo simulation+background centrality (first row) and aplanarity (second row) distributions. The original distributions are shown in the left column, the middle and right column plots illustrate the shapes after applying the weight factors $w(|\eta^{1st}|)$ (middle) and $w(|\eta^{1st}|,|\eta^{2nd}|)$ (right).
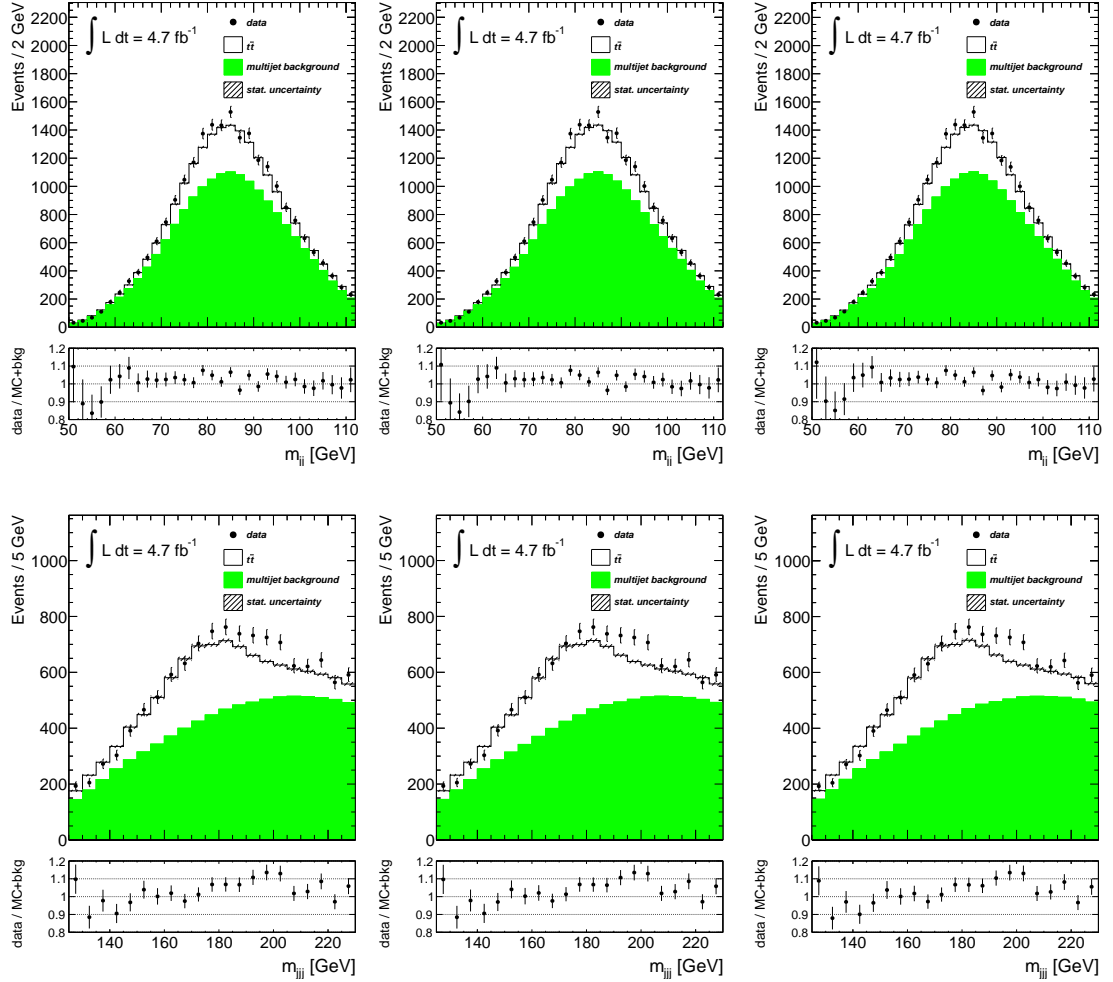
Figure 5.9.: Data vs. Monte-Carlo simulation+background m_{jj} (first row) and m_{jjj} (second row) distributions for events passing the full chain of analysis cuts. The original distributions are shown in the left column, the middle and right column plots illustrate the shapes after applying the weight factors $w(|\eta^{1st}|)$ (middle) and $w(|\eta^{1st}|, |\eta^{2nd}|)$ (right). No dependence on the η mismodelling has been observed.

Figure 5.8 illustrates the same distributions for two η dependent event shape variables: centrality and aplanarity [6]. The uncorrected distributions (left column) show a clear slope in the data vs. Monte-Carlo simulation+background ratio plots. Improved agreement is found when correcting the background shapes in the 0-tag and 1-tag bin by means of the weight factors $w(|\eta^{1st}|)$ (middle) and $w(|\eta^{1st}|, |\eta^{2nd}|)$ (right column). Further improvement on the agreement is expected when parameterising the weight factors as a function of η^{1st}-η^{4th}, i.e. including all jets considered for the *b*-tag multiplicity evaluation. For further illustration the normalised shapes of both the centrality and aplanarity distributions per *b*-tag multiplicity bin as well as the ratios of the shapes in the 2-tag bin with respect to the 0 and 1-tag bin are shown in Figure B.2.

Similar studies have been performed for the trijet and dijet invariant mass distributions, m_{jjj} and m_{jj}, the aim being to investigate how strong these distributions depend on the weight factors. The same kinematic likelihood fit as for the reconstruction of the $R_{3/2}$ variable (see Section 7.2) has been applied to assign jets to the top quark (m_{jjj}) and the W-boson (m_{jj}). By contrast to the centrality and aplanarity distributions the unweighted plots do not show a slope in the data vs. Monte-Carlo+background ratio. Also, when reweighting the background distributions (middle and right column) no clear change in the resulting shapes is visible, indicating that the variables needed for the top quark measurement are not affected by the η mismodelling. Due to this results the original, unweighted background distributions are used as input to the template method (see Section 7.3.2).

5.2.5. Background modelling performance

To investigate the performance of the background model, data vs. Monte-Carlo simulation+background comparison studies have been made. Only basic preselection criteria have been applied to data allowing to test the ABCD method in regions highly dominated by background events. Good agreement has been found for the jet kinematical distributions in Figure 5.11 and Figure 5.12. The missing transverse energy, $\phi_{\not{E}_T}$, as well as missing transverse energy significance distributions (Figure 5.10) show reasonable agreement within the $\approx 10\%$ uncertainty assigned to the MET calculation.

---

[6]Centrality is defined as the scalar sum of the transverse energy of all jets passing the event selection criteria divided by the invariant mass of these jets:

$$centrality = \frac{\sum_{jets} E_t}{M_{jets}} \tag{5.8}$$

Aplanarity is defined as 1.5 times the smallest eigenvalue of the momentum tensor

$$S^{\alpha\beta} = \frac{\sum_i p_i^\alpha p_i^\beta}{\sum_i |p_i|^2}, \tag{5.9}$$

where $\sum_i$ denotes the sum running over all selected jets and α, β are the x, y and z components of the momentum tensor. Labelling the normalised eigenvalues of equation 5.9 as $\lambda_1 \leq \lambda_2 \leq \lambda_3$ aplanarity is defined as follows:

$$aplanarity = \frac{3}{2} \times \lambda_1 \tag{5.10}$$
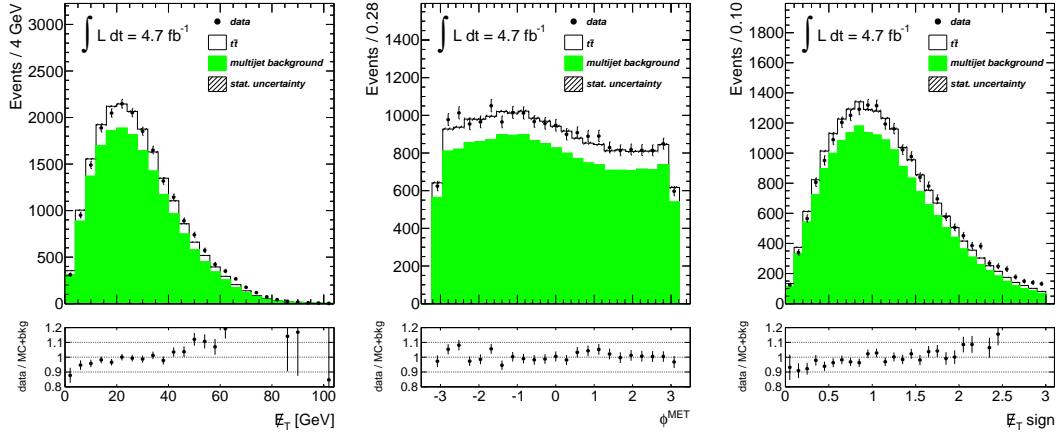
Figure 5.10.: Data vs. Monte-Carlo simulation+background comparison plots after pres-
election cuts: $\not{E}_T$ and $\phi^{\not{E}_T}$, as well as $\not{E}_T$ siginificance.

5.2.6. Systematic uncertainties on the background modelling

The background modelling in Section 5.2.2 is based on 6 regions, allowing to have one
additional region for the evaluation of the shapes and normalisation with respect to the
generic ABCD method. For the estimate of the systematic uncertainty, the background
modelling is redone using only four of the 6 regions, i.e. the shapes and normalisation in
the 2-tag signal region are extracted from

1. the 0-tag bin (regions A and B) only:

$$\frac{dn_F^{backgr}}{dx} = \frac{n_E^{backgr}}{n_A^{backgr}} \frac{dn_B^{backgr}}{dx} \tag{5.11}$$

2. the 1-tag bin (regions C and D) only:

$$\frac{dn_F^{backgr}}{dx} = \frac{n_E^{backgr}}{n_C^{backgr}} \frac{dn_D^{backgr}}{dx} \tag{5.12}$$

This procedure is motivated as follows:

- Different b-tag multiplicity requirements might lead to different contributions from,
  e.g. single top and W+jets processes (with hadronically decaying W-bosons), re-
  sulting in different background shapes per region.

- The signal Monte-Carlo sample is used to correct for the expected $t\bar{t}$ contamination
  in the 0 and 1-tag bin, introducing a small dependence on the Monte-Carlo mod-
  elling. Due to the different signal contamination in the 0 and 1-tag bin this will
  influence the shapes differently.
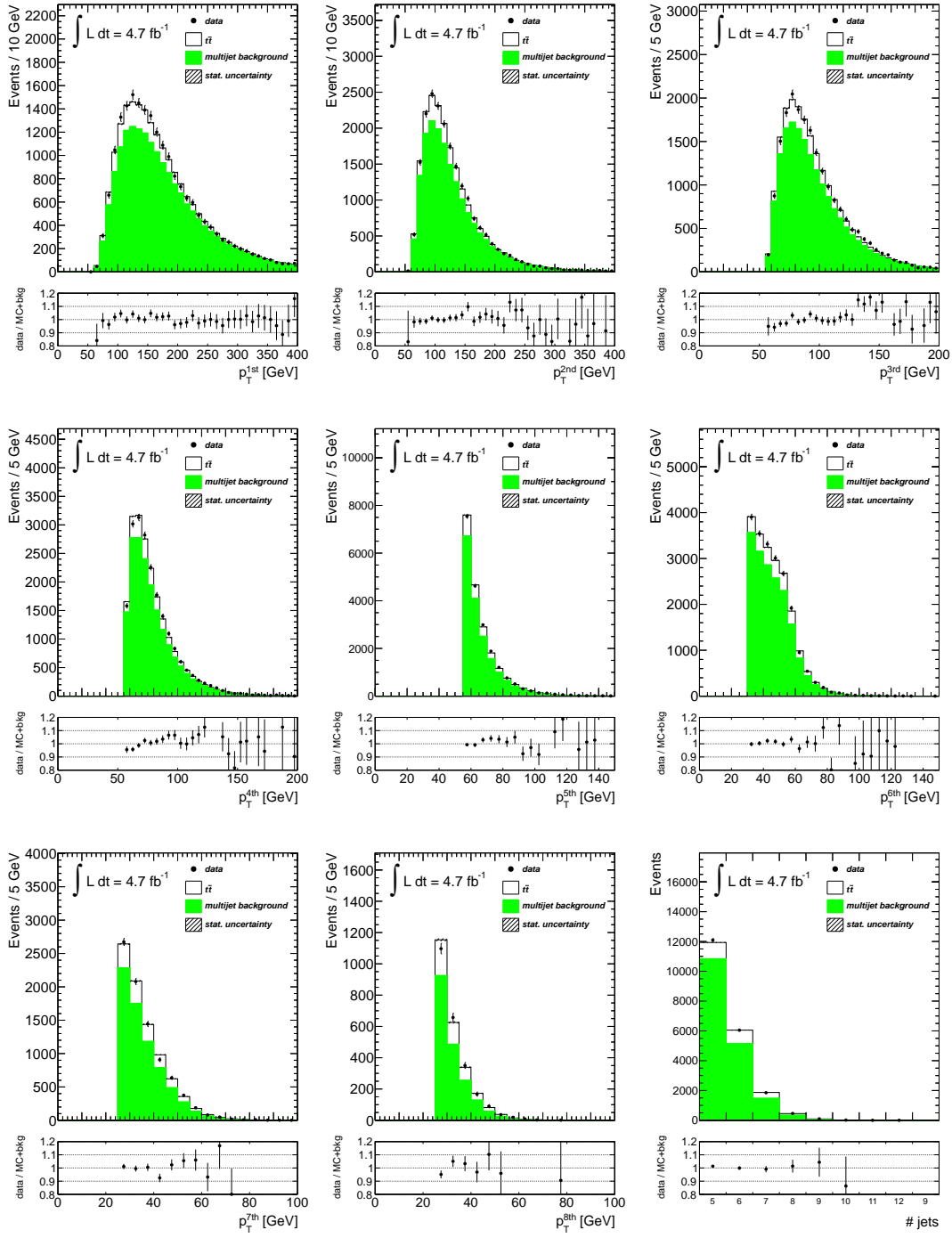
Figure 5.11.: Data vs. Monte-Carlo simulation+background comparison plots after pres-
election cuts: 1st - 8th leading jet transverse momenta as well as jet multi-
plicity distributions.
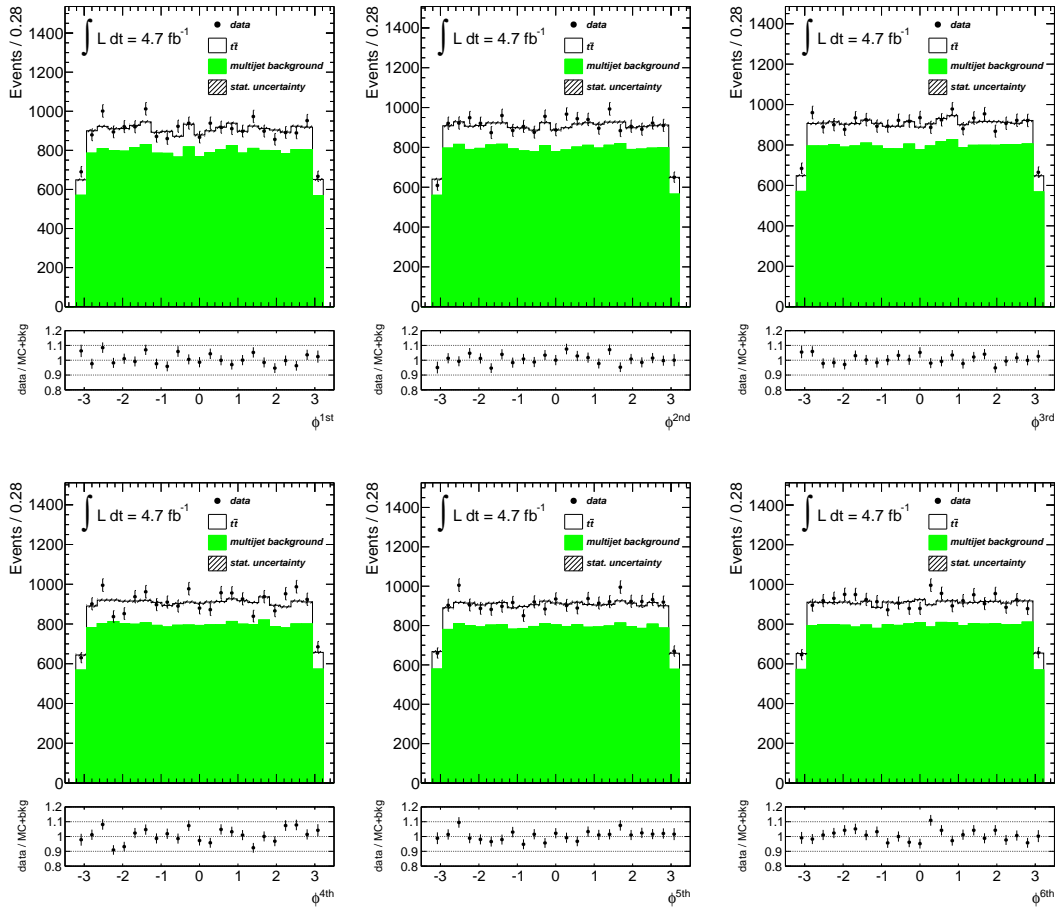
Figure 5.12.: Data vs. Monte-Carlo simulation+background comparison plots after pres-election cuts: 1st - 6th leading jet ϕ distributions.

- Possible correlations between the distribution of interest and the *b*-tag multiplicity will result in different shapes in different regions.

The above effects are expected to get visible when varying the regions considered for the background shapes and normalisation. Some of the above effects may be anticorrelated and changes in the shapes can thus partially cancel out as the different sources of uncertainty are not treated separately. To obtain a conservative estimate on the systematic uncertainty the changes in the resulting top quark mass when using formula 5.11 and 5.12 instead of the 6-region background respectively are added in quadrature.

6. Model to data comparison

The performance of the signal Monte-Carlo simulation and the background model is tested by means of control plots. All event selection criteria given in Section 4.4.3 are applied. The expected signal and background yields are given in Table 5.3 (region F). The data to Monte-Carlo simulation+background agreement has been tested for several kinematic variables and event observables. In addition, reconstructed quantities have been investigated which are obtained by means of a kinematic likelihood fit (see Section 7.2), allowing to reconstruct the $t\bar{t}$ decay and to associate jets with either of the top quarks. On overall, nearly all distributions under investigation have been shown to be well modelled by the signal Monte-Carlo simulation and the data-driven background model.

Figures 6.1, 6.2 and 6.3 illustrate the p_T, η and ϕ distributions of the six leading jets. Good agreement is observed for the p_T and ϕ distribution, while the η distributions show some deviation between Monte-Carlo simulation+background and data. This effect has however been investigated in Section 5.2.4 and has been understood to be a consequence of the η-dependent b-tagging efficiency. Good agreement has also been observed for the jet multiplicity and the $\not{E}_T$, and $\phi_{\not{E}_T}$ distributions (see Figure 6.4)

Figure 6.5 illustrates the trijet (m_{jjj}) and dijet (m_{jj}) invariant mass as well as the $R_{3/2}$ distribution. Good agreement is observed for the likelihood distribution. Naturally, differences between the data and Monte-Carlo simulation+background are expected for the m_{jjj}, m_{jj} and $R_{3/2}$ distributions – introduced due to differences in the top quark mass in data and the Monte-Carlo simulation input top quark mass of 172.5 GeV. In addition, the distance in the η-ϕ plane between the jets of the dijet system has been investigated in Figure 6.6. Similarly, the maximum distance between any jet-pair of the trijet system is shown. Finally, the p_T of the dijet and trijet system has been evaluated. Good agreement is found for all kinematical distributions of the reconstructed dijet and trijet systems.

The number of primary vertices per event as well as the average number of interactions per bunch crossing ($\langle\mu\rangle$) is shown in Figure 6.7, where both quantities are sensitive to the pile-up conditions as outlined in Section 3.2.5. The plots are obtained after applying reweighting factors to simulated events to match the pile-up conditions in the data [94]. Good agreement is found for both distributions.
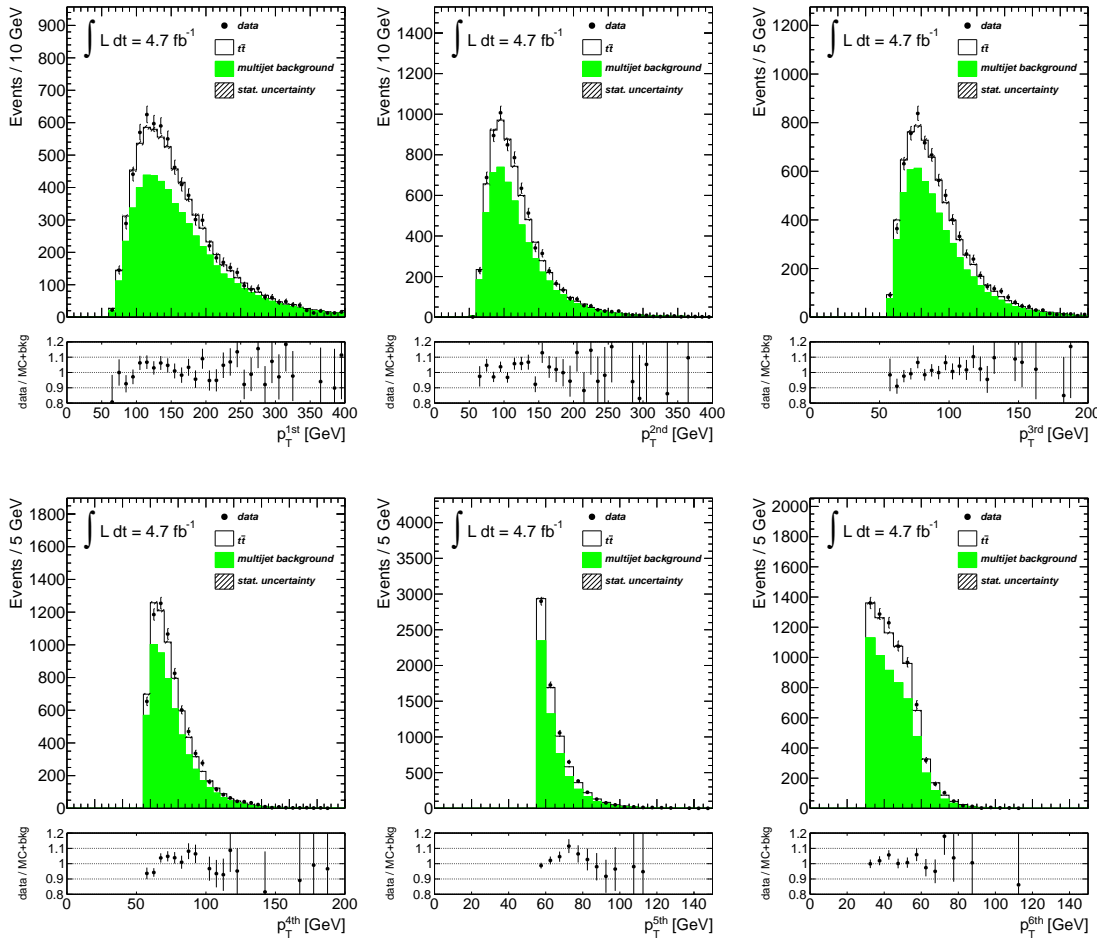
Figure 6.1.: Data vs. Monte-Carlo simulation+background jet p_T distributions after applying all analysis event selection criteria - the distributions are shown separately for the 1st - 6th leading jet.
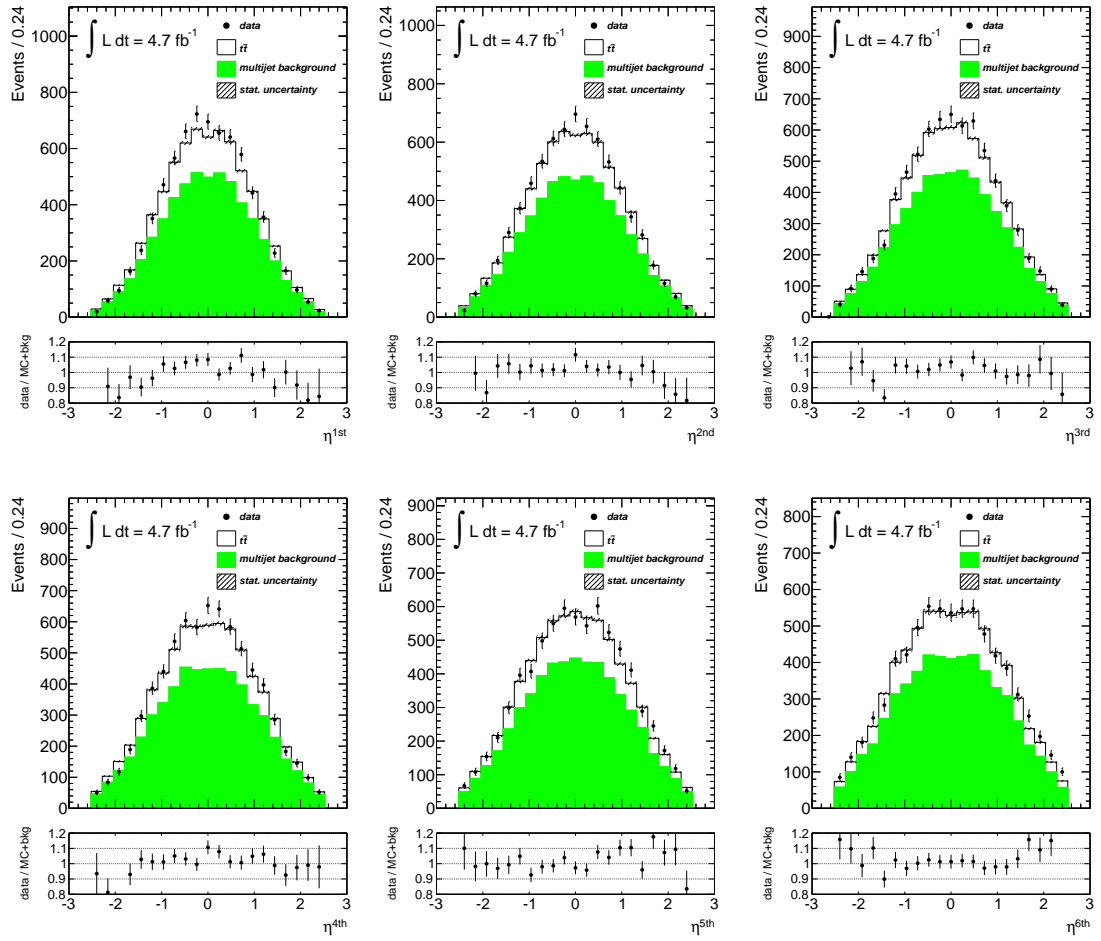
Figure 6.2.: Data vs. Monte-Carlo simulation+background jet η distributions after applying all analysis event selection criteria - the distributions are shown separately for the 1st - 6th leading jet.
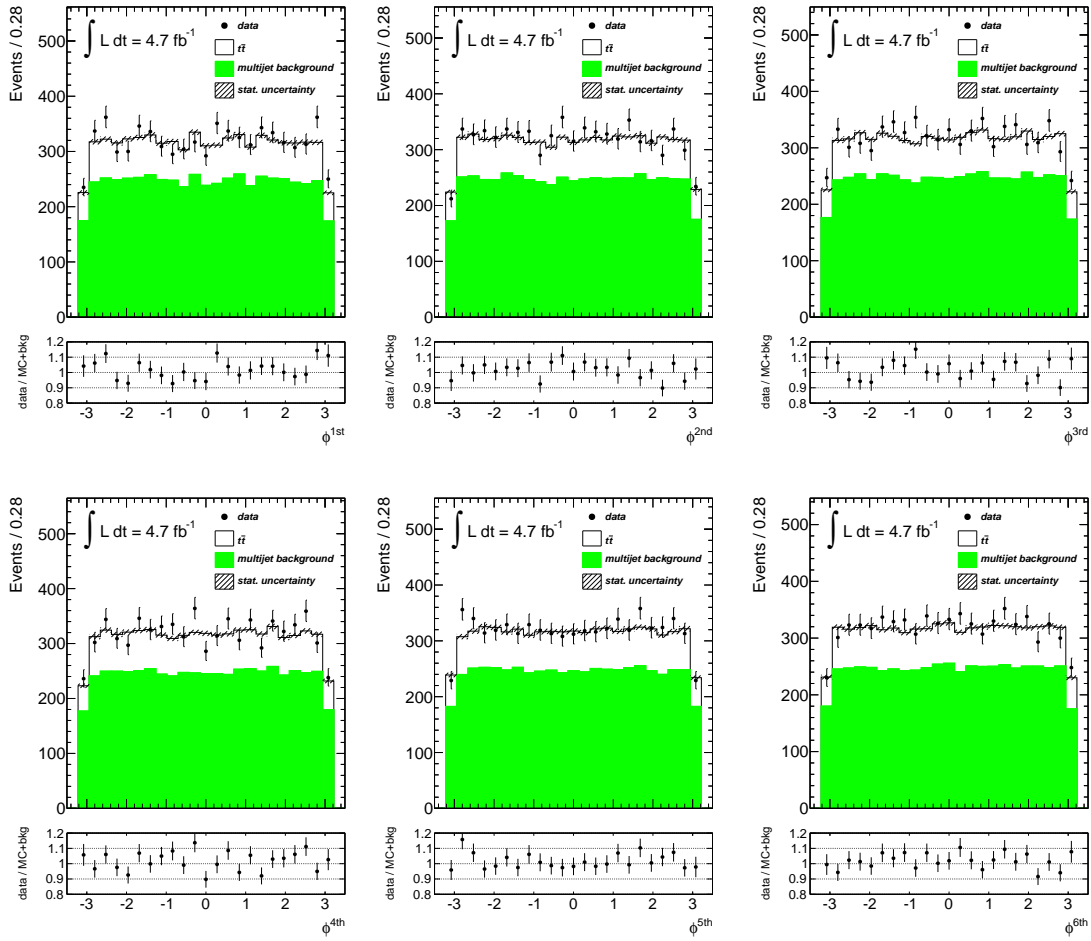
Figure 6.3.: Data vs. Monte-Carlo simulation+background jet ϕ distributions after applying all analysis event selection criteria - the distributions are shown separately for the 1st - 6th leading jet.
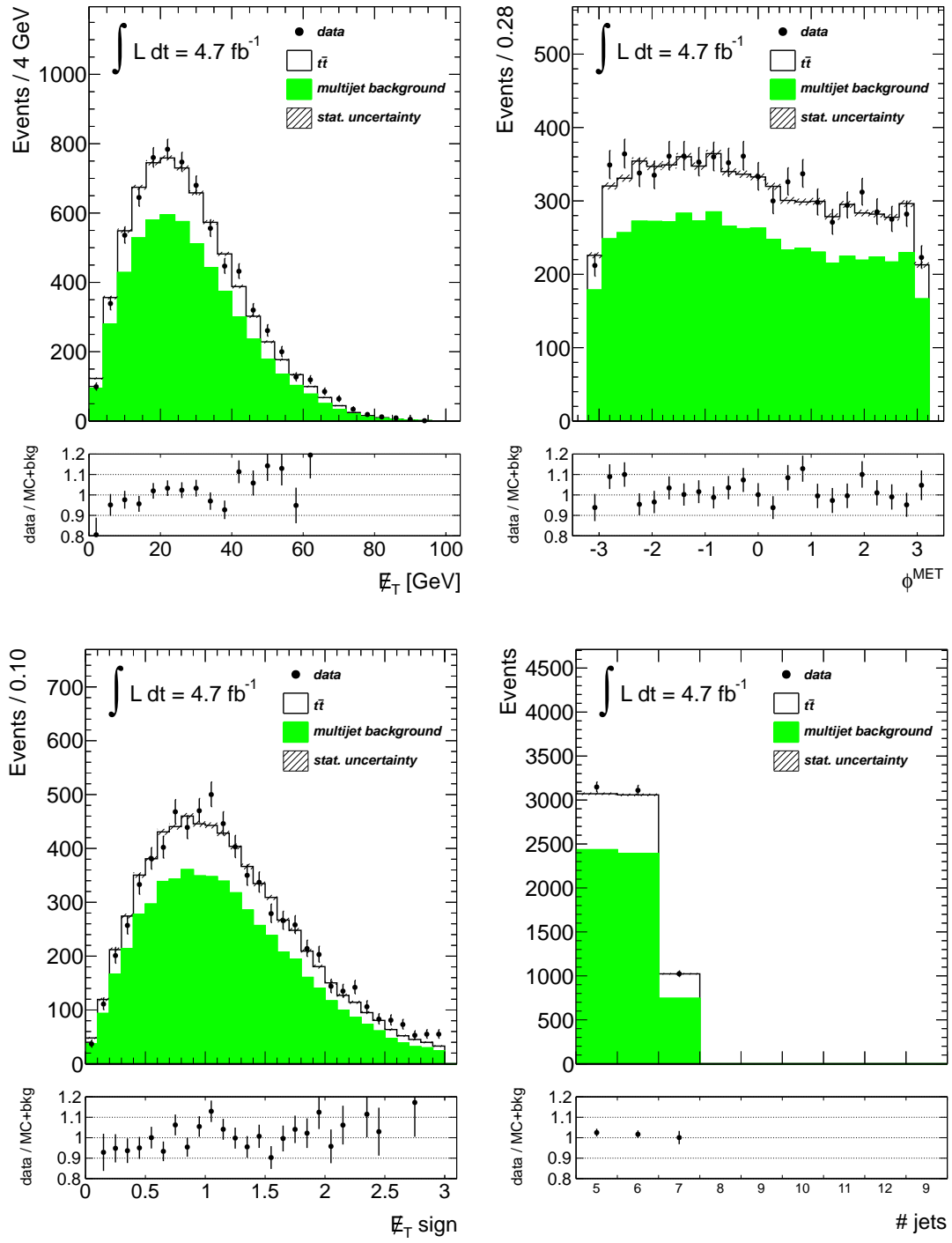
Figure 6.4.: Data vs. Monte-Carlo simulation+background jet multiplicity and $\not{E}_T$, ϕ angle of the missing transverse energy and $\not{E}_T$-significance distributions after applying all analysis event selection criteria.
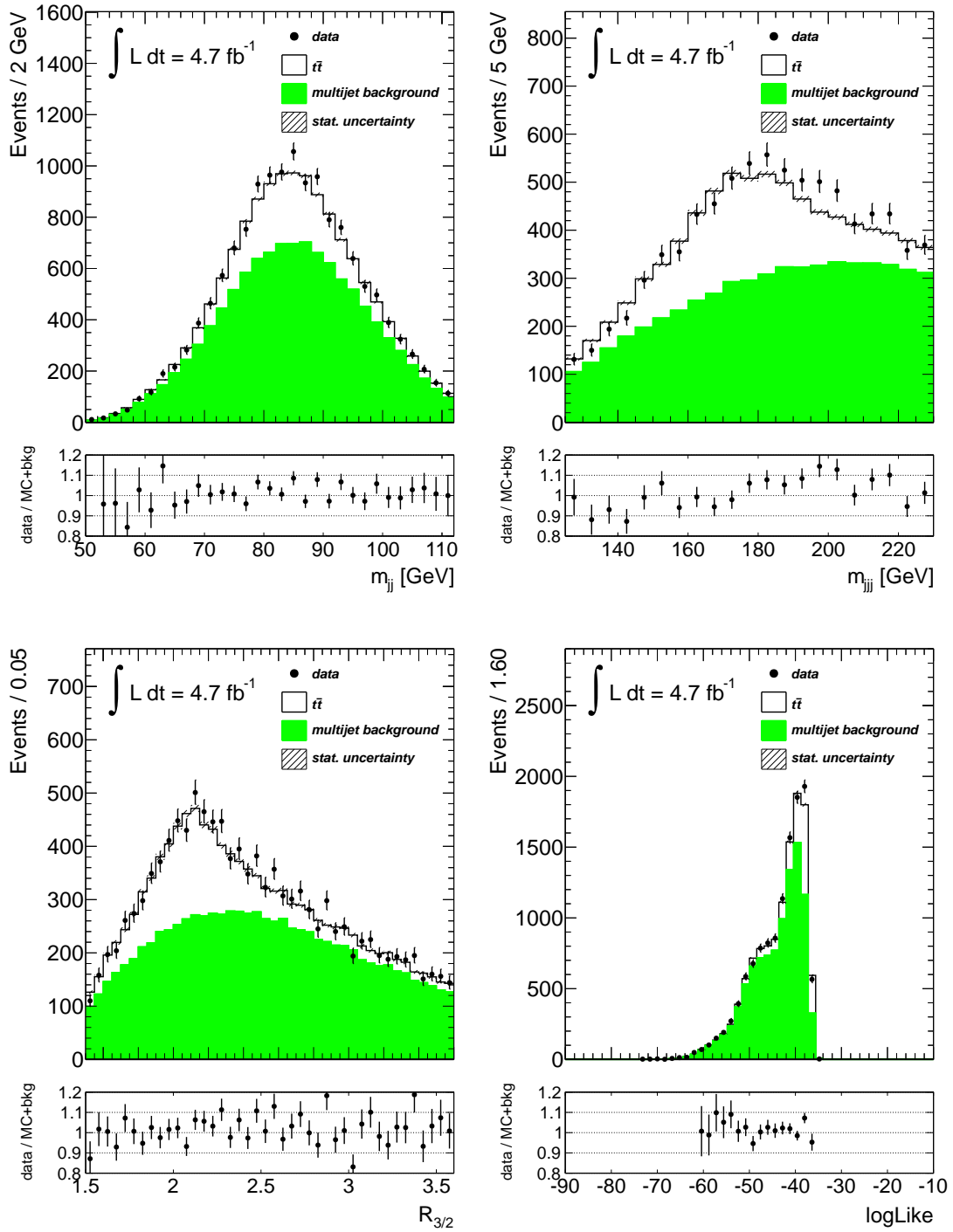
Figure 6.5.: Data vs. Monte-Carlo simulation+background m_{jj}, m_{jjj} and $R_{3/2}$ distributions after applying all analysis event selection criteria. Also shown is the likelihood distribution obtained from the kinematic likelihood fit, where all analysis selection criteria but the likelihood cut have been applied.
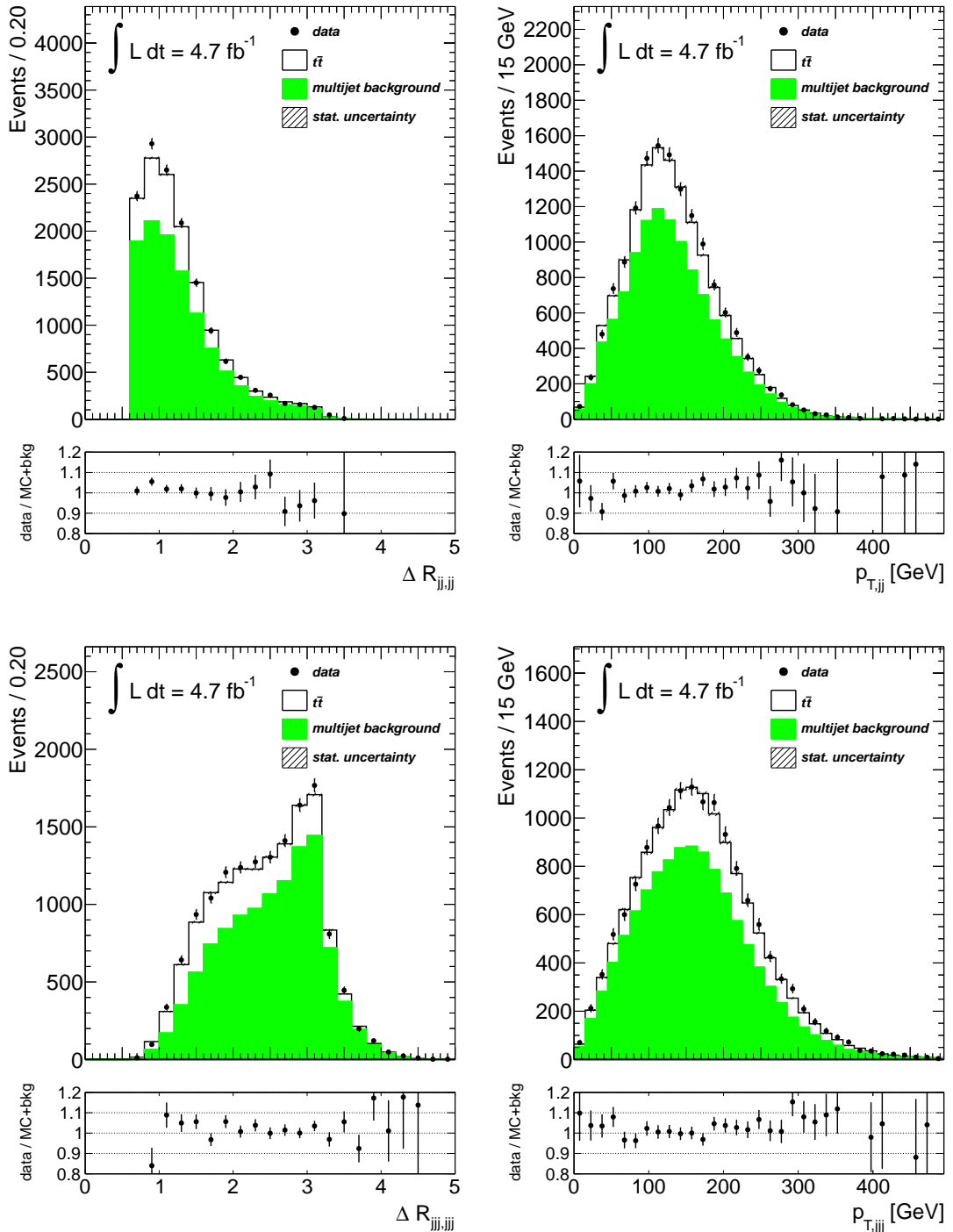
Figure 6.6.: Data vs. Monte-Carlo simulation+background kinematical distributions of the reconstructed dijet and trijet system. Shown is the distance between the jets of the dijet system as well as the maximum distance between any jet-pair of the trijet system. In addition, the transverse momenta of the reconstructed dijet and trijet system are illustrated.
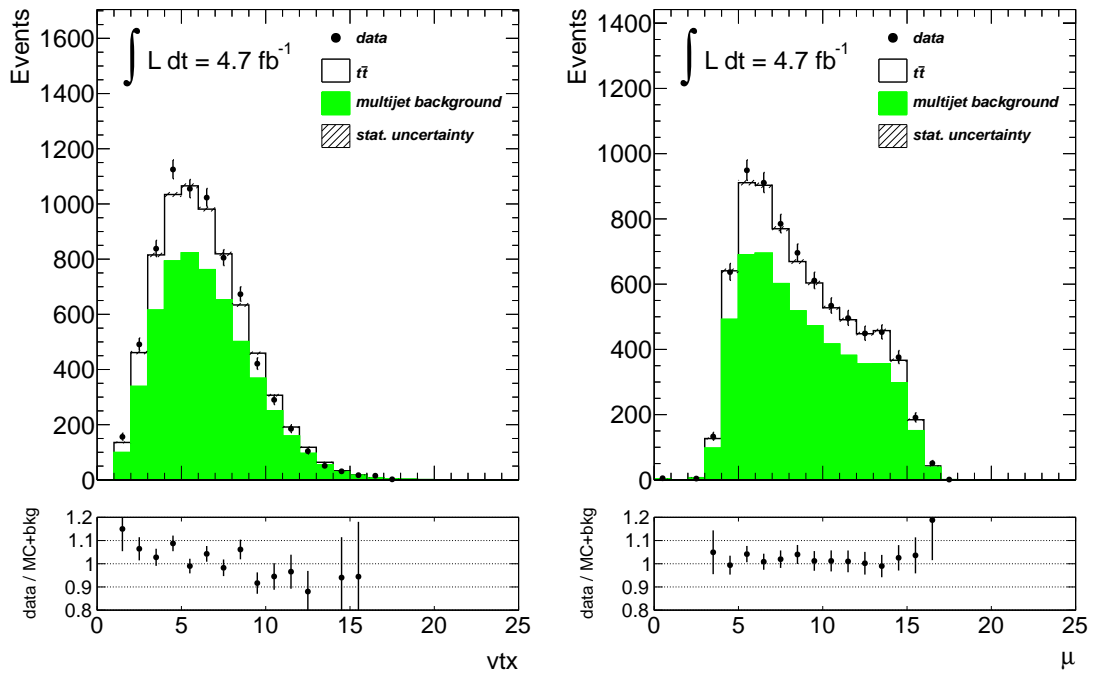
Figure 6.7.: Data vs. Monte-Carlo simulation+background distributions showing the number of reconstructed primary vertices per event as well as the average number of interactions per bunch-crossing. Both distributions are obtained after reweighting the simulated events to the pile-up conditions in data.

7. The $R_{3/2}$ template method

7.1. The $R_{3/2}$ variable

The $R_{3/2}$ variable is defined as the ratio of the invariant mass of the jet-triplet associated with the top quark, divided by the invariant mass of the W-boson dijet-system:

$$R_{3/2} = \frac{m_{jjj}}{m_{jj}}. \tag{7.1}$$

The $R_{3/2}$ ratio is evaluated on an event-by-event basis, separately for each of the two hadronic top quarks per event. By construction, a notable correlation between numerator and denominator of the $R_{3/2}$ variable is expected - introduced via the W-decay jets which enter both invariant mass terms. The correlation between m_{jj} and m_{jjj} has been studied in the nominal PowHeg+Pythia signal sample (see Figure 7.1) and has been evaluated to be $\rho = 0.25$.

Using templates built from the $R_{3/2}$-variable (see Section 7.3) an improved analysis performance with respect to m_{jjj}-based templates is expected:

- Due to the correlation between m_{jjj} and m_{jj} systematic uncertainties - such as the uncertainty on the jet-energy-scale - are expected to partially cancel out.

- Shifts in the W-invariant mass spectrum with respect to the peak value - introduced, for example, via gluon radiation - translate into shifts in the top invariant mass spectrum. Thanks to the ratio such effects are expected to cancel out, leading to an improved resolution of the $R_{3/2}$ peak compared to the m_{jjj} distribution.

7.2. Reconstruction of the $t\bar{t}$ decay - kinematic likelihood fit

Since the allhadronic final state comprises 6 jets, two of which are b-quark jets and four belong pairwaise to a W boson decay, the correct assignment of these jets to the top and antitop quark is combinatorially involved. Therefore, the kinematic Likelihood Fitter (KLFitter) [95] is applied to reconstruct the fully hadronic top-antitop decays. The likelihood function 7.2 is based on the leading order $t\bar{t}$ decay scenario, resulting in 6 jets in the fully hadronic final state, two of which are b-jets, the remaining four stemming from the hadronic decay of the W-bosons. The likelihood comprises of Breit-Wigner functions - $BW\left\{m(q_{11}q_{12}) \mid m_W, \Gamma_W\right\}$, $BW\left\{m(q_{21}q_{22}) \mid m_W, \Gamma_W\right\}$, $BW\left\{m(q_{11}q_{12}b_{\text{had1}}) \mid m_{\text{top}}, \Gamma_{\text{top}}\right\}$
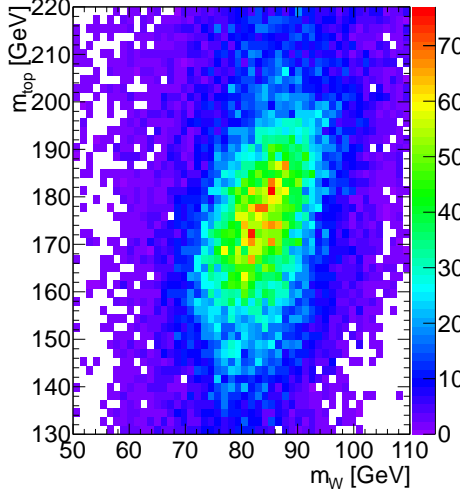
Figure 7.1.: Reconstructed W mass versus top mass - demonstrating the correlation between numerator and denominator of the $R_{3/2}$ variable.

and $BW\{m(q_{21}q_{22}b_{\text{had2}})\mid m_{\text{top}},\Gamma_{\text{top}}\}$ - modelling the mass distributions of the top quarks and W-bosons, and transfer functions relating the measured jet energies to their corresponding parton level energies:

$$
\begin{aligned}
L \;=\; & BW\{m(q_{11}q_{12})\mid m_W,\Gamma_W\}\cdot BW\{m(q_{21}q_{22})\mid m_W,\Gamma_W\}\cdot\\
& BW\{m(q_{11}q_{12}b_{\text{had1}})\mid m_{\text{top}},\Gamma_{\text{top}}\}\cdot BW\{m(q_{21}q_{22}b_{\text{had2}})\mid m_{\text{top}},\Gamma_{\text{top}}\}\cdot\\
& W\left(\tilde{E}_{\text{jet}_1}\mid E_{b_{\text{had1}}}\right)\cdot W\left(\tilde{E}_{\text{jet}_2}\mid E_{b_{\text{had2}}}\right)\cdot\\
& W\left(\tilde{E}_{\text{jet}_3}\mid E_{q_{11}}\right)\cdot W\left(\tilde{E}_{\text{jet}_4}\mid E_{q_{12}}\right)\cdot W\left(\tilde{E}_{\text{jet}_5}\mid E_{q_{21}}\right)\cdot W\left(\tilde{E}_{\text{jet}_6}\mid E_{q_{22}}\right)
\end{aligned}
\tag{7.2}
$$

The *Breit-Wigner functions* representing the W-boson mass distribution - $BW\{m(q_{11}q_{12})\mid m_W,\Gamma_W\}$ and $BW\{m(q_{21}q_{22})\mid m_W,\Gamma_W\}$ - are fixed to the W-mass PDG value of $m_W^{PDG}=80.4$ GeV and a corresponding width of $\Gamma_W=2.1$ GeV. The Breit Wigner functions representing the top quarks - $BW\{m(q_{11}q_{12}b_{\text{had1}})\mid m_{\text{top}},\Gamma_{\text{top}}\}$ and $BW\{m(q_{21}q_{22}b_{\text{had2}})\mid m_{\text{top}},\Gamma_{\text{top}}\}$ - are required to be equal in mass m_{top} and width Γ_{top}. No further constraint is applied to m_{top} which is treated as a free parameter in the likelihood fit - with the width Γ_{top} floating according to [14]:

$$
\Gamma_t=\frac{G_F m_{\text{top}}^3}{8\pi\sqrt{2}}\left(1-\frac{M_W^2}{m_{\text{top}}^2}\right)^2\left(1+2\frac{M_W^2}{m_{\text{top}}^2}\right)\left[1-\frac{2\alpha_s}{3\pi}\left(\frac{2\pi^2}{3}-\frac{5}{2}\right)\right]
\tag{7.3}
$$

The *transfer functions* - $W\left(\tilde{E}_{\text{jet}_i}\mid E_{q_{kl}}\right)$ - are parameterised by double Gaussian functions:

$$
W(E_{\text{truth}},E_{\text{reco}})=\frac{1}{\sqrt{2\pi}(p_2+p_3 p_5)}\left(e^{-\frac{(\Delta E-p_1)^2}{2p_2^2}}+p_3 e^{-\frac{(\Delta E-p_4)^2}{2p_5^2}}\right)
\tag{7.4}
$$

where $\Delta E = \frac{E_{\text{truth}} - E_{\text{reco}}}{E_{\text{truth}}}$ is the relative difference between the measured (fully calibrated) jet energy (E_{reco}) and the corresponding parton level energy (E_{truth}). The parameters p_i depend either linearly on E_{truth} ($p_i = a_i + b_i E_{\text{truth}}$) or are proportional to the inverse of the square-root of E_{truth} ($p_i = a_i / \sqrt{E_{\text{truth}}} + b_i$). The transfer functions are derived separately for light and b-jets in a PowHeg+Pythia $t\bar{t}$ sample only including lepton+jets and dileptonic events. Jets are assigned to partons if $dR(\text{jet}, \text{parton}) = \sqrt{\Delta\eta^2 + \Delta\phi^2} < 0.3$. To extract the MC based $\frac{E_{\text{truth}} - E_{\text{reco}}}{E_{\text{truth}}}$ distributions only jet-parton pairs are considered where the matching is unique, i.e. exactly one jet is found within dR<0.3 of exactly one parton. The parameters a_i and b_i are extracted by means of a global fit, i.e. their values are optimised such that the resulting double Gaussian functions match the $\frac{E_{\text{truth}} - E_{\text{reco}}}{E_{\text{truth}}}$ distributions over the full E_{truth} range.

For each jet-parton combination the jet energies are varied according to the $\frac{E_{\text{truth}} - E_{\text{reco}}}{E_{\text{truth}}}$ distributions encoded in the transfer functions - correcting the dijet and trijet invariant masses back to parton level to match the Breit-Wigner constraints of both top quarks and W-bosons. The maximisation of the logarithmic likelihood function with respect to the 6 jet energies and the top Breit-Wigner mass - serving as free parameters in the likelihood fit - is performed using the Bayesian Analysis Toolkit (BAT) [96]. Jets are associated with the W-bosons and top quarks according to the permutation maximising the likelihood value.

The likelihood function is symmetric under the exchange of the two jets stemming from the hadronic W-decay as well as under exchange of the jet triplets associated with each of the two top quarks. In a 6-jet event this translates into 90 ways of assigning jets to the 6 (LO) $t\bar{t}$ final state partons. In a 7-jet event there are already 180 such combinations, where the number of unique combinations steadily grows with increasing jet multiplicity. To reduce the influence of combinatorial background as well as computing time, events with more than 8 jets passing all quality selection criteria are rejected in the analysis.

7.3. Building $R_{3/2}$ templates and probability density functions

Using the kinematic likelihood fit technique detailed in Section 7.2 jets are associated with the top quark decay partons. m_{jjj} and m_{jj} are computed using fully calibrated jet four vectors as input (see Section 4.3.2). The jet energies optimised according to the constraints implemented in the kinematic likelihood fit are not taken into account. Signal and background templates are fitted by probability density functions within the range $1.5 \leq R_{3/2} \leq 3.6$.

7.3.1. Building signal templates

$R_{3/2}$ templates are built using PowHeg+Pythia fully hadronic $t\bar{t}$ Monte-Carlo samples, generated at 7 different top-mass point values: $m_{top}^{in,MC}$=165, 167.5, 170, 172.5, 175, 177.5
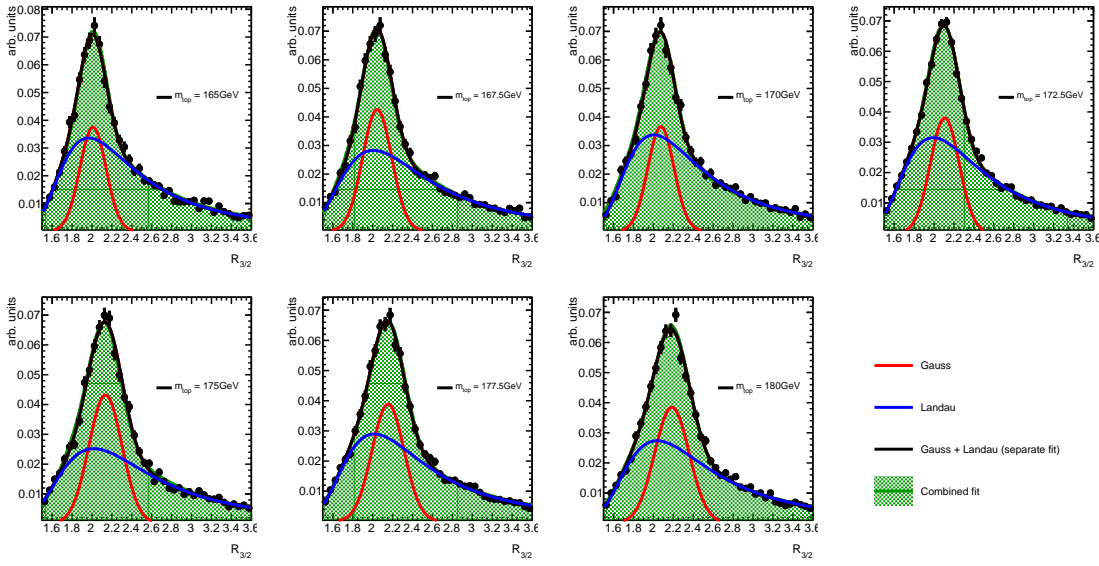
Figure 7.2.: $R_{3/2}$ templates for the 7 PowHeg+Pythia mass point samples, generated at
m_{in}^{MC} = 165, 167.5, 170, 172.5, 175, 177.5 and 180 *GeV*. Each mass point
is fitted by the combination (black) of a Gauss (red) and Landau (blue) p.d.f..
Superimposed on the templates are the shapes of the signal p.d.f. (green)
obtained when using the $p_i(m_{top}^{in,MC})$ parameterisation from the combined fit.
Good agreement with the templates is found for both the separate and com-
bined fit results.

and 180 GeV. The 7 templates are fitted by the combination of a Gauss and Landau p.d.f.
(Figure 7.2):

$$f_{fit}(p_1, p_2, p_3, p_4, p_5, p_6) = gauss(p_1, p_2, p_3) + landau(p_4, p_5, p_6). \qquad (7.5)$$

The p.d.f. parameters $p_1...p_6$ obtained when fitting each of the 7 templates separately
by formula 7.5 are plotted against $m_{top}^{in,MC}$, see Figure 7.3. All parameters are assumed
to depend linearly on the top quark mass, i.e. $p_i = a_i + b_i \times m_{top}^{in,MC}$. The y-intercepts
$a_{1...6}$ and slopes $b_{1...6}$ fixing the linear functions are evaluated by means of a simultane-
ous (combined) fit to all mass point samples where the results on a_i and b_i obtained from
the separate fit serve as start values. The linear functions parameterising the $m_{top}^{in,MC}$ de-
pendence of p_i are plotted in Figure 7.3 - where both the result of the separate (black)
and combined (green) fit are shown. Highlighted is the graph of the Gauss mean (p_2),
for which the linear dependence on $m_{top}^{in,MC}$ is particularly pronounced. The combined fit
yields a χ^2/ndof of 1.07, with the number of degrees of freedom being taken as the num-
ber of bins within the fit range. To check the parameterisation given by the combined fit
the signal p.d.f. is evaluated at the 7 mass point values. The resulting shapes are superim-
posed on the corresponding templates in Figure 7.2. Also shown is the result when fitting
the Gauss+Landau combination separately to each mass point template. Good agreement
with the templates is found for both the separate and the combined fit.
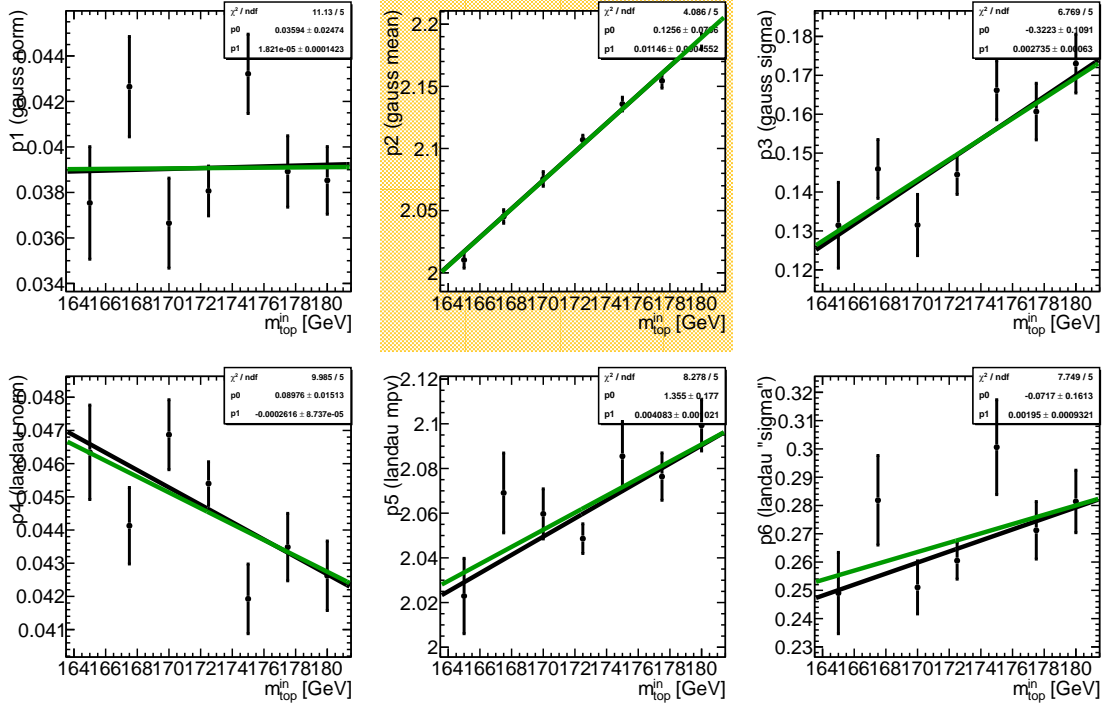
Figure 7.3.: Fit parameters as a function of the input Monte-Carlo top quark mass m_{in}^{MC}. The result of the separate fit to the seven mass point samples is shown in black. The y-intercepts and gradients evaluated in the separate fit to the mass point templates are used as starting values for the simultaneous (combined) fit to all mass point samples. The linear dependence of each parameter p_i on m_{in}^{MC} found in the combined fit is overlaid in green. The m_{in}^{MC} dependence is particularly pronounced in the case of the Gauss function mean (p_2), the corresponding graph is highlighted.

7.3.2. Building background templates

The background $R_{3/2}$ template is obtained via the ABCD method and is parameterised by means of a Landau function. The background template together with its Landau p.d.f. are shown in Figure 7.4. The $R_{3/2}$ shape distribution in multijet background events is taken to be independent of the top quark mass. Due to the data-driven background modelling technique any top quark mass dependent contribution to the background shape - such as due to hadronic single top events - is already calibrated to the top quark mass reference value in data.

7.4. The binned likelihood function

To measure the top quark mass in data a binned likelihood fit is performed. The likelihood function is built using the signal and background p.d.f.s (sections 7.3.1 and 7.3.2) and is
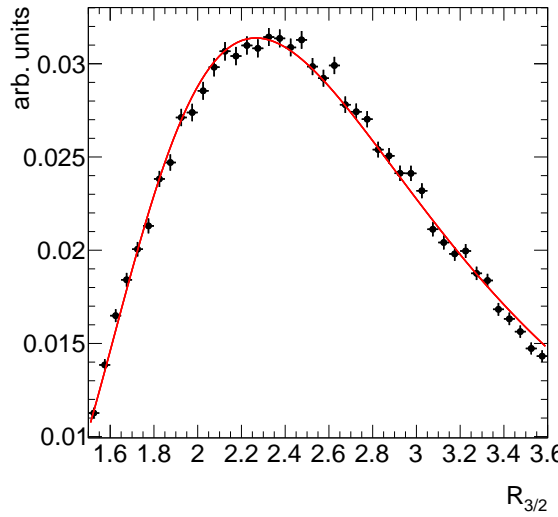
Figure 7.4.: Normalised $R_{3/2}$ distribution expected for multijet background events. The distribution is parameterised by a means of a Landau function.

given by:

$$\mathcal{L}(R_{3/2}|m_{top}) = \prod_{j}^{bins} \left(\frac{\lambda_j^{N_{obs,j}}}{N_{obs,j}!} \right) \exp(-\lambda_j) \tag{7.6}$$

where $N_{obs,j}$ and λ_j are the observed and expected number of entries in the j-th bin. The number of expected entries in the j-th bin comprises signal and background events and can be written as

$$\lambda_j = (1 - f_{back})N_{s,j}(m_{top}) + f_{back}N_{b,j}, \tag{7.7}$$

where the bin-wise number of signal and background events - $N_{s,j}(m_{top})$ and $N_{b,j}$ - is given by the signal and background p.d.f.s, evaluated at the centre of the j-th bin. Statistical fluctuations in the bins are assumed to be of Poisson nature. The background fraction f_{back} as well as the top quark mass m_{top} are taken as free prameters in the likelihood fit. The likelihood function is maximised to find the top quark mass and background fraction giving the p.d.f.s which best describe the data. The results obtained when applying the binned likelihood fit to the data are summarised in Chapter 10.

7.5. Method validation

The likelihood function (formula 7.6) is built using probability density functions parameterising the signal and background templates. Using p.d.f.s which are not in perfect agreement with the templates can give rise to biases in the measured top quark mass. In particular, all signal p.d.f. parameters are assumed to depend linearly on the top quark mass, which needs to be shown to give a reasonable description of the top mass dependent signal shapes.

To validate the template method, pseudo experiments (PEs) are performed where pseudodata are built using Monte-Carlo simulation based signal and data-driven background distributions. The binned likelihood fit used to measure the top quark mass in data (see formula 7.6) is applied to the pseudodata, allowing to compare the known input top quark mass and background fraction with the result of the likelihood fit.

To investigate whether differences between the input top quark mass and the output of the pseudo experiments are compatible with statistical fluctuations, pull distributions are evaluated according to:

$$pull = \frac{m_{top}^{in,MC} - m_{top}^{out}}{\sigma_{exp}}. \tag{7.8}$$

For an unbiased method the mean of the pull distribution yields zero. In addition, the pull width allows for a check on the estimated statistical uncertainty. If deviations between the output of the PEs and the true, input values are the same as the estimated uncertainty σ_{exp} the pull width yields 1. By contrast, a pull width < 1 (> 1) corresponds to an overestimated (underestimated) statistical uncertainty.

7.5.1. Building pseudodatasets

Pseudodata are created for all 7 values of the simulated top quark mass: $m_{top}^{in,MC} = $ 165, 167.5, 170, 172.5, 175, 177.5 and 180 GeV. For each pseudodataset the number of signal and background events to be drawn from the corresponding templates is evaluated using a Poisson distribution, based on the expected signal and background yields $N_{signal,exp}$ and $N_{background,exp}$. $N_{signal,exp}$ is extracted from Monte-Carlo studies, representing the number of events after all analysis specific cuts, scaled to the data amount of L = 4.7 fb^{-1}. $N_{background,exp}$ is obtained by means of the normalisation of the ABCD method.

7.5.2. Results of pseudo experiments

For each of the 7 mass points 5000 pseudodatasets are created. The distribution of the measured top quark mass and pull obtained from the pseudodatasets generated with $m_{top}^{in,MC} = $172.5 GeV is shown in Figure 7.5. Also shown are the corresponding distributions for the background fraction (the same distributions for the remaining 6 mass points are available in Figure C.1, Figure C.2, Figure C.3 and Figure C.4). All distributions are fitted by a Gauss function where the estimated output top quark mass m_{top}^{out} (background fraction) and the mass (background fraction) pull mean per PE is given by the mean of the Gaussian fit. Accordingly, the pull width is obtained from the width of the Gauss function. To account for oversampling due to limited Monte-Carlo statistics all errors on the extracted values are corrected according to [97]

$$\sigma_{corr} = \sigma \times \sqrt{N_{signal}/(N_{data} \times (1 - f_{back}))}, \tag{7.9}$$

where N_{signal} is the number of simulated signal events, N_{data} is the number of data events and f_{back} is the expected background fraction in data.

The top quark mass as well as the pull mean and width obtained from the PEs performed at all 7 mass input values is summarised in Figure 7.6. Both the average value of $m_{top}^{in,MC} - m_{top}^{out}$ (Figure 7.6(a)) and the mass pull mean (Figure 7.6(c)) yield 0.1 ± 0.2 indicating that no significant bias has been introduced when constructing the binned likelihood function. Also shown is the measured top quark mass as a function of $m_{top}^{in,MC}$ (7.6(b)). The average pull width (Figure 7.6(d)) is 1.01 ± 0.08 and is hence compatible with 1.

The background fraction pull and the $f_{back}^{in} - f_{back}^{out}$ distributions are shown in Figure 7.7(a) and Figure 7.7(b), respectively. A slight bias is observed, with the output background fraction being 0.9% higher compared to the input one. This bias, however, has been shown to disappear when using the background p.d.f. instead of the template to generate pseudodata, indicating that the background p.d.f. does not perfectly describe the template. As no bias could be observed in the measured top quark mass, this points to the background dominated region at high $R_{3/2}$ values, which is most likely not perfectly modelled while the agreement in the top quark mass sensitive region can be assumed to be reasonably good.
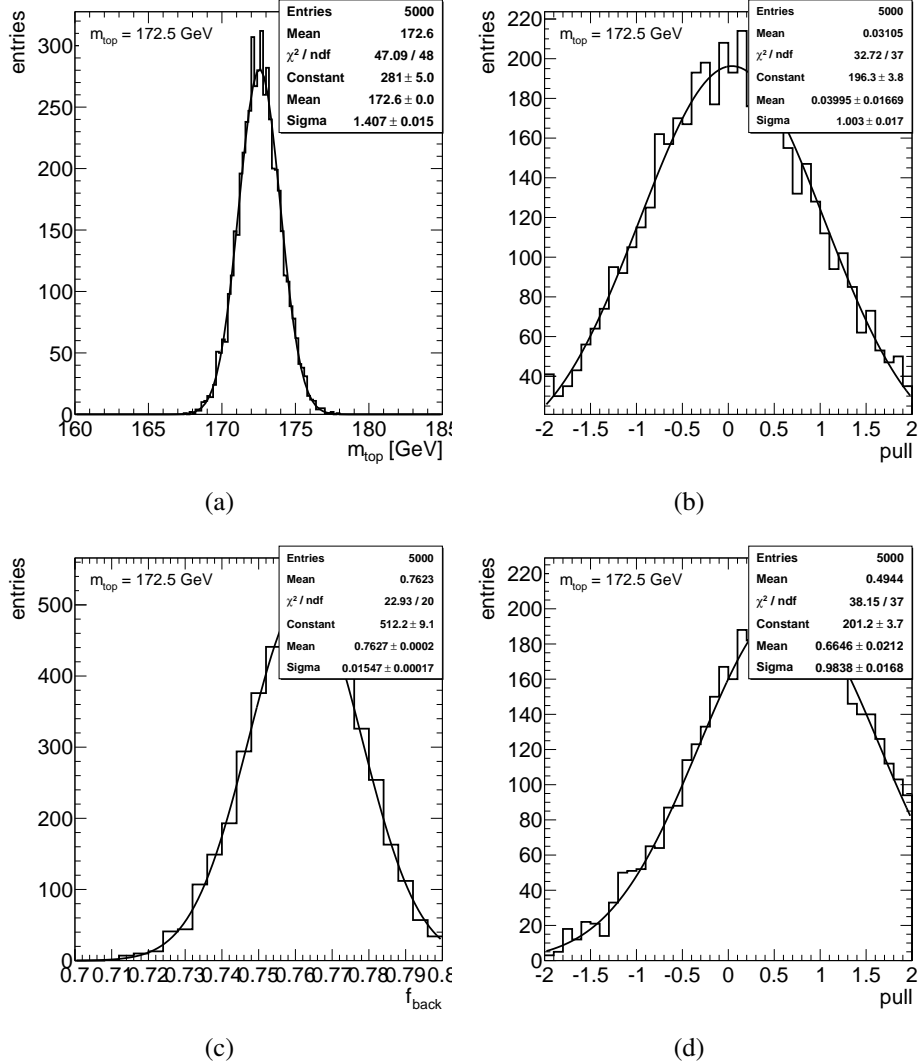
Figure 7.5.: Mass (a) and mass pull (b) distribution obtained from the pseudodatasets generated with $m_{top}^{in,MC} = 172.5$ GeV. The same distributions are shown for the fitted background fraction (c) and the background fraction pull (d). The distributions are fitted by a Gauss function. The estimated output top quark mass (background fraction) are given by the corresponding Gaussian mean. The pull width is given by the Gauss σ after being corrected for oversampling.

(a)

(b)

(c)

(d)
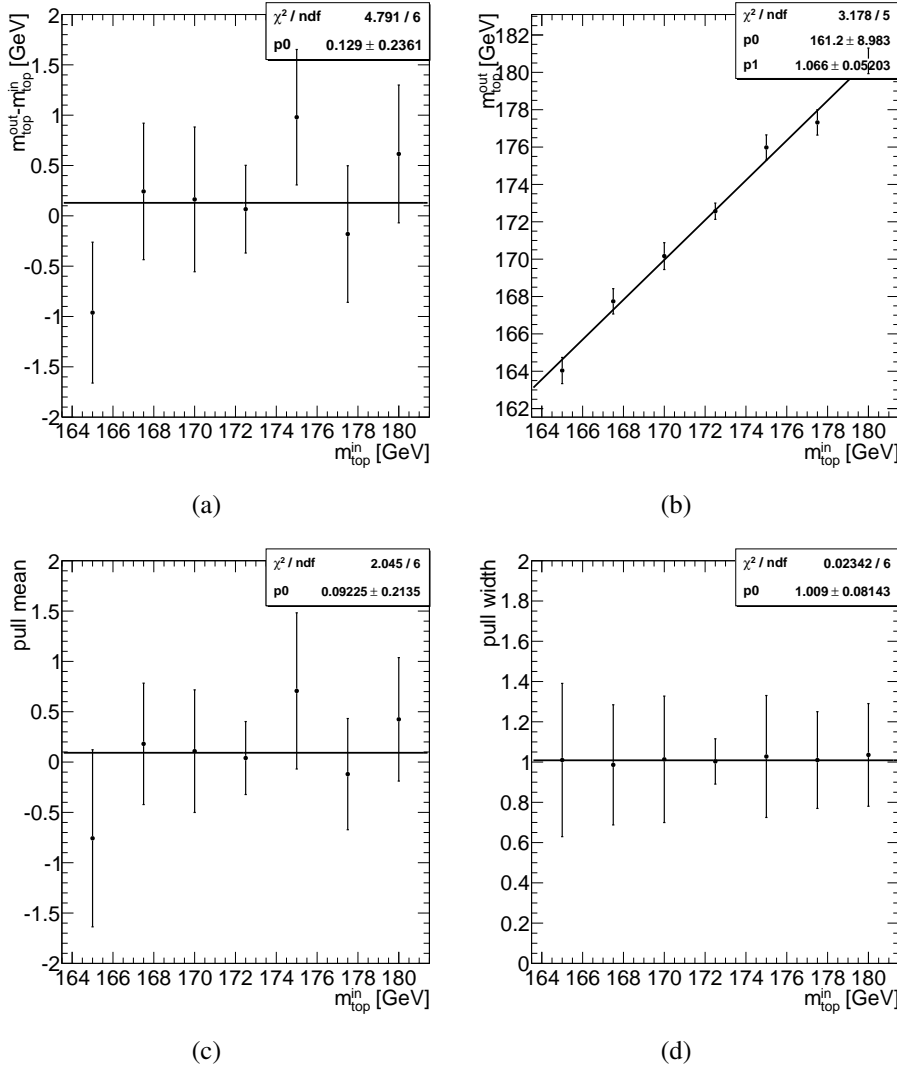
Figure 7.6.: Difference between the Monte-Carlo input top quark mass ($m_{top}^{in,MC}$) and the measured top quark mass per PE (m_{top}^{out}) as a function of $m_{top}^{in,MC}$ (a) and top mass linearity plot (b). Also shown are the mass pull mean and pull width. The input top quark mass is reproduced with no significant bias by the binned likelihood fit to the pseudodatasets. The pull width is compatible with unity, indicating that differences between the ouput mass of the PEs are compatible with the known input masses within statistical fluctuations.
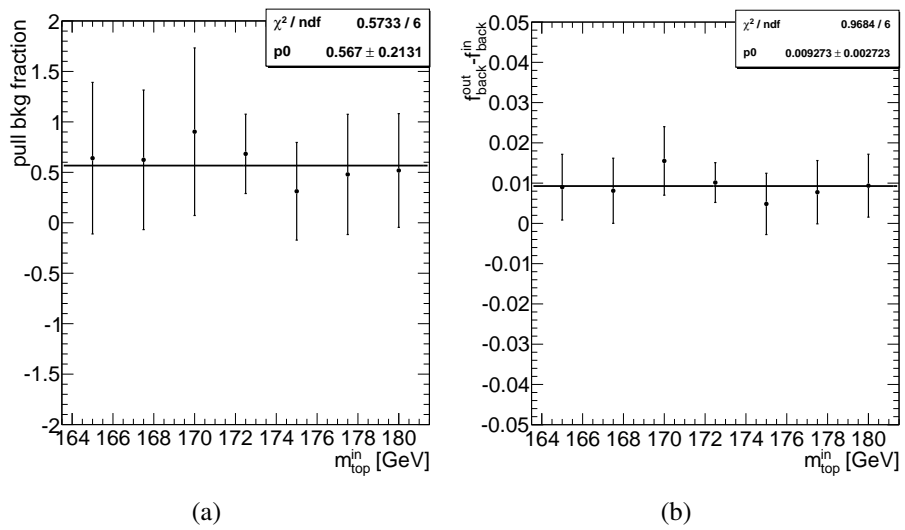
Figure 7.7.: Background fraction (a) and background fraction pull (b) per PE (m_{top}^{out}) as a function of $m_{top}^{in,MC}$.

8. Systematic uncertainties

To evaluate the precision of the $R_{3/2}$ top quark mass measurement several sources of systematic uncertainties are investigated and summarised in this chapter. The corresponding results are presented in Chapter 10 (see Table 10.1). Unless stated differently pseudo-experiments are performed, where 5000 pseudo-datasets are created according to systematically shifted templates. Similar to the procedure described in Section 7.5.1 the nominal $R_{3/2}$ parameterisation is used to measure the top quark mass for each pseudo-dataset. The systematic uncertainty on the measured top quark mass is given by the difference between the mean of the mass output of the systematically varied ensembles and the mean of the ensembles based on the nominal signal Monte-Carlo - or in some cases, another reference sample.

8.1. Systematic uncertainties related to the Monte-Carlo modelling

Approximations – zero top quark width, zero W boson width, initial and final state radiation – used in some theory calculations might affect the reconstructed top quark mass systematically. Similarly, the choice of the model used to describe non-perturbatively calculable hadronisation processes may influence the reconstructed top quark mass. The sources of systematic uncertainties related to the Monte-Carlo modelling and their influence on the measured top quark mass are given below.

8.1.1. Signal Monte-Carlo generator

To estimate the systematic uncertainty related to the choice of the signal Monte-Carlo generator templates are built from events simulated with PowHeg [78] and MC@NLO [98, 99], respectively. Both samples are generated with a top quark mass input value of m_{top} = 172.5 GeV and with the Herwig [81] program to perform parton-showering and hadronisation. The resulting top quark mass for both choices of the Monte-Carlo generator is evaluated using pseudo-experiments, where the full difference between both generators is quoted as uncertainty.

8.1.2. Hadronisation

Templates are built from events simulated with PowHeg interfaced to Herwig and Jimmy [84] with the ATLAS AUET2 [86] tune to perform parton showering and hadronisation according to the cluster model implemented in Herwig. The top quark mass

obtained from pseudo experiments is compared to the nominal case based on the string fragmentation model of Pythia, where templates built from simulated events with PowHeg and Pythia [80] with the Perugia 2011C [85] tune serve as input to pseudo-experiments. Both Monte-Carlo samples are generated with a top quark input mass of $m_{top} = 172.5$ GeV. The full difference between both choices of the parton-shower Monte-Carlo is quoted as systematic uncertainty.

8.1.3. Initial and final state radiation

The impact of initial and final state QCD radiation is assessed by building templates based on two sets of Monte-Carlo samples generated with the leading order – i.e. neither initial nor final state radiation generating – AcerMC [100], where Pythia with Perugia 2011C is used for parton showering and initial/final state radiation generation and for hadronisation. Perugia 2011C parameters sensitive to the parton shower strength are varied for both samples within a range compatible with studies detailed in [101]. The uncertainty is taken as half of the difference in the top quark mass obtained from both AcerMC samples.

8.1.4. Underlying event

Templates are built from simulated events using PowHeg and Pythia with the Perugia 2011 mpiHi ('multiple parton interaction at high luminosity') [85] tune. The mass output of pseudo-experiments is compared to the results obtained when using PowHeg+Pythia with the Perugia 2011 [85] tune[1]. Whereas the Perugia 2011 mpiHi tune leads to more semi-hard multiple parton interactions with respect to the Perugia 2011 tune the overall UE activity in the transverse region (see Section 5.1) is similar for both tunes. The uncertainty is taken as the full difference in the top quark mass obtained with both tunes. Since both samples use the same matrix element level PowHeg events statistical uncertainties on the extracted top quark mass are thus expected to be highly correlated between both samples and are hence not quoted explicitly.

8.1.5. Colour reconnection

The W bosons in the top decay are colour neutral particles while their decay products are colour charged. Since the lifetime of a W boson is shorter than the timescale for hadronisation, the W decay into quarks will happen inside the colourful parton environment, such that the colour charges of the W decay quarks might be exchanged with colour charges of the environment, which is denoted as colour reconnection.

Pseudo-experiment results from templates based on PowHeg interfaced to Pythia with the Perugia 2011 tune are compared to PowHeg interfaced to Pythia with the Perugia 2011C noCR [85] tune. The latter tune is obtained from data fits without invoking colour reconnection as stated in [85]. The Perugia 2011 noCR tune has been shown to result

---

[1]By contrast to Perugia 2011C the Perugia 2011 tune family uses the CTEQ5L [102] PDF set for parton shower and hadronisation.

in a reduced activity in the transverse region and can thus be understood to, in addition to colour reconnection systematics, assess uncertainties on the underlying event strength. The uncertainty is taken as the full difference in the top quark mass obtained from pseudo-experiments with both tunes. As both samples under study use the same matrix element level PowHeg events the statistical uncertainty on the extracted top quark mass difference is not explicitly given.

8.1.6. Fast simulation

To measure the top quark mass templates are built from samples generated using a simplified but fast simulation of the ATLAS detector. To asses the effect of calibrating the measured top quark mass to fast simulation Monte-Carlo samples, templates are generated using fast and full simulation PowHeg+Pythia events as input. Both samples are generated using an input top quark mass of m_{top} = 172.5 GeV. The full difference in the top quark mass obtained from pseudo-experiments using full and fast simulation based templates is quoted as systematic uncertainty.

8.1.7. Proton PDF

The impact of the choice of the PDF set on the signal templates has been evaluated in the lepton+jets channel [103], where a top quark mass measurement was performed using both a 2-dimensional template technique and, similar to the measurement presented in this thesis, the $R_{3/2}$ variable. The uncertainty on the PDF set was evaluated by re-weighting signal events to 22 additional PDF sets, where the resulting uncertainites yield 0.15 GeV for the $R_{3/2}$ and 0.10 GeV for the 2-dimensional analysis. As a conservative estimate twice the value obtained in the $R_{3/2}$ analysis is quoted as uncertainty.

8.2. Systematic uncertainties affecting jets

All sources of systematic uncertainties related to jets are evaluated based on the same Monte-Carlo sample (i.e. the nominal PowHeg+Pythia sample, see Section 5.1), with the quantity under investigation varied accordingly. Statistical uncertainties on the extracted top quark mass difference between the reference and systematic varied samples are thus expected to be highly correlated and are hence not quoted explicitly for these cases.

8.2.1. Jet energy scale uncertainty

The jet energy scale uncertainty comprises various nuisance parameters originating from the different in-situ techniques applied to evaluate the residual JES correction factors accounting for differences between data and Monte-Carlo simulation, see Section 4.3.2. A combination technique, detailed in [61], is applied to combine the single components according to categories which keep track on the physical meaning of the nuisance parameters. Further sources of uncertainties related to high-p_T extrapolation, intercalibration for jets with larger pseudorapidity and pile-up are also considered. Finally, topology

dependent uncertainties arising from the composition of light quark and gluon initiated jets in the analysis sample as well as uncertainties on the response of jets with nearby activity are accounted for. The evaluation of the flavour composition uncertainty for the fully hadronic $t\bar{t}$ analysis is detailed in Chapter 9. An additional uncertainty is applied to b-jets to account for differences between jets containing b-hadrons and jets originating from light quarks. The relative b-jet energy scale uncertainty was derived based on Monte-Carlo simulation studies and was validated using the comparison of track jets and calorimeter jets in the 2011 dataset [104]. More detailed information on the evaluation of the jet energy scale uncertainty is given in [61].

In total, a reduced set of 24 nuisance parameters is used to determine the JES uncertainty. Templates are built for each component, where the jet energy scale is varied by $\pm 1\sigma$ around the central value. The expected uncertainty on the top quark mass is evaluated separately for each component by means of pseudo-experiments. The total uncertainty is given by the quadratic sum of the uncertainties arising from the single components.

8.2.2. Jet energy resolution

The jet energy resolution has been measured in data and Monte-Carlo simulation using two in-situ techniques [105]. To account for the systematic uncertainty on the jet energy resolution, reconstructed jets in Monte-Carlo simulation are smeared by a Gaussian function according to the jet energy resolution uncertainty. The difference between the top quark mass measured with the smeared jet energies with respect to the nominal case is taken as systematic uncertainty.

8.2.3. Jet reconstruction efficiency

The jet reconstruction efficiency has been studied in data and Monte Carlo simulation using a tag and probe technique, where probe jets reconstructed from charged tracks in the inner detector were matched to calorimeter jets [106]. The difference in the observed jet reconstruction efficiency - defined as the fraction of probe jets matched to calorimeter jets - in data and Monte Carlo simulation is accounted for by randomly discarding jets in the nominal Monte-Carlo simulation sample within the inefficiency range. Templates are rebuilt with the uncertainty on the jet reconstruction efficiency applied, where differences with respect to the nominal case can arise due to the (slightly) changed set of events passing the analysis selection criteria.

8.2.4. Jet vertex fraction scale factor uncertainty

The hard scatter jet selection efficincy, pile-up jet rejection as well as the hard scatter jet and pile-up jet mistag rate scale factors are varied according to their uncertainties [53]. The systematic variation of the overall JVF scale factor is applied to Monte Carlo events as a function of jet p_T.

8.2.5. b-tagging efficiency and mistag rate uncertainty

The b-tagging efficiency as well as the c and light (u, d, s) jet mistag scale factors are varied according to their uncertainties [66, 67, 69]. The systematic variation of the scale factors is applied to Monte-Carlo simulation events by varying each of the three components separately by $\pm 1\sigma$ around the corresponding central value. Similarly to the nominal case the systematically shifted scale factors depend on the jet p_T, η as well as on the jet flavour.

8.3. Method calibration

To account for any possible bias arising from the choice of the probability density functions as well as from the linear top mass parameterisation of the signal templates, pseudo experiments are performed using the 7 mass point variation samples as input as detailed in Section 7.5). The average difference between the input and output top quark mass is quoted as systematic uncertainty.

8.4. Pile-up

To estimate the uncertainty due to pile-up interactions, the same reference is used as in Section 8.1.7, where an uncertainty of < 0.05 GeV is quoted for both the 2-dimensional and $R_{3/2}$ analysis [103]. The uncertainty due to additional proton-proton interactions has been investigated by repeating the top mass measurement in simulated events and data as a function of the number of reconstructed primary – i.e. collision – vertices and as a function of the average number of inelastic proton proton interactions per bunch crossing. As a conservative estimate twice the uncertainty evaluated in the lepton+jets channel is quoted as uncertainty.

8.5. Uncertainty on the background modelling

To assess the uncertainty on the background modelling the background templates are re-built using the 0 and 1-b-tag region only to extract the shapes as detailed in Section 5.2.6. The background parameterisation is redone for both cases and the top mass fit to data is repeated according to the likelihood function using the varied background p.d.f.s. The differences in the measured top quark mass using the 0-b-tag parameterisation with respect to the nominal case and the 1-b-tag parameterisation with respect to the nominal case are added in quadrature and quoted as systematic uncertainty.

9. Flavour related JES uncertainty in fully hadronic top-antitop events

9.1. Flavour response and composition uncertainty

Due to the difference in the calorimeter response of light quark and gluon initiated jets [107], uncertainties on the relative fraction of both jet flavours in the analysis sample will propagate to an uncertainty on the average flavour inclusive jet response.

The difference in the response of light quark and gluon initiated jets is closely connected to their different properties. Gluon jets tend to have a larger number of constituents [1], which is reflected in the larger number of tracks associated with gluon initiated jets. In addition, gluon jets on average have a wider angular energy profile compared to light quark jets. Particles in light quark jets therefore have a harder p_T spectrum resulting in a higher response in the calorimeter. Thus, if the predicted fraction of light quark jets in the Monte-Carlo simulation is smaller with respect to the data, the average jet response in the Monte-Carlo sample will be smaller compared to the data and vice verse, see Figure 9.1.

Assuming that the JES is established for quark jets due to the in-situ techniques applied, the flavour related uncertainty $\Delta \mathcal{R}_s$ can be written as [61]:

$$\Delta \mathcal{R}_s = \Delta f_g \times (\mathcal{R}_q - \mathcal{R}_g) \oplus f_q \times \Delta \mathcal{R}_g,\,^2 \tag{9.1}$$

where f_g and Δf_g are the fraction of gluon initiated jets and its uncertainty and $\mathcal{R}_q$ and $\mathcal{R}_g$ respresent the response of light quark and gluon initiated jets, respectively. The term $f_q \times \Delta \mathcal{R}_g$ accounts for the uncertainty on the response of gluon jets which has been evaluated by comparing the response of gluon initiated jets in samples simulated with Pythia and Herwig++ [108]. The response difference between light quark and gluon initiated jets in the central region $|\eta| < 0.8$ for both Monte-Carlo samples is shown in Figure 9.2. As the uncertainty on heavy flavour jets is evaluated separately the uncertainty on the gluon jet fraction only includes gluon and light quark initiated jets.

---

[1]In the parton shower process, gluons can either radiate a further gluon $g \to gg$ or split into a quark-antiquark pair $g \to q\bar{q}$, while in the case of quarks the only possiblity is $q \to gq$. The highest coupling strength is given for the triple gluon vertex $g \to gg$ resulting in a higher number of particles produced in the parton shower for gluon jets.

[2]$\oplus$ means that both terms are added in quadrature.
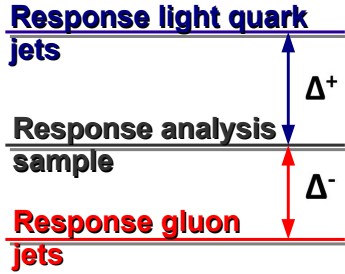
Figure 9.1.: As gluon initiated jets have a higher calorimeter response with respect to light quark initiated jets the average, flavour inclusive jet response depends on the flavour composition of jets in the analysis sample. Denoting Δ^+ / Δ^- as the difference between the response of a pure sample of light quark / gluon initiated jets and the average response in the analysis sample any change in the relative composition of both jet flavours will result in a change in Δ^+ / Δ^- and will thus shift the average sample response upwards (lower fraction of gluon initiated jets) or downwards (larger fraction of gluon initiated jets).

The flavour related uncertainty depends strongly on the analysis sample under study. The fraction of gluon initiated jets in fully hadronic $t\bar{t}$ signal events is, for instance, expected to be smaller compared to its background events originating from QCD multijet production. In addition, analysis specific cuts may alter the gluon jet fraction. The evaluation of the flavour composition uncertainty for the top quark measurement in the fully hadronic decay channel is detailed in this chapter.

9.2. Flavour composition uncertainty in fully hadronic $t\bar{t}$ events

To study the properties of light quark and gluon initiated jets in simulated $t\bar{t}$ events, the following jet-flavour labelling scheme is applied: Calorimeter jets are matched to the closest particle jet within $\Delta R = 0.3$. The particle jets are then matched to the highest energy parton within[3] $\Delta R = 0.4$. This matching scheme follows the procedure described in [107]. As stated in this reference, this definition of partonic jet flavour is not theoretically sound - however, it has been shown that this definition is reasonable equivalent to a matrix element-based labeling and the approach is deemed reasonable for the sake of performance studies. An alternative definition of jet flavour is given in [109].

The estimate of the flavour related JES uncertainty according to formula 9.1 involves the evaluation of the fraction of gluon initiated jets and its uncertainty in the analysis sample. The light quark and gluon initiated jet responses as well as the uncertainty on the gluon

---

[3]The size of the matching cone is motivated by the distance parameter R=0.4 used for the jet reconstruction algorithm.
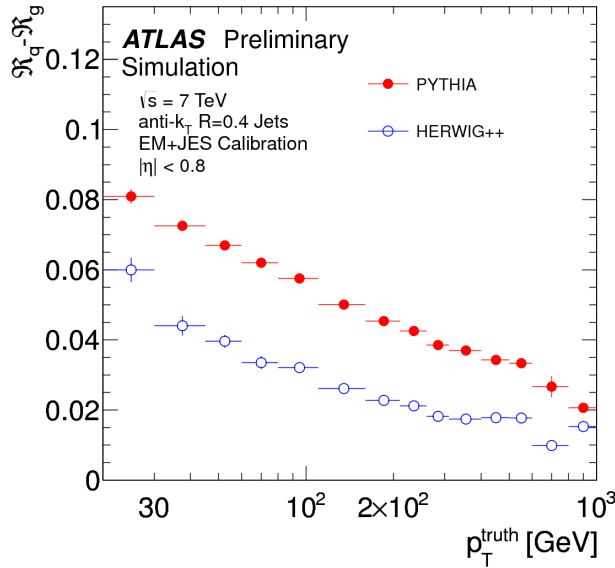
Figure 9.2.: Jet response difference between jets initiated by light quarks and gluons as a function of the jet p_T for Monte-Carlo simulations based on Pythia and on Herwig++ using jets in the central region $|\eta| < 0.8$.

initiated jet response are provided centrally, where the reference values $\mathcal{R}_q$ and $\mathcal{R}_g$ are based on the nominal Pythia dijets sample. Basic studies comparing the light quark and gluon initiated jet responses in the Pyhtia dijets simulation sample with those in various $t\bar{t}$ samples are summarised in appendix A. In overall, good agreement is found for the response of light quark and gluon initiated jets in the nominal (fully hadronic) $t\bar{t}$ sample generated with PowHeg and Pythia and the Pythia dijets sample. Differences arise in the $|\eta| > 2.8$ bins due to the usage of fast simulation in the forward detector for the $t\bar{t}$ sample. Given that these jets are not considered in the analysis using the Pythia dijets responses as reference results in a reasonable prescription.

9.3. Fraction of gluon initiated jets and its uncertainty in fully hadronic $t\bar{t}$ events

The fraction of gluon initiated jets as a function of particle jet p_T and jet η is extracted using the above flavour-labelling scheme. A more sophisticated approach using different properties of both jet flavours - such as the number of tracks associated with jets - allowing for a direct data to Monte-Carlo simulation comparison is described in [107].

The fraction of gluon initiated jets - i.e. the fraction of gluon initiated jets with respect to the subsample of gluon and light quark initiated jets - is shown in Figure 9.3, evaluated using the nominal fully hadronic PowHeg+Pythia Monte-Carlo simulation sample where

all analysis selection criteria have been applied. The fraction of gluon initiated jets keeps falling till it reaches its minimum p_T around 100 GeV and then keeps slightly rising again. This behaviour is mainly driven by the p_T spectrum of jets initiated by light quarks from the W decay, which, after reaching its peak value is falling more steeply compared to the spectrum of gluon initiated jets in the corresponding p_T region.

To further investigate the observed gluon jet fraction in the analysis sample the p_T spectra of light quark and gluon labelled jets in fully hadronic $t\bar{t}$ events are shown for the nominal PowHeg+Pythia simulation sample including all analysis cuts in fig 9.4. The p_T spectrum of light quark jets shows a steeply rising and falling edge around the peak value at ≈ 70 GeV. The p_T spectrum of gluon initiated jets shows a double peak structure where the falling edge after the second peak at ≈ 70 GeV is slightly flatter compared to the light quark jet falling edge. It should be noted that the p_T spectra are strongly influenced by the cuts applied, mainly by the p_T cuts on the 1st-5th leading (> 55 GeV) and 6th leading (> 30 GeV) jet. For comparison, the same distributions are shown with no analysis specific cuts applied in fig 9.5. The peak in the light quark jets spectrum is shifted to lower values at ≈ 40 GeV. For gluon jets the double peak structure disappears when dropping the analysis specific cuts, where the only peak is now at ≈ 30 GeV. The light quark initiated jet peak around ≈ 40 GeV is compatible with the dijet system p_T spectrum stemming from the W decay. Due to the tight jet p_T cuts the peak is shifted towards higher values in the analysis sample.

To obtain an estimate on the gluon fraction uncertainty the fraction of gluon initiated jets observed in different Monte-Carlo simulation samples is compared. To study the influence of the choice of the Monte-Carlo generator, the gluon fraction extracted in fully hadronic $t\bar{t}$ events generated with PowHeg+Herwig is compared with MC@NLO+Herwig. Similarly, the parton shower Monte-Carlo driven uncertainty is based on the gluon fraction comparison evaluated using PowHeg+Pythia and PowHeg+Herwig. Finally, ISR and FSR processes can influence the fraction of gluon initiated jets. To account for ISR/FSR effects the gluon fractions in AcerMC samples generated with varied parameters sensitive to the ISR/FSR strength (denoted as less/more PS) are compared. To obtain the final uncertainty on the fraction of gluon initiated jets the generator, parton-shower and ISR/FSR based uncertainties are added in quadrature. The fraction of gluon initiated jets extracted in all samples under study as a function of particle jet p_T is illustrated in Figure 9.6- 9.8 for different pseudorapidity bins. The gluon fraction distributions show similar shapes, with differences in the absolute gluon fraction Δf being smaller than 0.05 in most p_T bins for jets with $30\,\text{GeV} < p_T < 200\,\text{GeV}$.
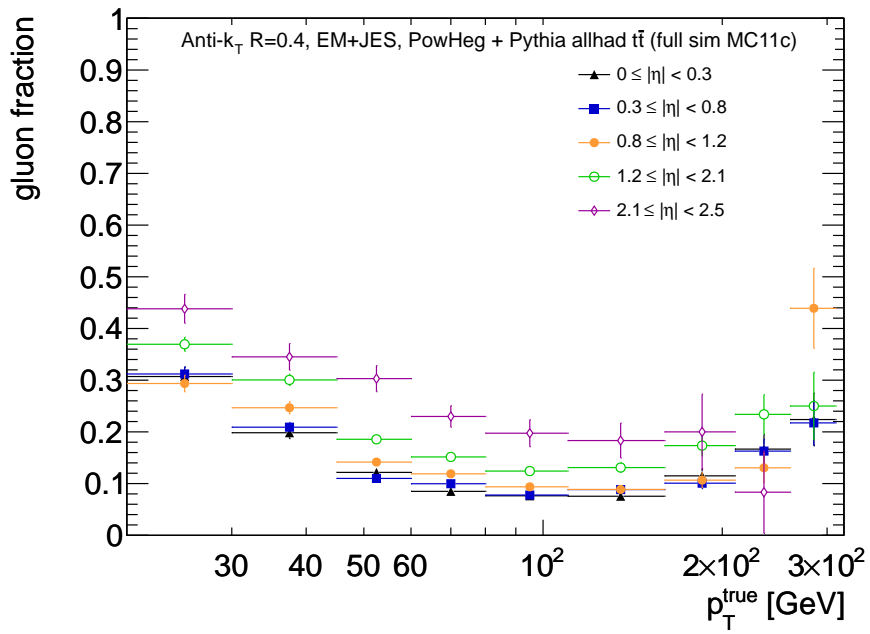
Figure 9.3.: Fraction of gluon initiated jets with respect to the jet subsample comprising gluon and light quark initiated jets in signal events simulated with PowHeg and Pythia after applying all selection criteria used in the top quark mass analysis in different pseudorapidity bins. The fraction of gluon initiated jets shows a flat minimum. This behaviour can be explained by the p_T spectrum of light quark jets stemming from the hadronic W boson decays, which is expected to have its peak in the p_T region around 50 GeV. The p_T spectrum of gluon initiated jets, however, is expected to mainly fall with raising jet transverse momentum while slightly flattening at higher p_T.
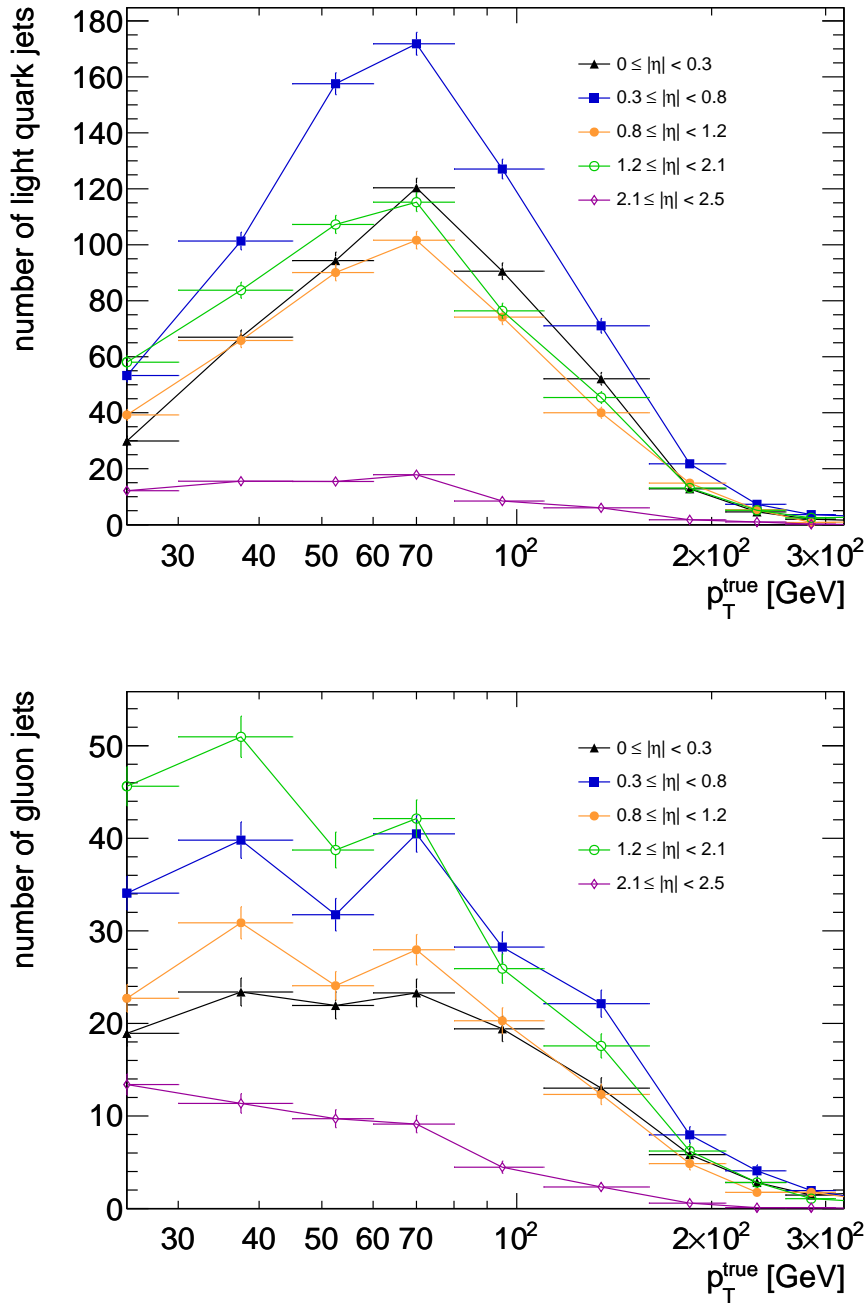
Figure 9.4.: p_T distributions of light quark (upper panel) and gluon (lower panel) initiated jets in $t\bar{t}$ events simulated with PowHeg and Pythia (including fully hadronic $t\bar{t}$ events only) after applying all selection criteria used for the top quark mass measurement. The results are shown in different bins of jet pseudorapidity η.
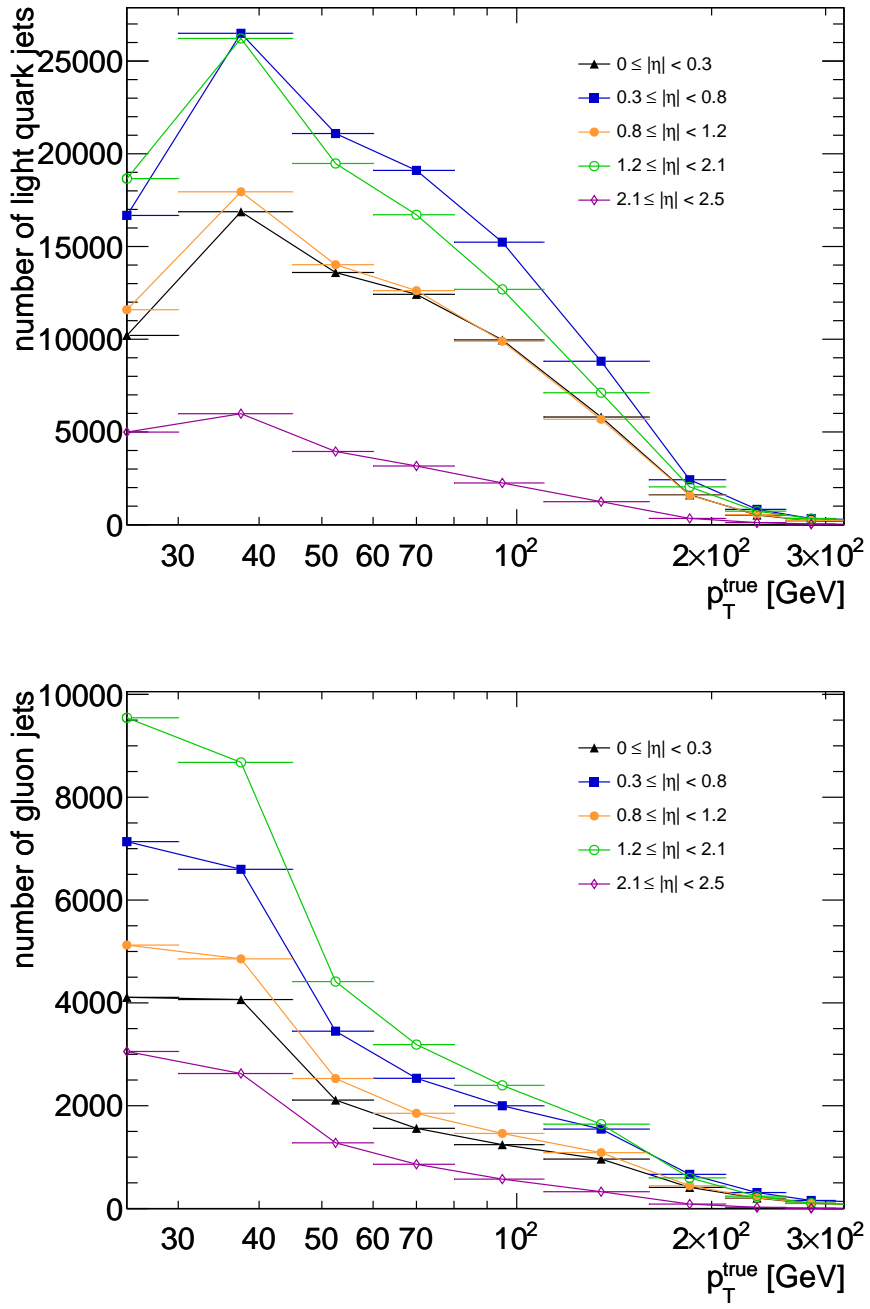
Figure 9.5.: p_T distributions of light quark (top) and gluon (bottom) initiated jets in $t\bar{t}$ events simulated with PowHeg and Pythia (including fully hadronic $t\bar{t}$ events only) with no analysis specific selection criteria applied. The results are shown in different bins of jet pseudorapidity η.
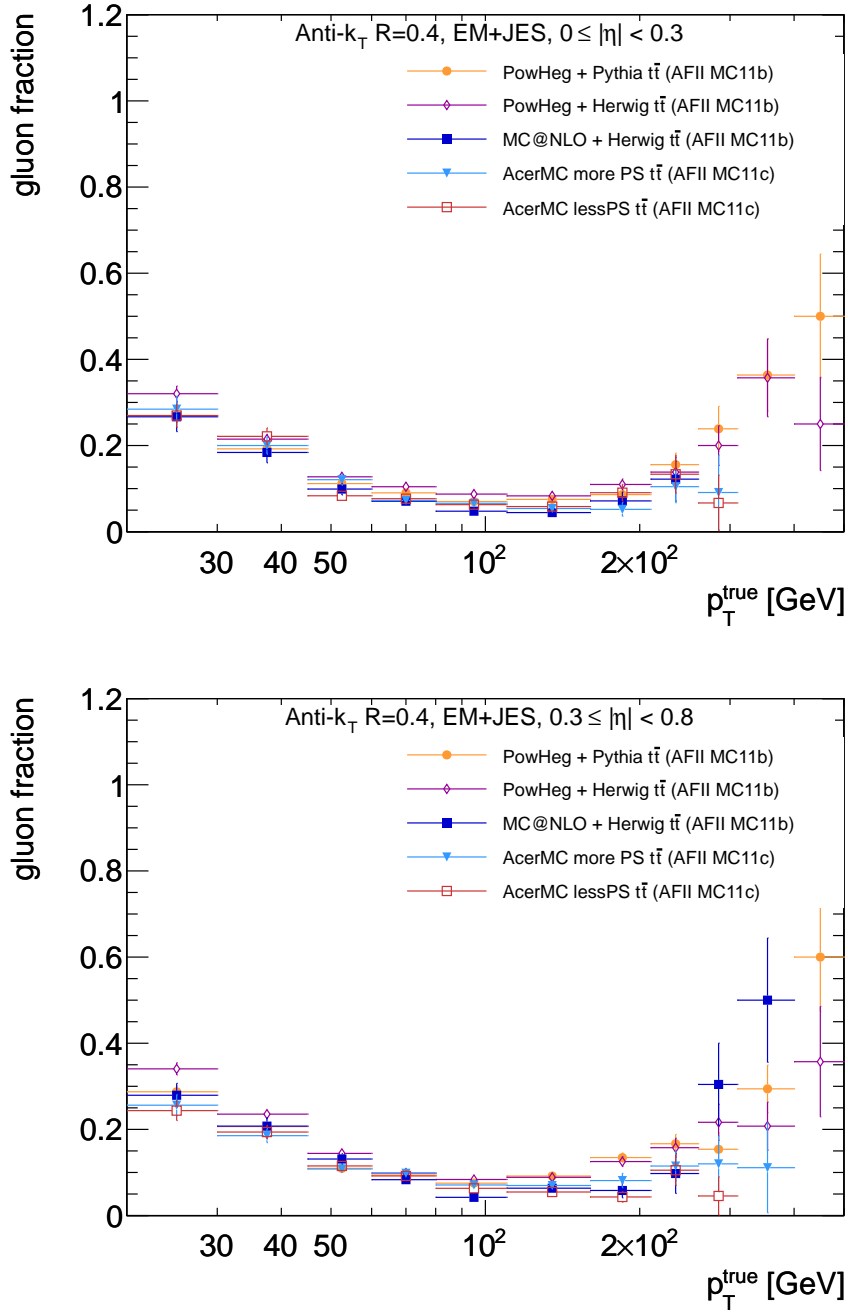
Figure 9.6.: Fraction of gluon initiated jets in different simulated $t\bar{t}$ samples (including fully hadronic $t\bar{t}$ events only) as a function of particle jet p_T with all analysis selection criteria applied for jets with $0 \leq |\eta| < 0.3$ (upper panel) and $0.3 \leq |\eta| < 0.8$ (lower panel).
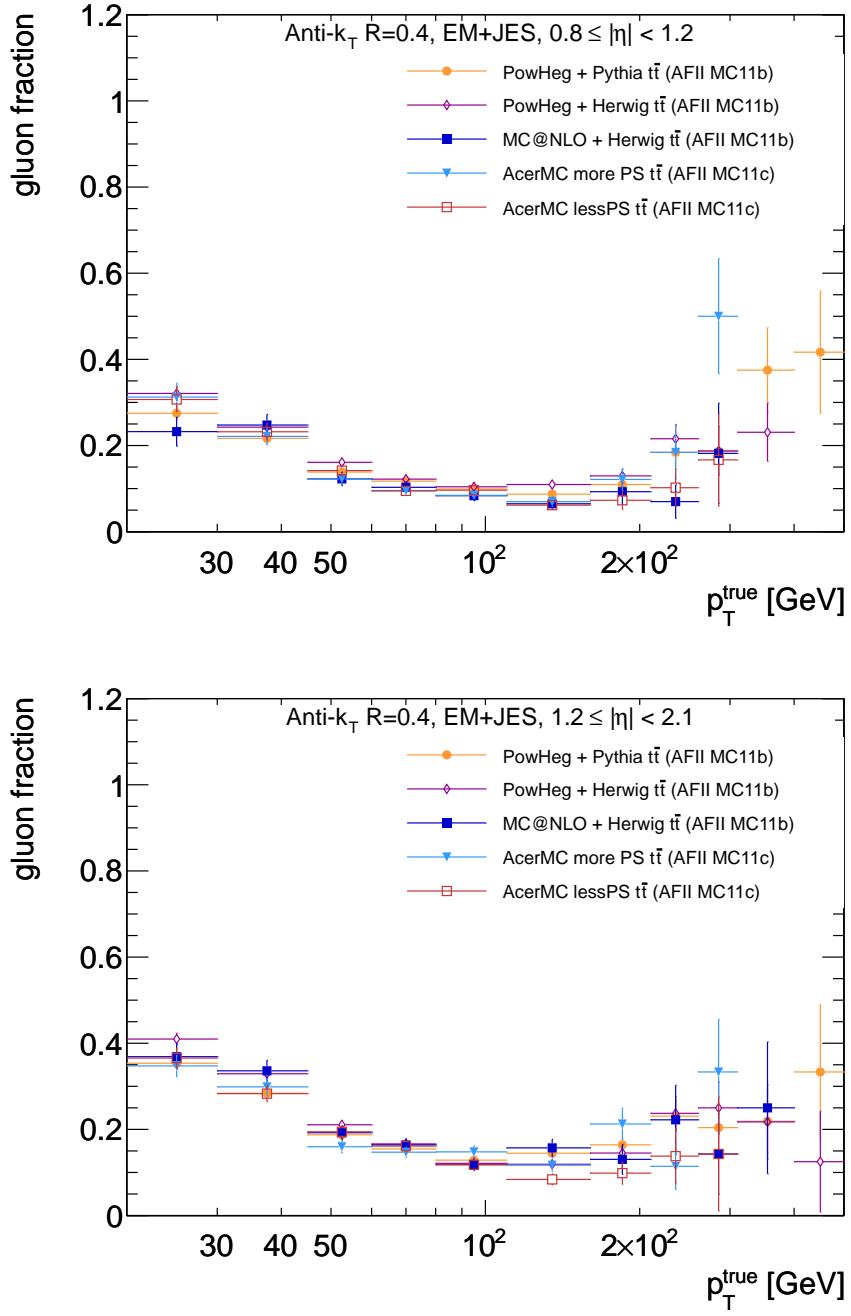
Figure 9.7.: Fraction of gluon initiated jets in different simulated $t\bar{t}$ samples (including fully hadronic $t\bar{t}$ events only) as a function of particle jet p_T with all analysis selection criteria applied for jets with $0.8 \leq |\eta| < 1.2$ (upper panel) and $1.2 \leq |\eta| < 2.1$ (lower panel).
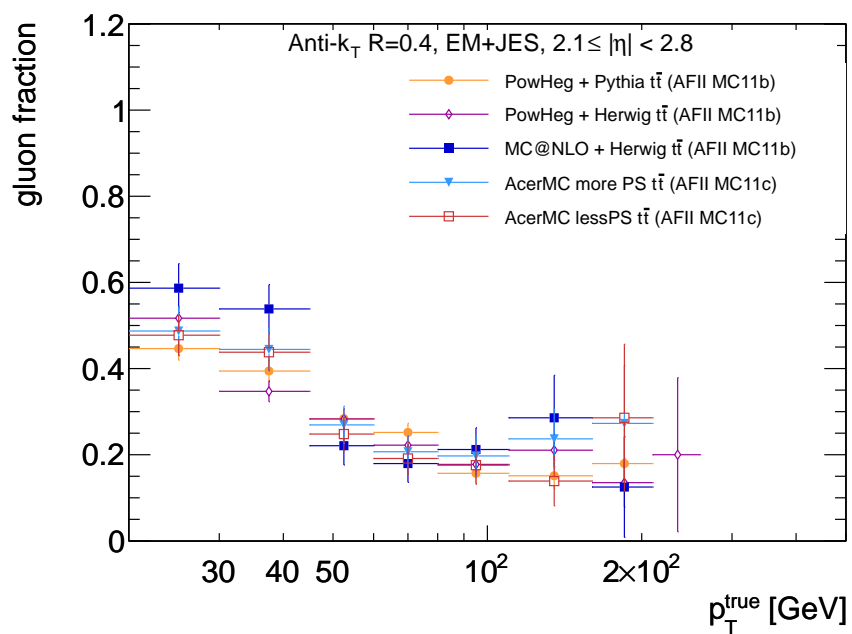
Figure 9.8.: Fraction of gluon initiated jets in different simulated $t\bar{t}$ samples (including fully hadronic $t\bar{t}$ events only) as a function of particle jet p_T with all analysis selection criteria applied for jets with $2.1 \leq |\eta| < 2.5$.

10. Measurement Results

The top quark mass measurement is performed using data from proton-proton collisions at a centre-of-mass energy of $\sqrt{s} = 7$ TeV, corresponding to an integrated luminosity of 4.7 fb^{-1}. All object definition and event selection criteria outlined in Chapter 4 are applied. A binned likelihood fit is applied to the $R_{3/2}$ distribution in data according to formula 7.6. The result of the binned likelihood fit is shown in Figure 10.2(a). Besides the overall probability density function (black), the separate signal (red) and background (green) p.d.f.s are also illustrated.

The background fraction extracted from the likelihood fit to the data yields 75.9 $\pm$ 0.2%, which is 0.7% higher compared to the fraction of background events evaluated via the ABCD method[1]. However, as shown in Section 7.5.2, the expected bias on the background fraction introduced by the template method yields + 0.9%, in agreement with the measured background fraction which is slightly higher compared to the expectation. The top quark mass is not influenced by this bias as has been shown by means of pseudo-experiments in Section 7.5.2. The 2-dimensional probability density function of the fitted top quark mass and the background fraction is highlighted in Figure 10.2(c).

The top quark mass in data is measured to be 175.09 GeV. To estimate the statistical uncertainty the probability density function is projected onto the top quark mass axis, see Figure 10.2(b). The uncertainty is given by the standard deviation boundaries around the mean value, where the latter corresponds to the measured top quark mass. The statistical uncertainty is nearly identical for both the up and down variation and yields $^{+1.43}_{-1.42}$ GeV. This value agrees within one standard deviation with the expected statistical uncertainty of 1.38$\pm$0.06 GeV (see Figure 10.1), obtained when performing 5000 pseudo-experiments according to the procedure outlined in Section 7.5.1. For consistency with the top quark mass measured in data, Monte-Carlo events generated with a top quark mass of m_{top} = 175 GeV were used to create pseudodata.

The various sources of systematic uncertainties under study are summarised in Table 10.1, which sum up to an uncertainty of 1.83 GeV. Although the sensitivity to the jet energy scale is limited due to the usage of the $R_{3/2}$ variable the major contribution to the overall systematic uncertainty still comes from the jet energy scale, followed by the relative *b*-JES and generator modelling uncertainties. It should be noted that even though the statistical uncertainty exceeds the measured systematic deviation in some of the Monte-Carlo samples under study, the corresponding deviations were kept and were

---

[1]It should be noted that the background fraction is lower as quoted in Section 5.2.3 due to the restricted $R_{3/2}$ range.
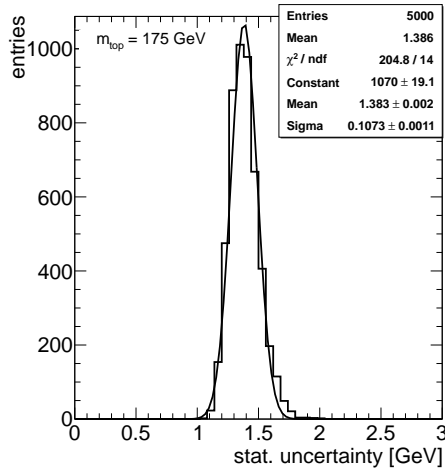
Figure 10.1.: Expected statistical uncertainty - evaluated by means of pseudo experiments using Monte-Carlo events simulated with m_{top} = 175 GeV.

used to calculate the expected precision of the measurement.

The measured top quark mass, its statistical and systematic uncertainty as well as the background fraction and its statistical uncertainty are:

- m_{top}= 175.1 $\pm$ 1.4 (stat.) $\pm$ 1.8 (syst.) GeV/c^2

- f_{back}= 75.9 $\pm$ 0.2%.

which yields a total uncertainty of 2.32 GeV and is therefore as precise as the currently best published ATLAS result on the top quark mass [103], obtained in the lepton+jets decay channel of $t\bar{t}$ events, yielding 174.5 $\pm$ 2.38 GeV/c^2. The result is consistent with measurements of m_{top} in the fully hadronic $t\bar{t}$ decay channel performed by the CDF (172.5 $\pm$ 2.0 GeV/c^2) [110] and CMS (173.5 $\pm$ 1.48 GeV/c^2) [111] experiments.

(a)

(b)   (c)
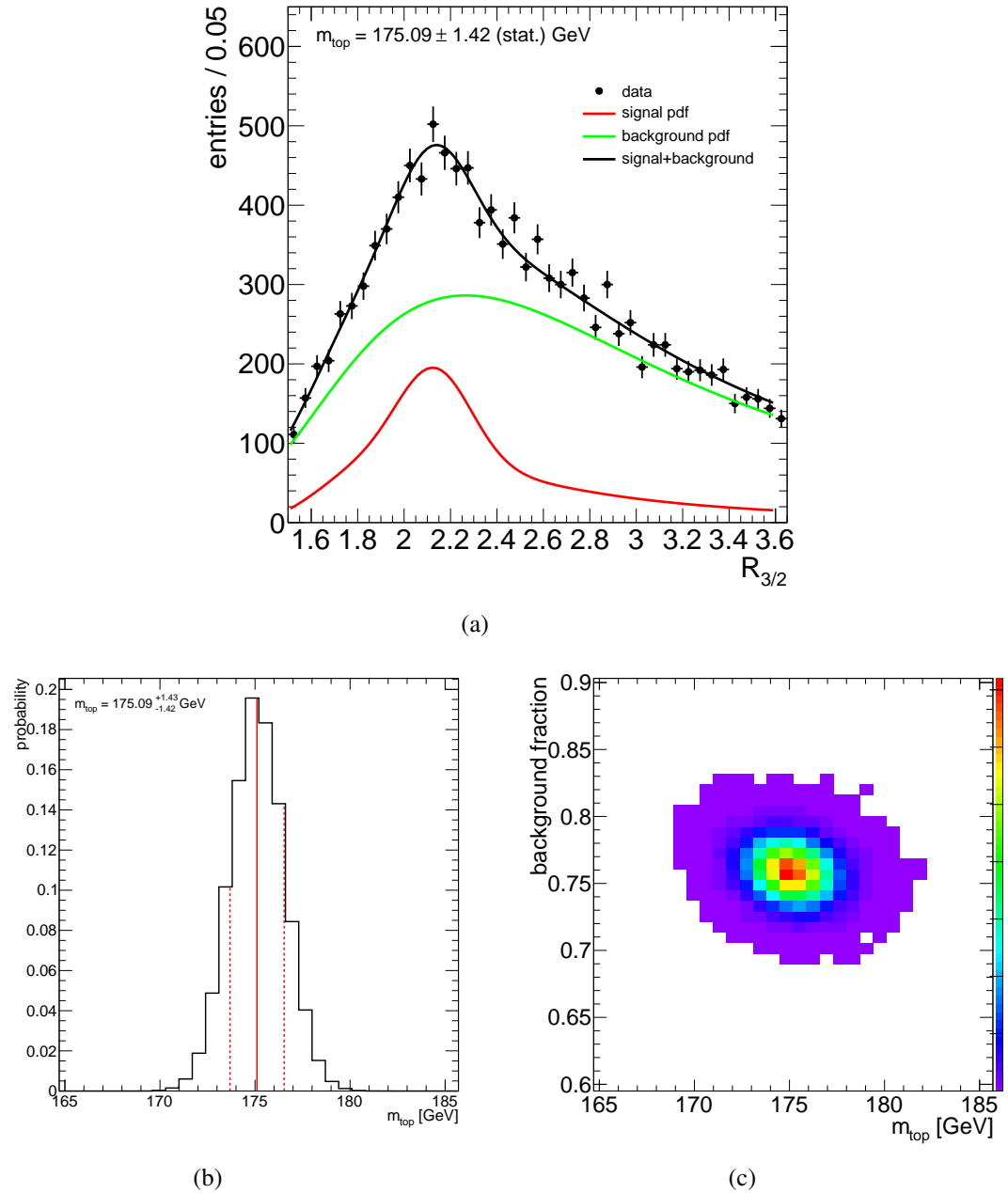
Figure 10.2.: Result of the binned likelihood fit to the full 2011 dataset recorded with the
ATLAS detector (L=4.7 fb^{-1}). Shown are the fit result for the signal (red)
and background (green) p.d.f.s as well as the signal+background combined
p.d.f. (black) yielding m$_{top}$= 175.09 ± 1.42 GeV and f$_{back}$= 75.9 ± 0.2% (a).
Also shown is the projection of the probability density function onto the top
quark mass axis. The statistical uncertainty of the measurement is estimated
by means of the ±1σ boundaries (red dashed line) around the mean value
(b). The 2-dimensional probability density function of the fitted top quark
mass and the background fraction is highlighted in (c).

Source	Uncertainty [GeV]
Method calibration	0.13
Full/fast simulation	0.19
Background modelling	0.45
MC generator	0.72 ($\pm$2.31)
Fragmentation model	0.33 ($\pm$0.31)
Colour reconnection	0.13
Underlying event	0.22
ISR/FSR	0.17 ($\pm$0.58)
Proton PDF	0.3
Pile-up	0.1
Jet energy scale	1.28
b-jet energy scale	0.75
b-tagging efficiency / mistag rate	0.19
Jet vertex fraction	0.01
Jet energy resolution	0.03
Jet reconstruction efficiency	0.01
Sum	1.83

Table 10.1.: Overview over the sources of systematic uncertainties considered together with the resulting uncertainties. The numbers in brackets represent the estimated statistical uncertainty for sources of systematic uncertainties which are evaluated using two independent samples of simulated events.

11. Conclusion

A top quark mass measurement has been performed in the fully hadronic $t\bar{t}$ decay channel using data collected with the ATLAS detector from proton-proton collision at a centre of mass energy of $\sqrt{s}$ =7 TeV. The dataset has been recorded in 2011 and corresponds to an integrated luminosity of 4.7 fb^{-1}. A template method has been applied to measure the top quark mass in data based on the $R_{3/2}$ variable which is built from the invariant mass ratio of the hadronically decaying top quark and the W-boson. The choice of the $R_{3/2}$ estimator is motivated by its reduced sensitivity to the jet energy scale, which is one of the major sources of systematic uncertainty in the top quark measurement.

To discriminate fully hadronic $t\bar{t}$ events from background events arising from QCD multijet production, a pure 'cut-based' event selection has been applied, resulting in a background fraction of $\approx$75%. Particular focus has been set on the modelling of background events via a data driven ABCD method. Detailed studies have been performed allowing to find a set of observables with minimal correlation to be used in the ABCD method. Good agreement between data and background model has been found for nearly all kinematical distributions. The background normalisation extracted via the ABCD method has been used to test the background fraction resulting from the binned likelihood fit to data, where both results have been shown to be consistent with each other.

The measured top quark mass together with its statistical und systematic uncertainties has been evaluated to be:

$$m_{top}= 175.1 \pm 1.4 \text{ (stat.)} \pm 1.8 \text{ (syst.) GeV/c}^2$$

Even though the uncertainty on the jet energy scale could be limited thanks to the use of the $R_{3/2}$ variable it still represents the largest contribution to the overall systematic uncertainty, followed by the residual b-jet energy scale and the choice of the signal Monte-Carlo generator. Due to the precise modelling via the ABCD method, the uncertainty on the background shapes only amounts to 0.45 GeV despite of the large contribution of multijet events in the analysis sample.

Further reduction of the (b-)jet energy scale uncertainty may be achieved by using a 2-dimensional or 3-dimensional template technique, where the latter has only recently been applied in the lepton+jets channel in ATLAS [112]. These techniques typically rely on additional variables sensitive to the 'light' and b-jet-to-parton scale factors, such as the W-boson invariant mass distribution, to measure the top quark mass and the (b)-jet scale

factor simultaneously. However, the usage of a 3 dimensional template technique requires sufficiently large statistics. Using the full 2011 dataset the fully hadronic $t\bar{t}$ signal statistics is largely decreased after applying the event selection criteria to reject the large multijet background contribution. The dataset recorded in 2012, however, corresponding to a 4-fold integrated luminosity of 20 fb^{-1}, might allow applying a 3 dimensional fit technique in the fully hadronic $t\bar{t}$ channel. This, together with the steadily growing understanding of the detector and improved Monte-Carlo modelling techniques provides room to further improve on the precision achieved for the top quark mass measurement in the fully hadronic $t\bar{t}$ channel.

A. Flavour response in $t\bar{t}$ events

The response of gluon and light quark labelled jets in simulated $t\bar{t}$ events has been studied and compared for different choices of the Monte-Carlo generator. The jet flavour labelling as well as the calorimeter to particle jet matching has been performed as outlined in Section 9.2. To obtain the jet response, a Gaussian function is fit to the p_T^{reco}/p_T^{true} distributions in different bins of $|\eta|$ and particle jet p_T, where p_T^{reco} denotes the transverse momentum of the calorimeter jet and p_T^{true} is the transverse momentum of the particle jet matched to the calorimeter jet. The mean of the fitted Gauss function is quoted as jet response. Only isolated calorimeter jets are considered in this study, where a jet is considered as isolated if no further reconstructed jet with EM-scale (uncalibrated) $p_T > 7$ GeV is found within a cone of size 1.0 around the jet of interest.

The study is focused on non-allhadronic $t\bar{t}$ samples, mainly for practical reasons, since full simulation samples are available for a broader range of generators and parton shower Monte-Carlo programs and samples are available at larger statisitics. For comparison, the jet response was also extracted for the nominal fully hadronic PowHeg+Pythia $t\bar{t}$ sample. As a reference, the corresponding response in the Pythia dijets Monte-Carlo sample is also shown. To allow for a comparison between the fully and non-allhadronic $t\bar{t}$ as well as with the dijet event topology, no analysis specific event-level criteria were applied. The object definition including overlap removal was performed according to Chapter 4.

A.1. Light quark jet response in $t\bar{t}$ events

Consistent results are found for the response of light quark labelled jets in events simulated with all different Monte-Carlo programs under study (Figures A.1-A.7) for jets with $|\eta| < 2.8$, where samples using Pythia to perform parton showering show a slight trend towards higher jet responses. Differences between the dijet sample with respect to the $t\bar{t}$ samples arise for jets with $|\eta| > 2.8$. However, this effect can be understood as a result of different settings used in the detector simulation, where the $t\bar{t}$ samples under study were simulated using a simplified fast simulation for the forward calorimeter. In addition, differences between the MC@NLO+Herwig sample with respect to all $t\bar{t}$ samples under study get visible for jets with $|\eta| > 2.8$, where the MC@NLO+Herwig sample predicts lower jet responses.

Also shown is a comparison of ATLAS fast simulation (AFII) MC11b samples for MC@NLO+Herwig, PowHeg+Pythia and PowHeg+Herwig (Figures A.8-A.14). Again, using Pythia as parton shower Monte-Carlo results in a slightly higher jet response, specif-

ically for jets < 100 GeV in the central region $|\eta| < 0.8$. A better agreement between the MC@NLO and both PowHeg samples is found for jets with $|\eta| > 2.8$ compared to the corresponding full simulation samples.
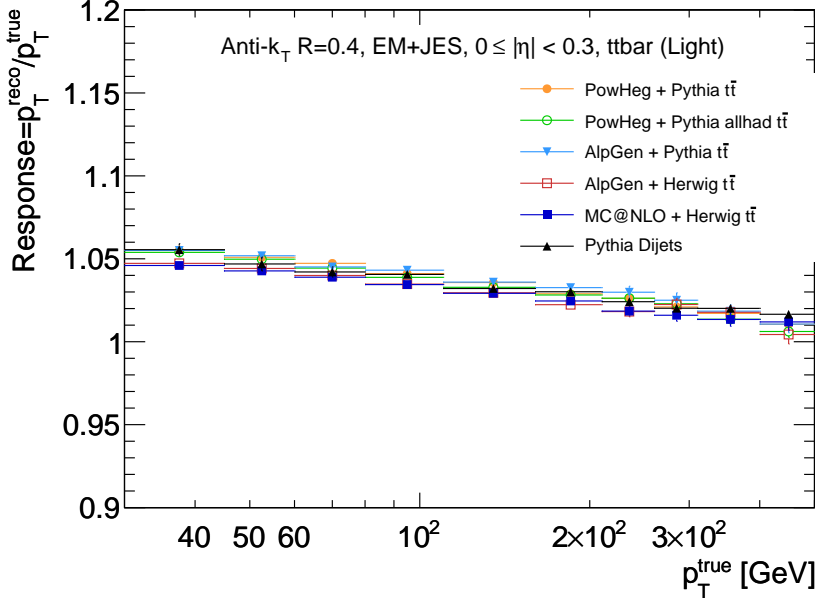
Figure A.1.: Jet response of light quark labelled jets in *tt̄* events for different choices of the Monte-Carlo generator and parton shower program for jets with $0 \leq |\eta| < 0.3$. The comparison only includes full simulation samples.
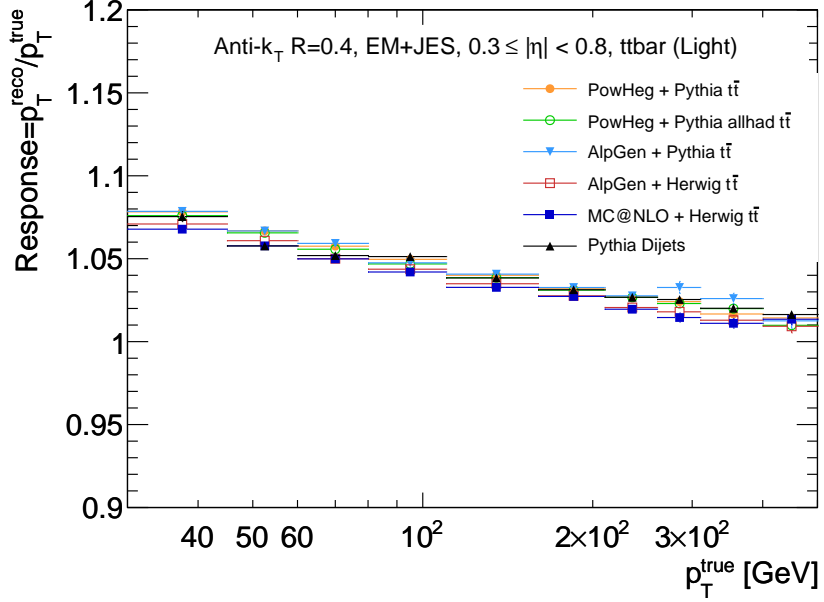
Figure A.2.: Jet response of light quark labelled jets in $t\bar{t}$ events for different choices of the Monte-Carlo generator and parton shower program for jets with $0.3 \leq |\eta| < 0.8$. The comparison only includes full simulation samples.
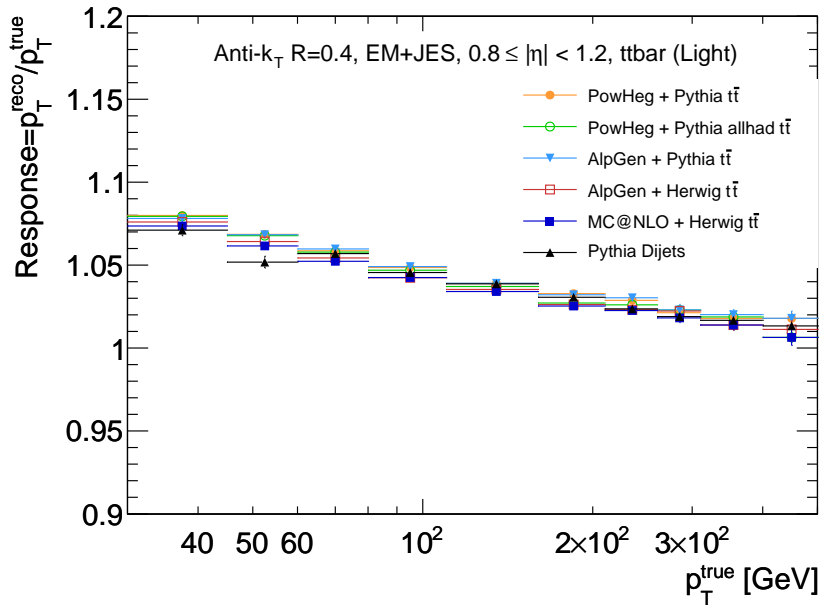
Figure A.3.: Jet response of light quark labelled jets in $t\bar{t}$ events for different choices of the Monte-Carlo generator and parton shower program for jets with $0.8 \leq |\eta| < 1.2$. The comparison only includes full simulation samples.
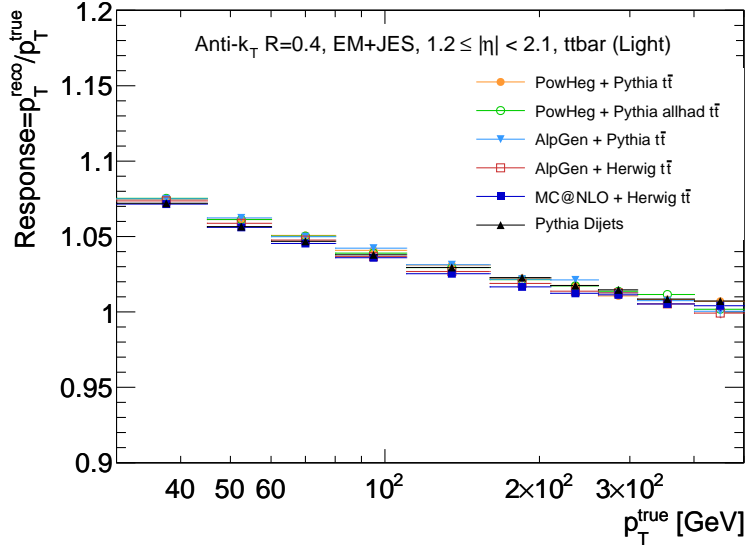
Figure A.4.: Jet response of light quark labelled jets in *t t̄* events for different choices of the Monte-Carlo generator and parton shower program for jets with $1.2 \leq |\eta| < 2.1$. The comparison only includes full simulation samples.
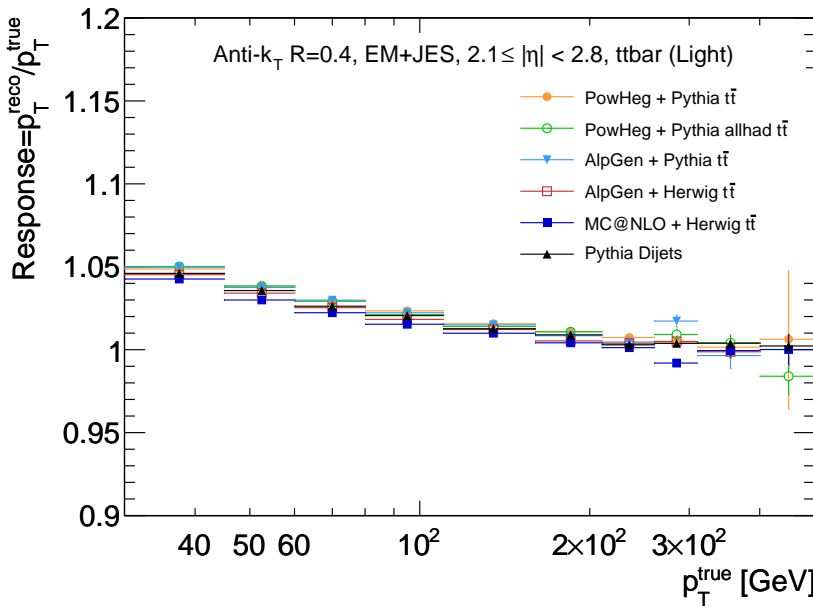
Figure A.5.: Jet response of light quark labelled jets in *t t̄* events for different choices of the Monte-Carlo generator and parton shower program for jets with $2.1 \leq |\eta| < 2.8$. The comparison only includes full simulation samples.
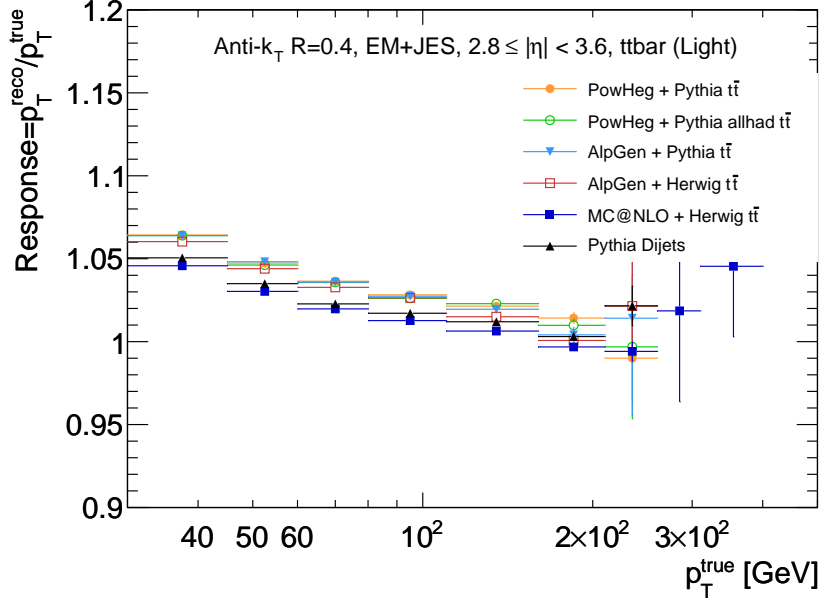
Figure A.6.: Jet response of light quark labelled jets in $t\bar{t}$ events for different choices of the Monte-Carlo generator and parton shower program for jets with $2.8 \leq |\eta| < 3.6$. The comparison only includes full simulation samples.
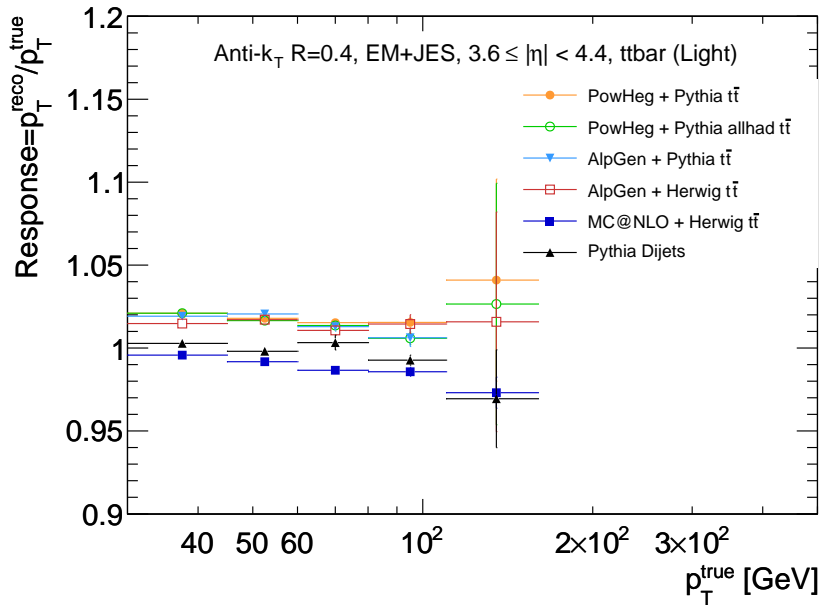
Figure A.7.: Jet response of light quark labelled jets in $t\bar{t}$ events for different choices of the Monte-Carlo generator and parton shower program for jets with $3.6 \leq |\eta| < 4.4$. The comparison only includes full simulation samples.
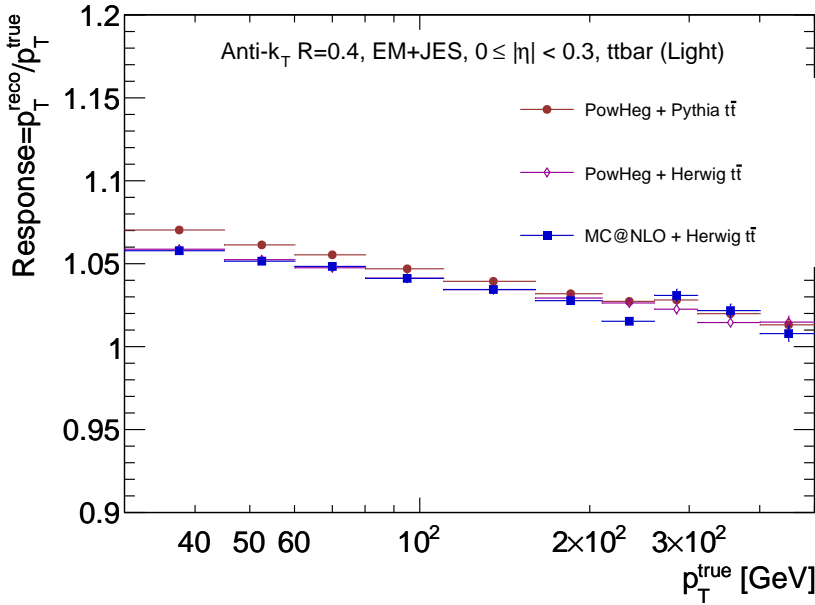
Figure A.8.: Jet response of light quark labelled jets in *tt̄* events for different choices of the Monte-Carlo generator and parton shower program for jets with $0 \leq |\eta| < 0.3$. The comparison only includes fast simulation samples.
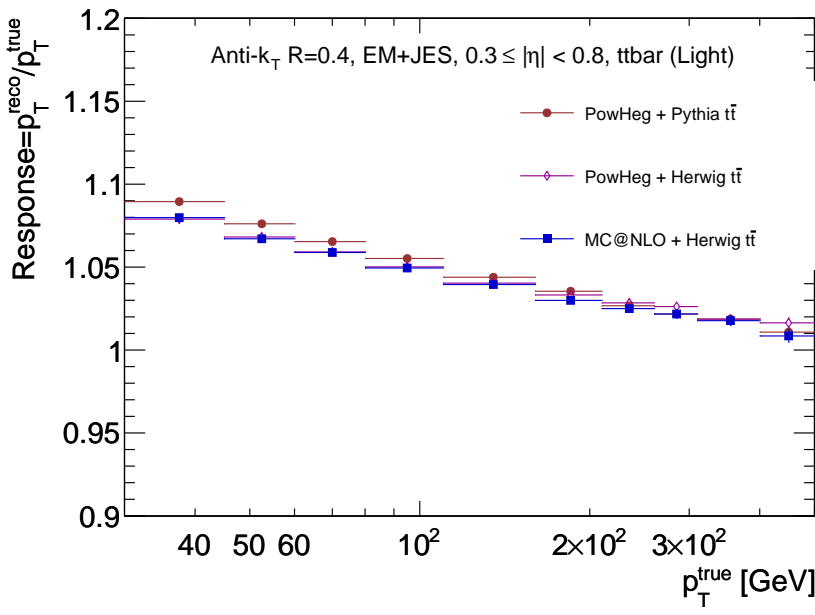
Figure A.9.: Jet response of light quark labelled jets in *tt̄* events for different choices of the Monte-Carlo generator and parton shower program for jets with $0.3 \leq |\eta| < 0.8$. The comparison only includes fast simulation samples.
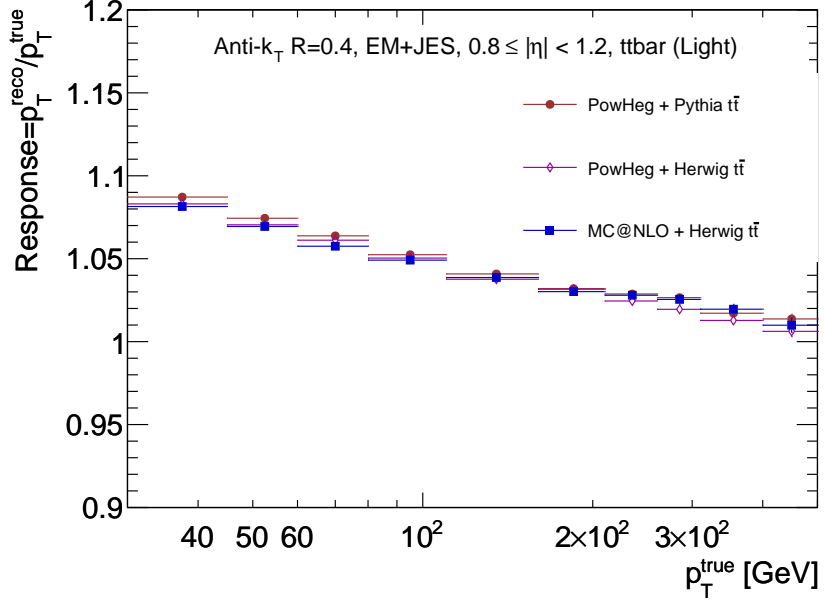
Figure A.10.: Jet response of light quark labelled jets in $t\bar{t}$ events for different choices of the Monte-Carlo generator and parton shower program for jets with $0.8 \leq |\eta| < 1.2$. The comparison only includes fast simulation samples.
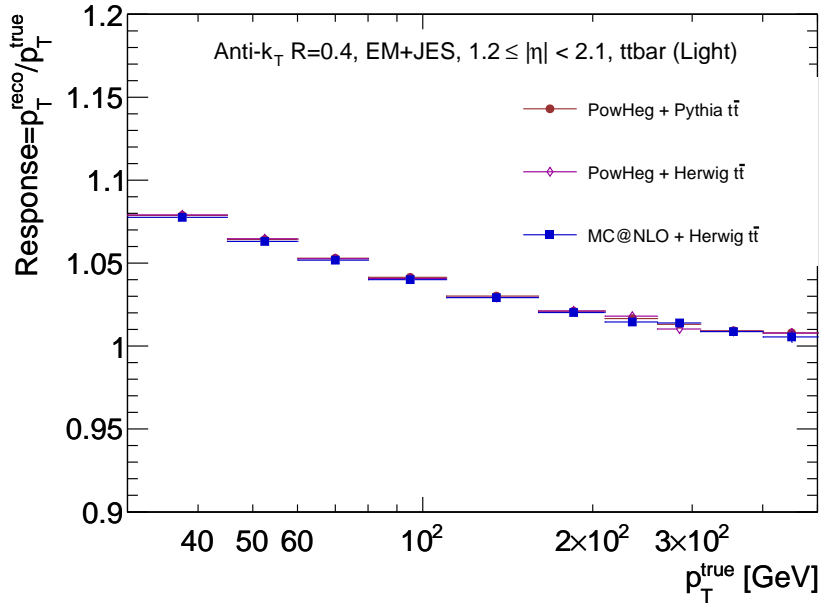
Figure A.11.: Jet response of light quark labelled jets in $t\bar{t}$ events for different choices of the Monte-Carlo generator and parton shower program for jets with $1.2 \leq |\eta| < 2.1$. The comparison only includes fast simulation samples.
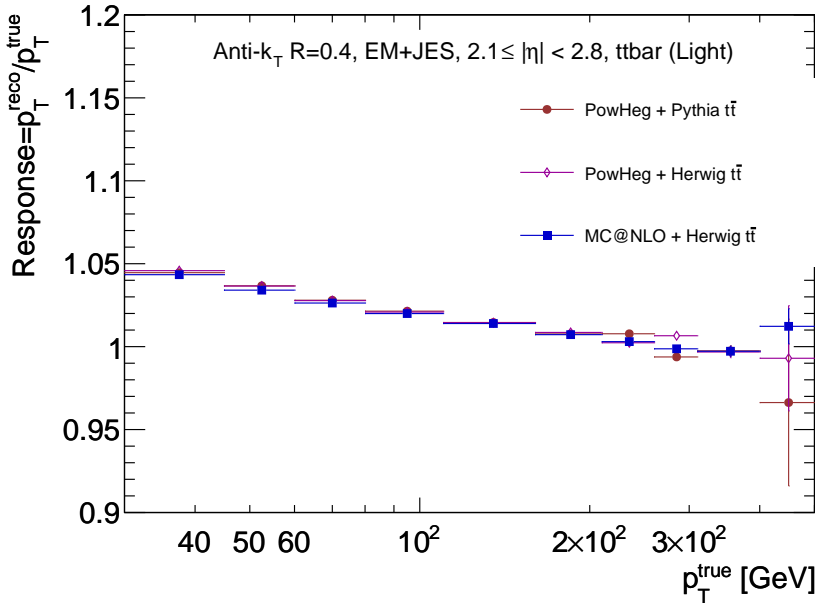
Figure A.12.: Jet response of light quark labelled jets in $t\bar{t}$ events for different choices of the Monte-Carlo generator and parton shower program for jets with $2.1 \leq |\eta| < 2.8$. The comparison only includes fast simulation samples.
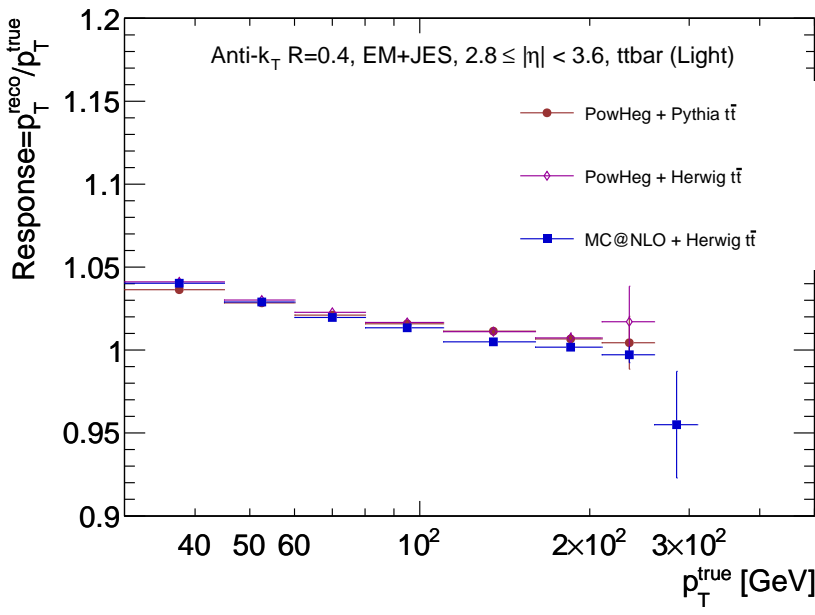
Figure A.13.: Jet response of light quark labelled jets in $t\bar{t}$ events for different choices of the Monte-Carlo generator and parton shower program for jets with $2.8 \leq |\eta| < 3.6$. The comparison only includes fast simulation samples.
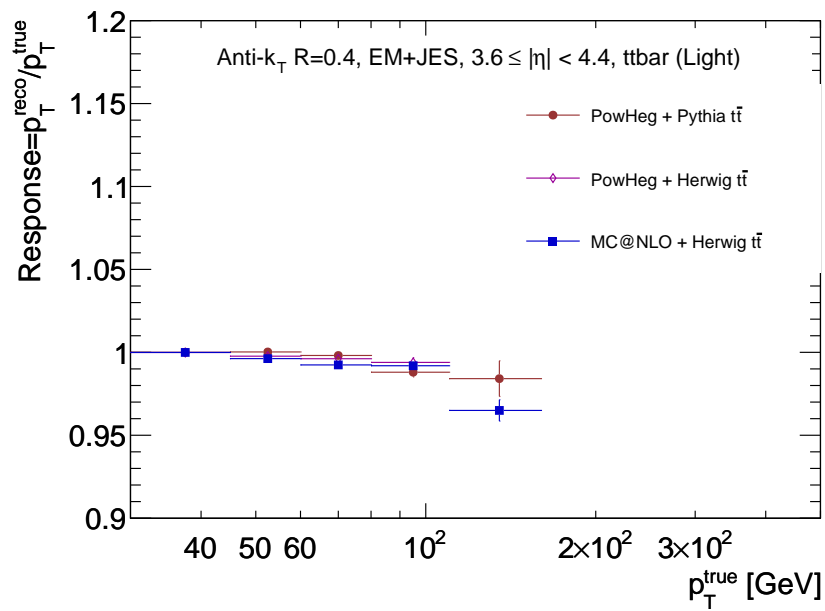
Figure A.14.: Jet response of light quark labelled jets in *tt̄* events for different choices of the Monte-Carlo generator and parton shower program for jets with 3.6 ≤ $|\eta|$ < 4.4. The comparison only includes fast simulation samples.

A.2. Gluon jet response in $t\bar{t}$ events

The response of gluon labelled jets in full simulation samples is illustrated in Figures A.15-A.21. For jets with $|\eta| < 2.8$ the samples using Herwig as parton shower Monte-Carlo predict a higher response. These differences get smaller for jets with $p_T > 100$ GeV for the samples generated with AlpGen+Herwig, but get more pronounced for MC@NLO+Herwig. In overall, good agreement is found for $t\bar{t}$ samples using Pythia as parton shower Monte-Carlo with the reference Pythia dijets sample - with differences in the forward calorimeter due to the usage of fast simulation for the $t\bar{t}$ samples.

The same trend gets visible in the comparison plots using ATLAS fast simulation (AFII) samples (Figures A.22-A.28), where the response of gluon labelled jets in the PowHeg+Herwig and MC@NLO+Herwig samples is higher with respect to PowHeg+Pythia. Again, these differences get smaller for jets with $p_T > 100$ GeV in both PowHeg samples, while the jet response in the MC@NLO sample is systematically higher with respect to both PowHeg samples.

Apart from the behaviour observed in the response of gluon labelled jets in MC@NLO, differences in the gluon jet response are mainly driven by differences in the simulation of parton shower and hadronisation effects.
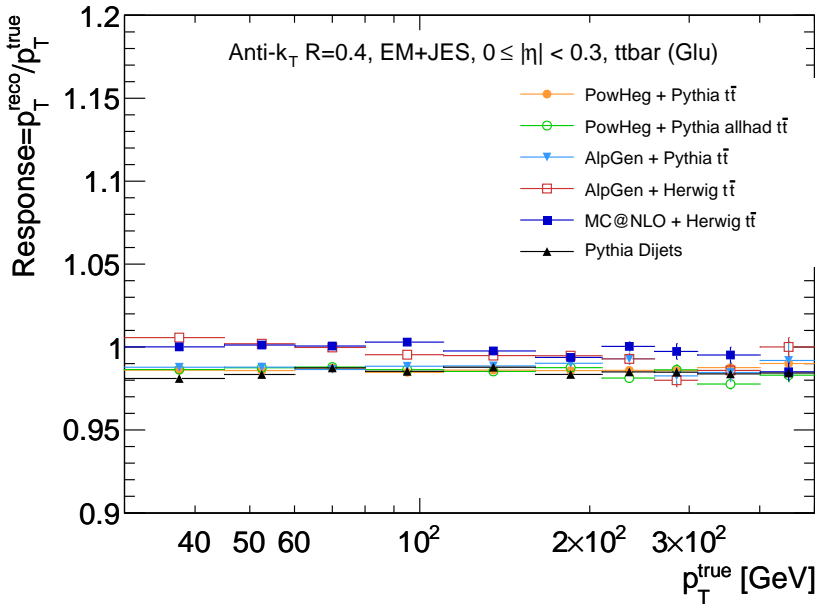
Figure A.15.: Jet response of gluon labelled jets in $t\bar{t}$ events for different choices of the Monte-Carlo generator and parton shower program for jets with $0 \leq |\eta| < 0.3$. The comparison only includes full simulation samples.
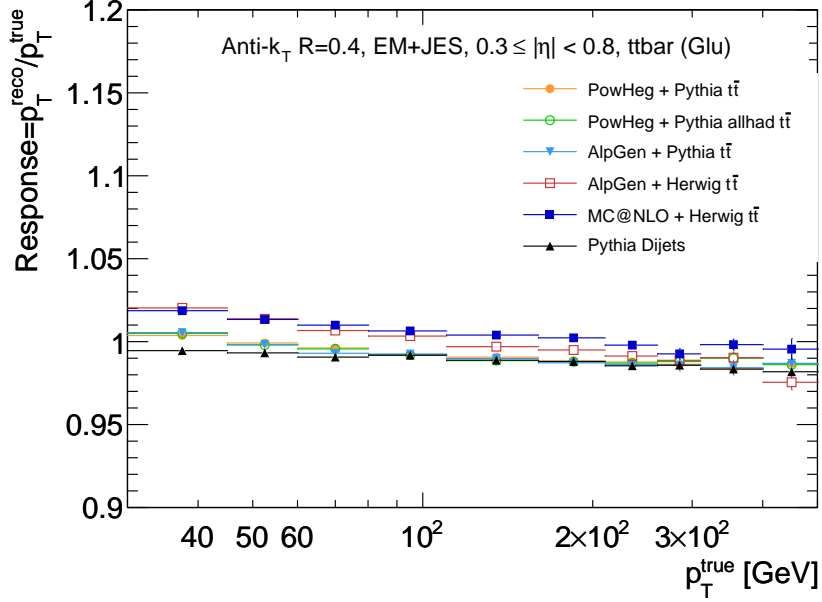
Figure A.16.: Jet response of gluon labelled jets in *tt̄* events for different choices of the Monte-Carlo generator and parton shower program for jets with $0.3 \leq |\eta| < 0.8$. The comparison only includes full simulation samples.
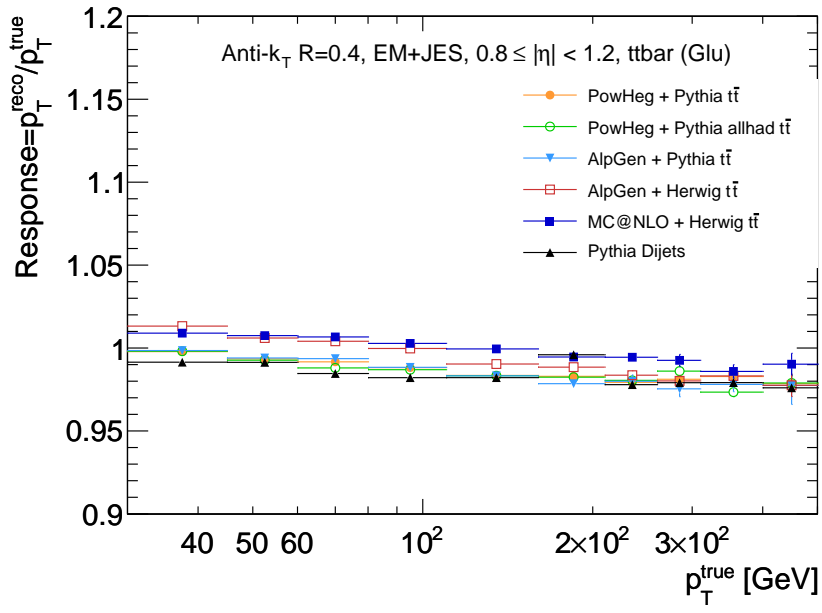
Figure A.17.: Jet response of gluon labelled jets in *tt̄* events for different choices of the Monte-Carlo generator and parton shower program for jets with $0.8 \leq |\eta| < 1.2$. The comparison only includes full simulation samples.
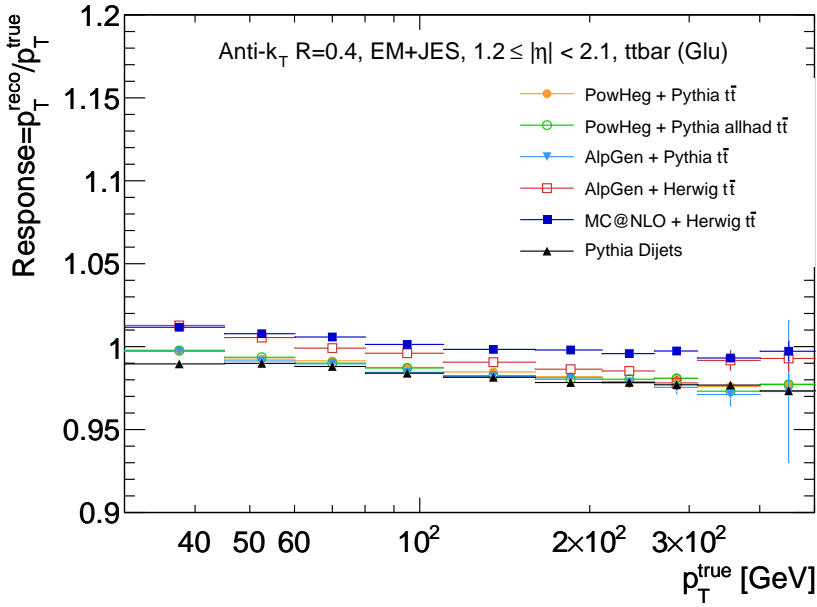
Figure A.18.: Jet response of gluon labelled jets in *tt̄* events for different choices of the Monte-Carlo generator and parton shower program for jets with $1.2 \leq |\eta| < 2.1$. The comparison only includes full simulation samples.
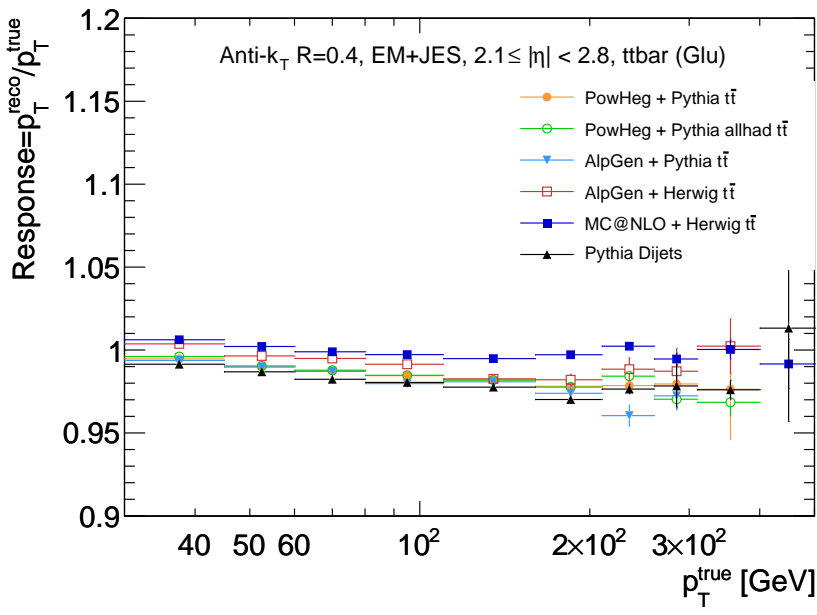
Figure A.19.: Jet response of gluon labelled jets in *tt̄* events for different choices of the Monte-Carlo generator and parton shower program for jets with $2.1 \leq |\eta| < 2.8$. The comparison only includes full simulation samples.
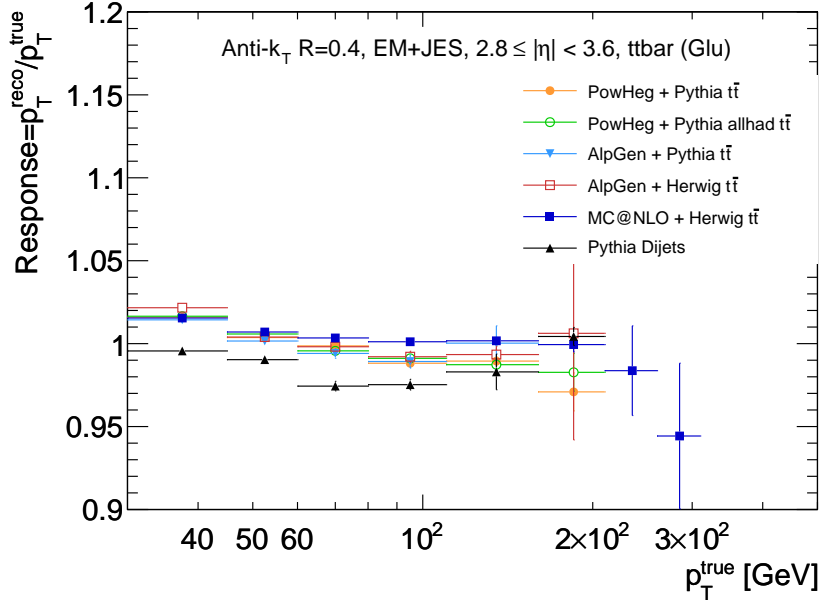
Figure A.20.: Jet response of gluon labelled jets in *tt̄* events for different choices of the Monte-Carlo generator and parton shower program for jets with $2.8 \leq |\eta| < 3.6$. The comparison only includes full simulation samples.
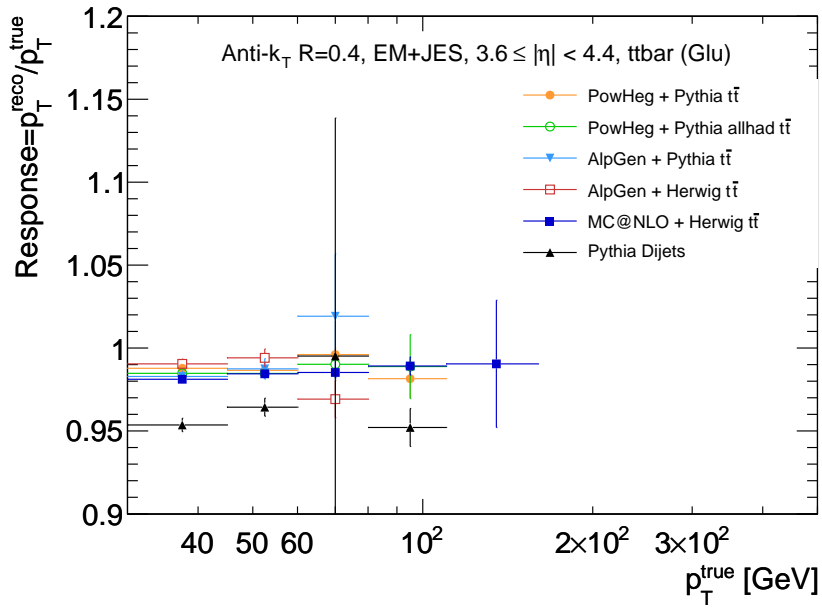
Figure A.21.: Jet response of gluon labelled jets in *tt̄* events for different choices of the Monte-Carlo generator and parton shower program for jets with $3.6 \leq |\eta| < 4.4$. The comparison only includes full simulation samples.
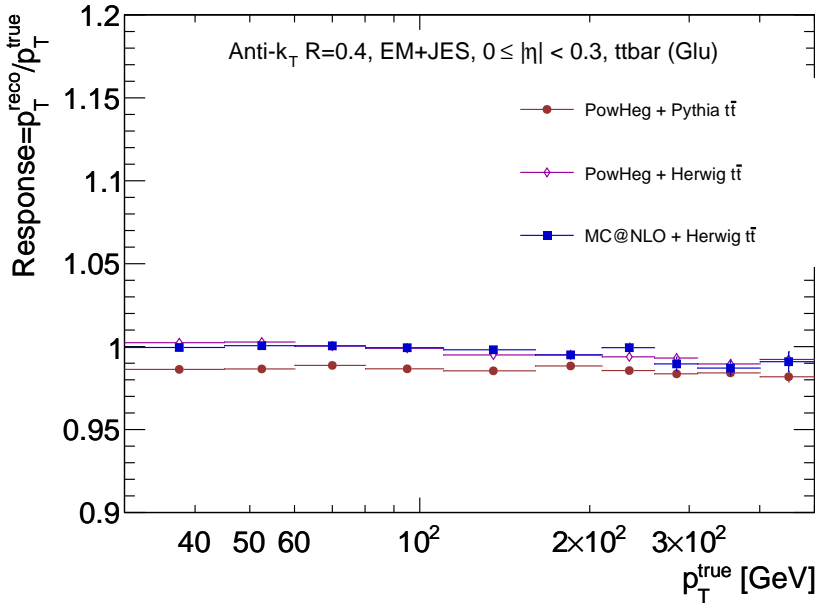
Figure A.22.: Jet response of gluon labelled jets in *tt̄* events for different choices of the Monte-Carlo generator and parton shower program for jets with $0 \leq |\eta| < 0.3$. The comparison only includes fast simulation samples.
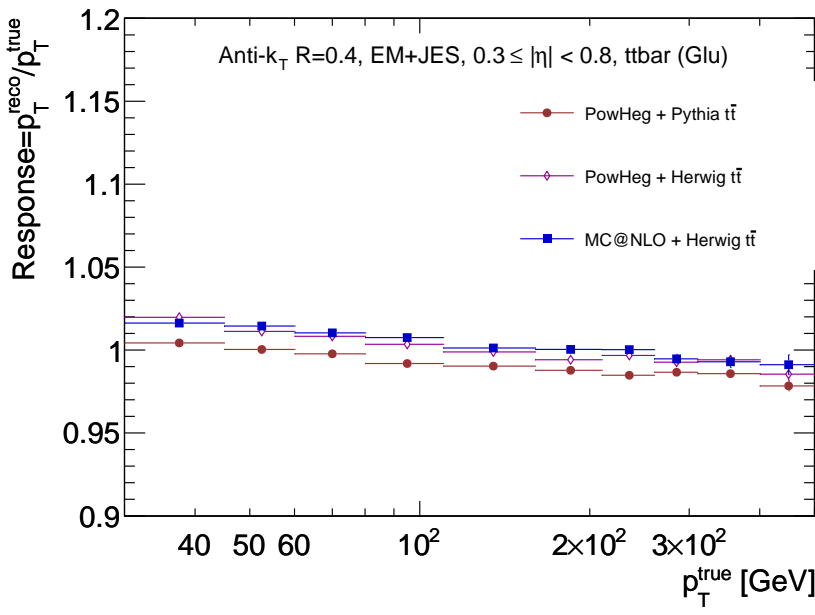
Figure A.23.: Jet response of gluon labelled jets in *tt̄* events for different choices of the Monte-Carlo generator and parton shower program for jets with $0.3 \leq |\eta| < 0.8$. The comparison only includes fast simulation samples.
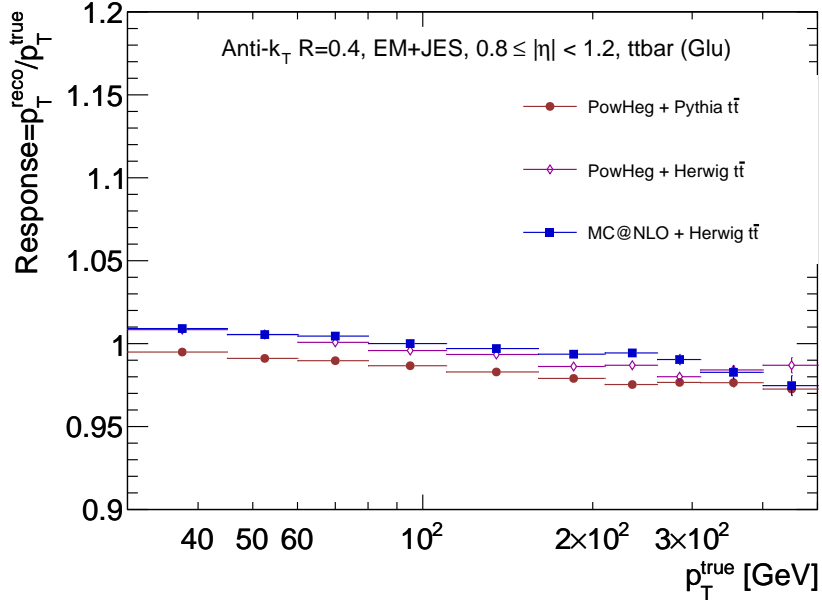
Figure A.24.: Jet response of gluon labelled jets in $t\bar{t}$ events for different choices of the Monte-Carlo generator and parton shower program for jets with $0.8 \le |\eta| < 1.2$. The comparison only includes fast simulation samples.
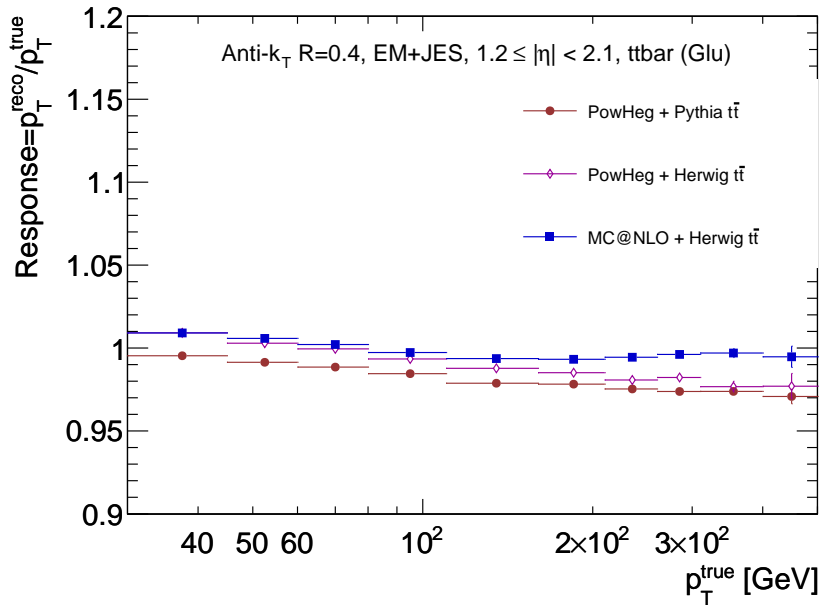
Figure A.25.: Jet response of gluon labelled jets in $t\bar{t}$ events for different choices of the Monte-Carlo generator and parton shower program for jets with $1.2 \le |\eta| < 2.1$. The comparison only includes fast simulation samples.
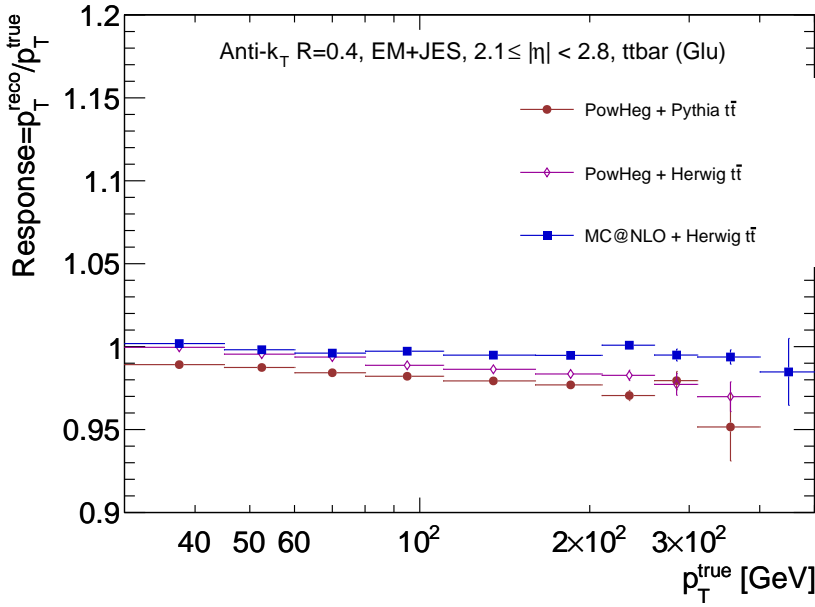
Figure A.26.: Jet response of gluon labelled jets in *tt̄* events for different choices of the Monte-Carlo generator and parton shower program for jets with 2.1 ≤ |η| < 2.8. The comparison only includes fast simulation samples.
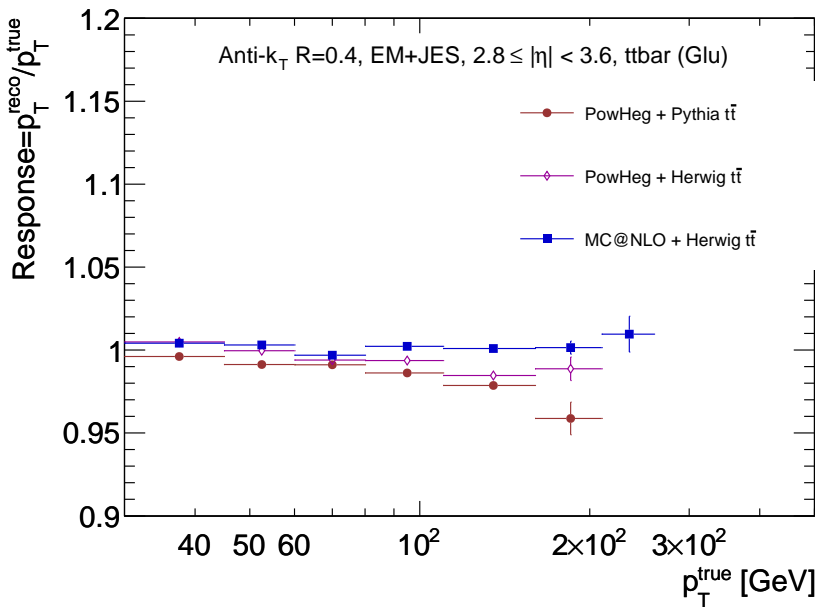
Figure A.27.: Jet response of gluon labelled jets in *tt̄* events for different choices of the Monte-Carlo generator and parton shower program for jets with 2.8 ≤ |η| < 3.6. The comparison only includes fast simulation samples.
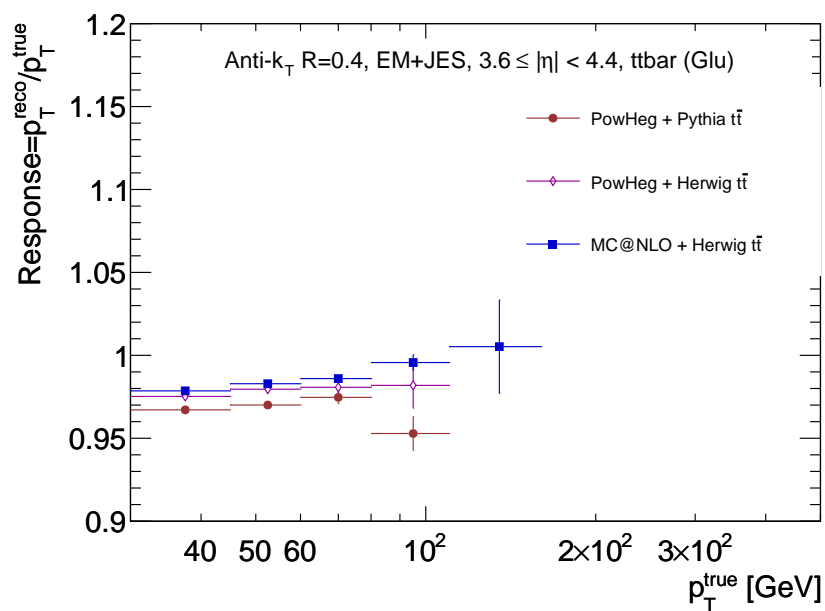
Figure A.28.: Jet response of gluon labelled jets in $t\bar{t}$ events for different choices of the Monte-Carlo generator and parton shower program for jets with $3.6 \leq |\eta| < 4.4$. The comparison only includes fast simulation samples.

B. Background correlation plots
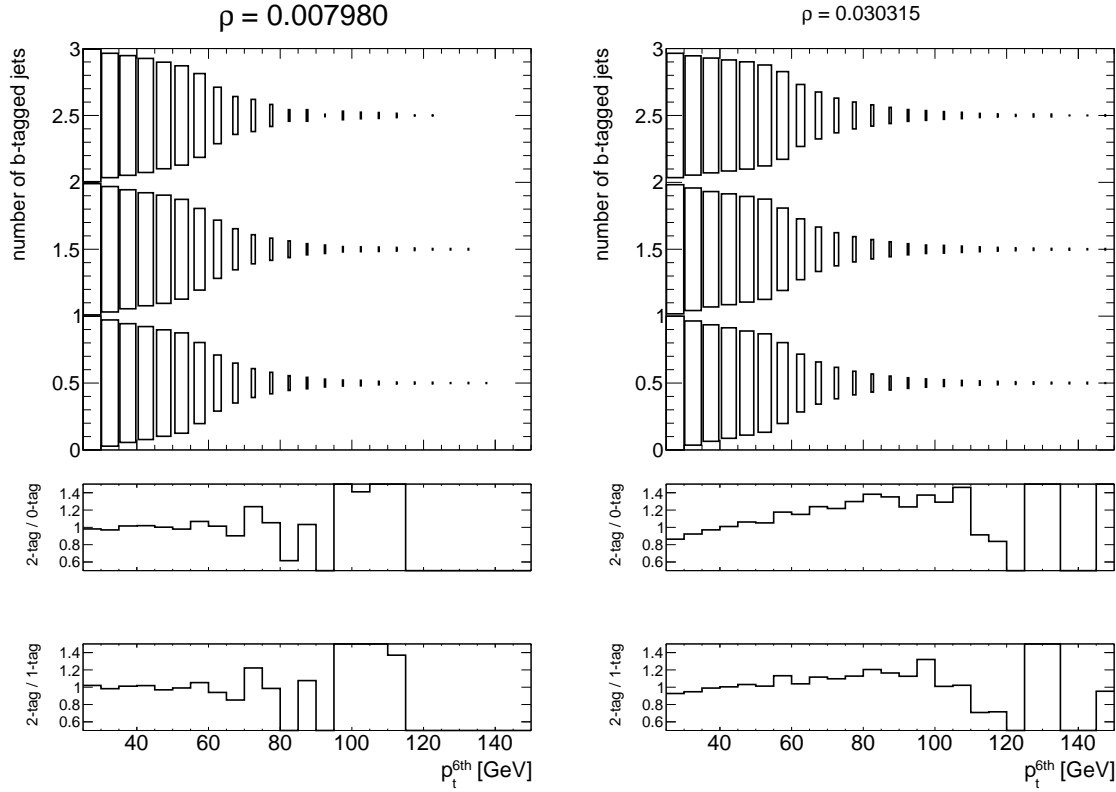
Figure B.1.: p_T distributions of the 6th leading jet - normalised for each *b*-tag multiplicity bin. The *b*-tag multiplicity has been evaluated considering only the four leading jets (left) and considering all jets (right). Also shown are the ratios of the p_T distribution in the 2-tag bin with respect to the 0-tag bin and the 2-tag bin with respect to the 1-tag bin. Even though the correlation coefficients are small in both cases not restricting the *b*-jet multiplicity to the four leading jets results in a raising slope in the ratio plots as larger p_T values are favoured in the higher *b*-tag multiplicity bins. The final set of selection criteria used for the top mass analysis was applied to the data sample.
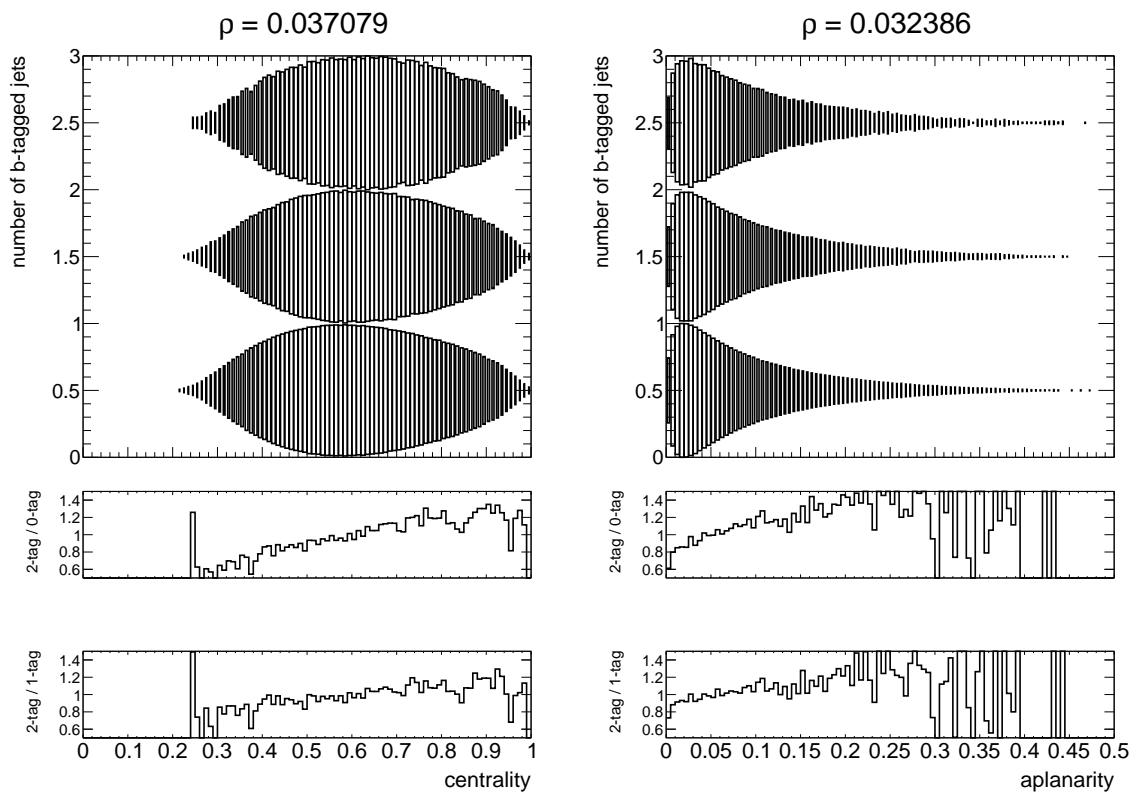
Figure B.2.: Centrality (left) and aplanarity (right) - normalised for each *b*-tag multiplicity bin. Also shown are the ratios of the distributions in the 2-tag bin with respect to the 0-tag bin and the 2-tag bin with respect to the 1-tag bin. Both distributions show a raising slope in the ratio plots.

C. Ensemble test results

(a) $m_{top}^{in,MC}$=165 GeV

(b) $m_{top}^{in,MC}$=167.5 GeV

(c) $m_{top}^{in,MC}$=170 GeV

(d) $m_{top}^{in,MC}$=175 GeV

(e) $m_{top}^{in,MC}$=178 GeV

(f) $m_{top}^{in,MC}$=180 GeV
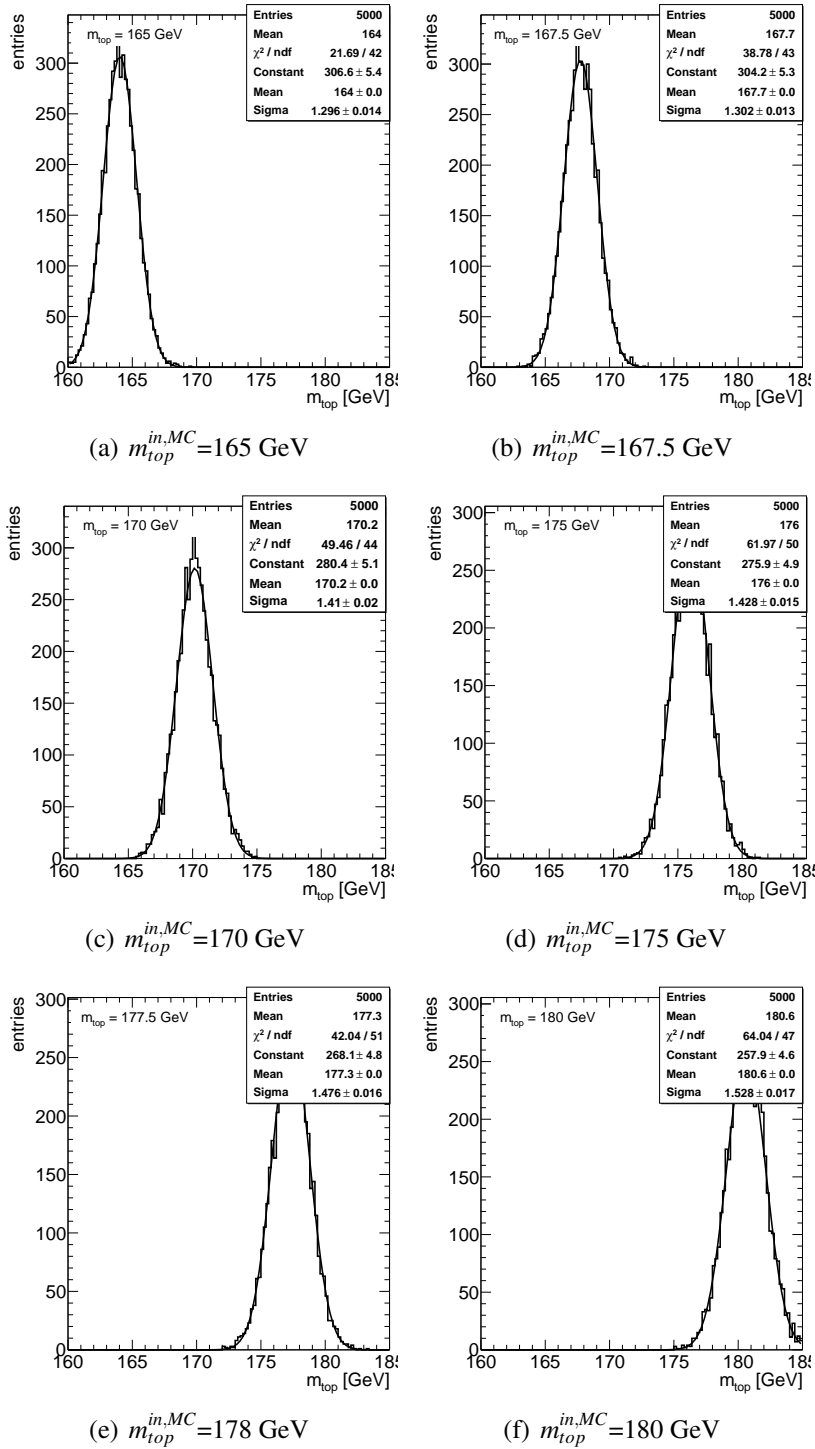
Figure C.1.: Top mass distribution obtained via PEs at 6 different $m_{top}^{in,MC}$ values.

(a) $m_{top}^{in,MC}$=165 GeV

(b) $m_{top}^{in,MC}$=167.5 GeV

(c) $m_{top}^{in,MC}$=170 GeV

(d) $m_{top}^{in,MC}$=175 GeV

(e) $m_{top}^{in,MC}$=177.5 GeV

(f) $m_{top}^{in,MC}$=180 GeV
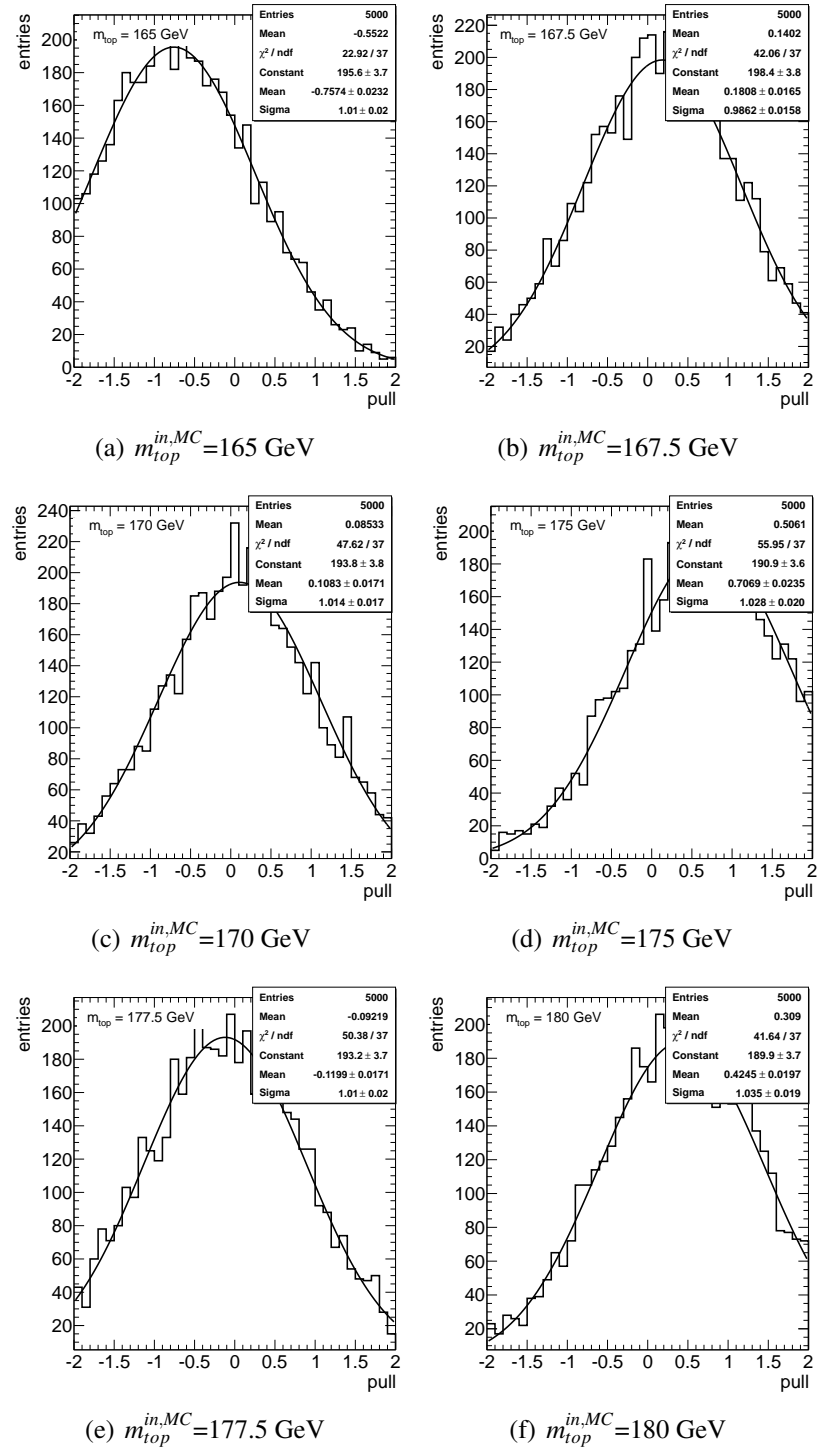
Figure C.2.: Pull distributions obtained via PEs at 6 different $m_{top}^{in,MC}$ values.

(a) $m_{top}^{in,MC}$=165 GeV

(b) $m_{top}^{in,MC}$=167.5 GeV

(c) $m_{top}^{in,MC}$=170 GeV

(d) $m_{top}^{in,MC}$=175 GeV

(e) $m_{top}^{in,MC}$=177.5 GeV

(f) $m_{top}^{in,MC}$=180 GeV
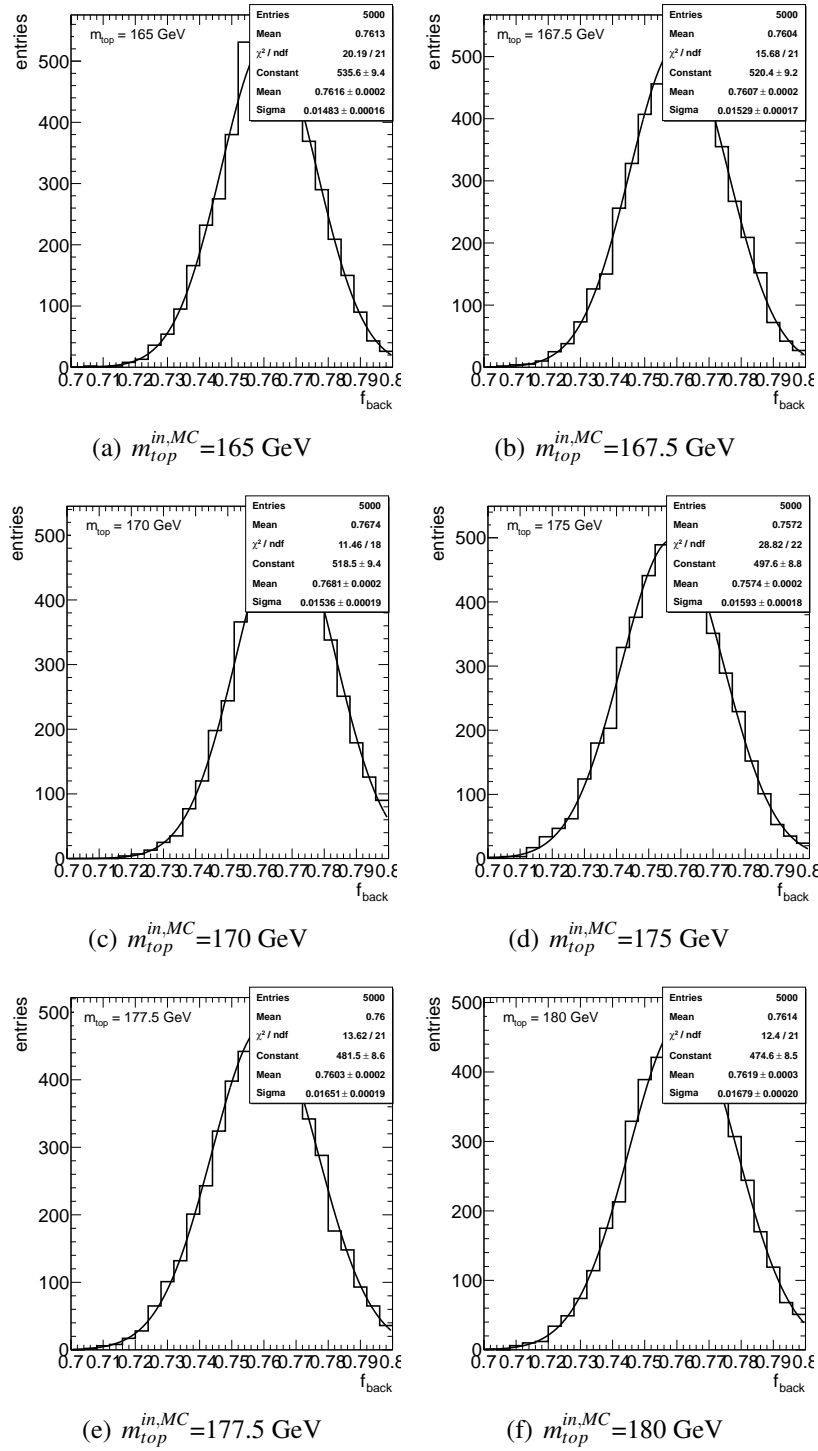
Figure C.3.: Fitted background fraction obtained via PEs at 6 different $m_{top}^{in,MC}$ values.
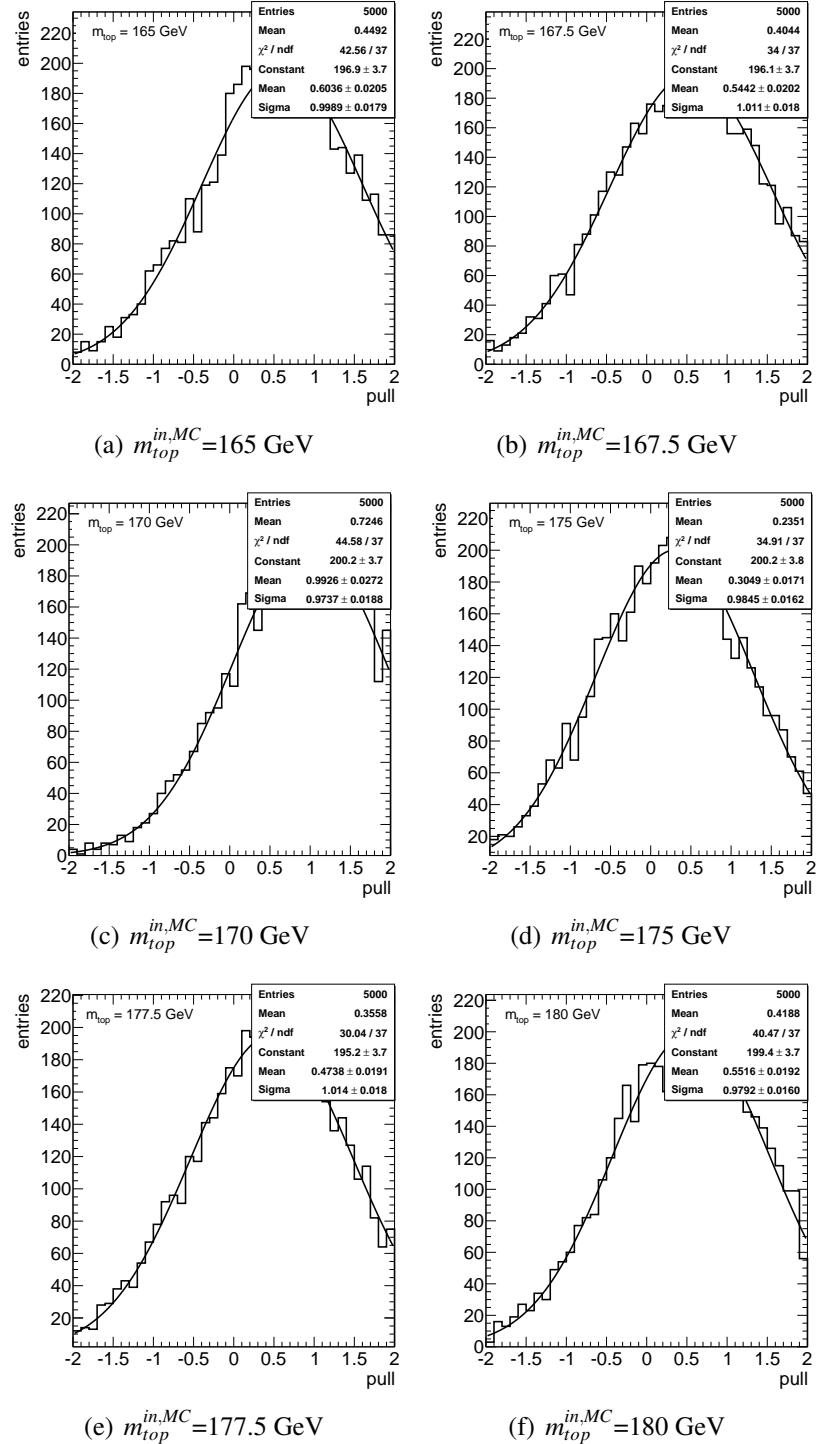
Figure C.4.: Background fraction pull obtained via PEs at 6 different $m_{top}^{in,MC}$ values.

Bibliography

[1] D0 Collaboration, S. Abachi et al., *Observation of the Top Quark*, Phys. Rev. Lett. **74** (Apr, 1995) 2632–2637.
http://link.aps.org/doi/10.1103/PhysRevLett.74.2632.

[2] CDF Collaboration, F. Abe et al., *Observation of Top Quark Production in $\overline{p}p$ Collisions with the Collider Detector at Fermilab*, Phys. Rev. Lett. **74** (Apr, 1995) 2626–2631.
http://link.aps.org/doi/10.1103/PhysRevLett.74.2626.

[3] The ATLAS Collaboration, *Observation of a new particle in the search for the Standard Model Higgs boson with the ATLAS detector at the LHC*, Physics Letters B **716** (2012) no. 1, 1–29. http://www.sciencedirect.com/science/article/pii/S037026931200857X.

[4] The CMS Collaboration, *Observation of a new boson at a mass of 125 GeV with the CMS experiment at the LHC*, Physics Letters B **716** (2012) no. 1, 30–61.
http://www.sciencedirect.com/science/article/pii/S0370269312008581.

[5] S. Alekhin, A. Djouadi, and S. Moch, *The top quark and Higgs boson masses and the stability of the electroweak vacuum*, Phys.Lett. **B716** (2012) 214–219,
arXiv:1207.0980 [hep-ph].

[6] S. Glashow, *Partial Symmetries of Weak Interactions*, Nucl.Phys. **22** (1961) 579–588.

[7] S. Weinberg, *A Model of Leptons*, Phys. Rev. Lett. **19** (Nov, 1967) 1264–1266.
http://link.aps.org/doi/10.1103/PhysRevLett.19.1264.

[8] A. Salam, *Elementary Particle Physics: Relativistic Groups and Analyticity*, Eighth Nobel Symposium (1968) 367.

[9] S. L. Glashow, J. Iliopoulos, and L. Maiani, *Weak Interactions with Lepton-Hadron Symmetry*, Phys. Rev. D **2** (Oct, 1970) 1285–1292.
http://link.aps.org/doi/10.1103/PhysRevD.2.1285.

[10] H. D. Politzer, *Reliable Perturbative Results for Strong Interactions?*, Phys. Rev. Lett. **30** (Jun, 1973) 1346–1349.
http://link.aps.org/doi/10.1103/PhysRevLett.30.1346.

[11] H. D. Politzer, *Asymptotic freedom: An approach to strong interactions*, Physics Reports **14** (1974) no. 4, 129 – 180. `http://www.sciencedirect.com/science/article/pii/0370157374900143`.

[12] D. J. Gross and F. Wilczek, *Ultraviolet Behavior of Non-Abelian Gauge Theories*, Phys. Rev. Lett. **30** (Jun, 1973) 1343–1346. `http://link.aps.org/doi/10.1103/PhysRevLett.30.1343`.

[13] Wikipedia, *Standard Model (Wikipedia, the free encyclopedia)*, Accessed: 2012-05-2. `http://en.wikipedia.org/wiki/Standard_model`.

[14] Particle Data Group Collaboration, J. Beringer et al., *Review of Particle Physics*, Phys. Rev. D **86** (July, 2012) 010001. `http://link.aps.org/doi/10.1103/PhysRevD.86.010001`.

[15] F. Englert and R. Brout, *Broken Symmetry and the Mass of Gauge Vector Mesons*, Phys. Rev. Lett. **13** (Aug, 1964) 321–323. `http://link.aps.org/doi/10.1103/PhysRevLett.13.321`.

[16] P. W. Higgs, *Broken symmetries, massless particles and gauge fields*, Phys.Lett. **12** (1964) 132–133.

[17] P. W. Higgs, *Broken Symmetries and the Masses of Gauge Bosons*, Phys. Rev. Lett. **13** (Oct, 1964) 508–509. `http://link.aps.org/doi/10.1103/PhysRevLett.13.508`.

[18] G. S. Guralnik, C. R. Hagen, and T. W. B. Kibble, *Global Conservation Laws and Massless Particles*, Phys. Rev. Lett. **13** (Nov, 1964) 585–587. `http://link.aps.org/doi/10.1103/PhysRevLett.13.585`.

[19] The ATLAS Collaboration, *Combined measurements of the mass and signal strength of the Higgs-like boson with the ATLAS detector using up to 25 fb^{-1} of proton-proton collision data*, Tech. Rep. ATLAS-CONF-2013-014, CERN, Geneva, Mar, 2013.

[20] S. W. Herb et al., *Observation of a Dimuon Resonance at 9.5 GeV in 400-GeV Proton-Nucleus Collisions*, Phys. Rev. Lett. **39** (Aug, 1977) 252–255. `http://link.aps.org/doi/10.1103/PhysRevLett.39.252`.

[21] A. Quadt, *Top quark physics at hadron colliders*, The European Physical Journal C - Particles and Fields **48** (2006) no. 3, 835–1000. `http://dx.doi.org/10.1140/epjc/s2006-02631-6`.

[22] F.-P. Schilling, *Top Quark Physics at the LHC: A Review of the First Two Years*, Int.J.Mod.Phys. **A27** (2012) 1230016, `arXiv:1206.4484 [hep-ex]`.

[23] J. Pumplin, D. Stump, J. Huston, H. Lai, P. M. Nadolsky, et al., *New generation of parton distributions with uncertainties from global QCD analysis*, JHEP **0207** (2002) 012, `arXiv:hep-ph/0201195 [hep-ph]`.

[24] ATLAS Collaboration, *Measurement of the t-channel single top-quark production cross section in pp collisions at $\sqrt{s}$ = 7 TeV with the ATLAS detector*, Physics Letters B **717** (2012) no. 45, 330 – 350. `http://www.sciencedirect.com/science/article/pii/S0370269312009781`.

[25] *Search for s-Channel Single Top-Quark Production in pp Collisions at $\sqrt{s}$ = 7 TeV*, Tech. Rep. ATLAS-CONF-2011-118, CERN, Geneva, Aug, 2011. `https://cds.cern.ch/record/1376410`.

[26] ATLAS Collaboration, *Evidence for the associated production of a W boson and a top quark in ATLAS at $\sqrt{s}$ = 7 TeV*, Physics Letters B **716** (2012) no. 1, 142 – 159. `http://www.sciencedirect.com/science/article/pii/S0370269312008489`.

[27] P. Z. Skands and D. Wicke, *Non-perturbative QCD effects and the top mass at the Tevatron*, Eur.Phys.J. **C52** (2007) 133–140, `arXiv:hep-ph/0703081 [HEP-PH]`.

[28] D0 Collaboration, V. M. Abazov et al., *Determination of the pole and MSbar masses of the top quark from the $t\bar{t}$ cross section*, Phys.Lett. **B703** (2011) 422–427, `arXiv:1104.2887 [hep-ex]`.

[29] G. Brianti, *Status report on the CERN large hadron collider (LHC)*, Tech. Rep. CERN-LHC-Note-194. LHC-NOTE-194, CERN, Geneva, 1992. `http://cds.cern.ch/record/1019452`.

[30] C. Lefevre, *LHC: the guide (English version)*, Feb, 2009. `http://cds.cern.ch/record/1165534`.

[31] ALICE Collaboration, *ALICE: Technical proposal for a Large Ion collider Experiment at the CERN LHC*. LHC Tech. Proposal. CERN, Geneva, 1995. `http://cds.cern.ch/record/293391`.

[32] LHCb Collaboration, *LHCb : Technical Proposal*. Tech. Proposal. CERN, Geneva, 1998. `http://cds.cern.ch/record/622031`.

[33] CMS Collaboration, *CMS Physics: Technical Design Report Volume 1: Detector Performance and Software*. Technical Design Report CMS. CERN, Geneva, 2006. `http://cds.cern.ch/record/922757`.

[34] ATLAS Collaboration, G. Aad et al., *Expected Performance of the ATLAS Experiment - Detector, Trigger and Physics*, `arXiv:0901.0512 [hep-ex]`.

[35] *CERN releases analysis of LHC incident*, Accessed: 2012-06-23. `http://press.web.cern.ch/press-releases/2008/10/cern-releases-analysis-lhc-inciden`.

[36] *European Organization of Nuclear Research (Geneve)*, Accessed: 2012-06-23. `http://atlas.ch`.

[37] ATLAS Collaboration, *ATLAS inner detector: Technical Design Report, 1.*
Technical Design Report ATLAS. CERN, Geneva, 1997.
`https://cds.cern.ch/record/331063`.

[38] ATLAS Collaboration, *ATLAS liquid-argon calorimeter: Technical Design
Report.* Technical Design Report ATLAS. CERN, Geneva, 1996.
`https://cds.cern.ch/record/331061`.

[39] ATLAS Collaboration, *Readiness of the ATLAS liquid argon calorimeter for LHC
collisions*, European Physical Journal C **70** (Dec., 2010) 723–753,
`arXiv:0912.2642 [physics.ins-det]`.

[40] H. Wilkens and the ATLAS LArg Collaboration, *The ATLAS Liquid Argon
calorimeter: An overview*, Journal of Physics: Conference Series **160** (2009)
no. 1, 012043.
`http://stacks.iop.org/1742-6596/160/i=1/a=012043`.

[41] ATLAS Collaboration, *Readiness of the ATLAS Tile Calorimeter for LHC
collisions*, Eur. Phys. J. C **70** (Jul, 2010) 1193–1236. 64 p.
`https://cds.cern.ch/record/1282535`.

[42] ATLAS Collaboration, *ATLAS tile calorimeter: Technical Design Report.*
Technical Design Report ATLAS. CERN, Geneva, 1996.
`https://cds.cern.ch/record/331062`.

[43] ATLAS Collaboration, *ATLAS muon spectrometer: Technical Design Report.*
Technical Design Report ATLAS. CERN, Geneva, 1997.
`https://cds.cern.ch/record/331068`.

[44] ATLAS Collaboration, *Commissioning of the ATLAS Muon Spectrometer with
cosmic rays*, The European Physical Journal C **70** (2010) no. 3, 875–916.
`http://dx.doi.org/10.1140/epjc/s10052-010-1415-2`.

[45] M. Elsing, T. Schrner-Sadenius, et al., *Configuration of the ATLAS Trigger System
062*, Tech. Rep. ATL-DAQ-2003-038, CERN, Geneva, Mar, 2003.
`https://cds.cern.ch/record/681597`.

[46] *ATLAS Internal Documentation*, Accessed: 2012-06-23. `https://twiki.
cern.ch/twiki/bin/viewauth/Atlas/TriggerForDummies`.

[47] *ATLAS Internal Documentation*, Accessed: 2012-06-23.
`https://atlas-lumicalc.cern.ch/`.

[48] *ATLAS Internal Documentation*, Accessed: 2012-06-23.
`https://twiki.cern.ch/twiki/bin/viewauth/
AtlasProtected/TopCommonObjects2011`.

[49] ATLAS Collaboration, *Electron performance measurements with the ATLAS detector using the 2010 LHC proton-proton collision data*, The European Physical Journal C **72** (2012) no. 3, .
http://dx.doi.org/10.1140/epjc/s10052-012-1909-1.

[50] ATLAS Collaboration, *Muon reconstruction efficiency in reprocessed 2010 LHC proton-proton collision data recorded with the ATLAS detector*, Tech. Rep. ATLAS-CONF-2011-063, CERN, Geneva, Apr, 2011.
https://cds.cern.ch/record/1345743.

[51] B. Resende, *Muon identification algorithms in ATLAS*, Tech. Rep. ATL-PHYS-PROC-2009-113, CERN, Geneva, Sep, 2009.
https://cds.cern.ch/record/1209632/.

[52] *ATLAS Internal Documentation*, Accessed: 2012-06-23.
https://twiki.cern.ch/twiki/bin/viewauth/
AtlasProtected/MCPAnalysisGuidelinesRel17MC11a.

[53] ATLAS Internal Documentation, *Object selection and calibration, background estimations and MC samples for the Summer 2012 Top Quark analyses with 2011 data*, Tech. Rep. ATL-COM-PHYS-2012-499, CERN, Geneva, May, 2012.
https://cds.cern.ch/record/1447086.

[54] ATLAS Collaboration, G. Aad et al., *Performance of Missing Transverse Momentum Reconstruction in Proton-Proton Collisions at 7 TeV with ATLAS*, Eur.Phys.J. **C72** (2012) 1844, arXiv:1108.5602 [hep-ex].

[55] M. Cacciari, G. P. Salam, and G. Soyez, *The Anti-k(t) jet clustering algorithm*, JHEP **0804** (2008) 063, arXiv:0802.1189 [hep-ph].

[56] C. Cojocaru et al., *Hadronic calibration of the ATLAS liquid argon end-cap calorimeter in the pseudorapidity region in beam tests*, Nuclear Instruments and Methods in Physics Research Section A: Accelerators, Spectrometers, Detectors and Associated Equipment **531** (2004) no. 3, 481 – 514.
http://www.sciencedirect.com/science/article/pii/
S0168900204012884.

[57] W. Lampl, S. Laplace, D. Lelas, P. Loch, H. Ma, S. Menke, S. Rajagopalan, D. Rousseau, S. Snyder, and G. Unal, *Calorimeter Clustering Algorithms: Description and Performance*, Tech. Rep. ATL-LARG-PUB-2008-002. ATL-COM-LARG-2008-003, CERN, Geneva, Apr, 2008.
https://cdsweb.cern.ch/record/1099735.

[58] G. P. Salam and G. Soyez, *A Practical Seedless Infrared-Safe Cone jet algorithm*, JHEP **0705** (2007) 086, arXiv:0704.0292 [hep-ph].

[59] M. Martinez, *CDF at IFAE*, Accessed: 2012-06-23.
www-cdf.fnal.gov/ifae/ifae_1year.ppt.

[60] E. Abat et al., *Combined performance studies for electrons at the 2004 ATLAS combined test-beam*, Journal of Instrumentation **5** (2010) no. 11, P11006. http://stacks.iop.org/1748-0221/5/i=11/a=P11006.

[61] ATLAS Collaboration, *Jet energy scale and its systematic uncertainty in proton-proton collisions at $\sqrt{s} = 7$ TeV with ATLAS 2011 data*, Tech. Rep. ATLAS-CONF-2013-004, CERN, Geneva, Jan, 2013. https://cds.cern.ch/record/1509552.

[62] ATLAS Collaboration, *Probing the measurement of jet energies with the ATLAS detector using Z+jet events from proton-proton collisions at $\sqrt{s} = 7$ TeV*, Tech. Rep. ATLAS-CONF-2012-053, CERN, Geneva, May, 2012. https://cds.cern.ch/record/1452641.

[63] ATLAS Collaboration, *Probing the measurement of jet energies with the ATLAS detector using photon+jet events in proton-proton collisions at $\sqrt{s} = 7$ TeV*, Tech. Rep. ATLAS-CONF-2012-063, CERN, Geneva, Jul, 2012. https://cds.cern.ch/record/1459528.

[64] ATLAS Collaboration, *Selection of jets produced in proton-proton collisions with the ATLAS detector using 2011 data*, Tech. Rep. ATLAS-CONF-2012-020, CERN, Geneva, Mar, 2012. https://cds.cern.ch/record/1430034.

[65] ATLAS Collaboration, *Commissioning of the ATLAS high-performance b-tagging algorithms in the 7 TeV collision data*, Tech. Rep. ATLAS-CONF-2011-102, CERN, Geneva, Jul, 2011. https://cds.cern.ch/record/1369219.

[66] ATLAS Collaboration, *Measuring the b-tag efficiency in a top-pair sample with 4.7 $fb^{-}1$ of data from the ATLAS detector*, Tech. Rep. ATLAS-CONF-2012-097, CERN, Geneva, Jul, 2012. https://cds.cern.ch/record/1460443.

[67] ATLAS Collaboration, *Measurement of the b-tag Efficiency in a Sample of Jets Containing Muons with 5 fb1 of Data from the ATLAS Detector*, Tech. Rep. ATLAS-CONF-2012-043, CERN, Geneva, Mar, 2012. https://cds.cern.ch/record/1435197.

[68] ATLAS Collaboration, *b-jet tagging calibration on c-jets containing D^{*+} mesons*, Tech. Rep. ATLAS-CONF-2012-039, CERN, Geneva, Mar, 2012. https://cds.cern.ch/record/1435193.

[69] ATLAS Collaboration, *Measurement of the Mistag Rate with 5 fb^{1} of Data Collected by the ATLAS Detector*, Tech. Rep. ATLAS-CONF-2012-040, CERN, Geneva, Mar, 2012. https://cds.cern.ch/record/1435194.

[70] D0 Collaboration, *Observation of Single Top Quark Production*, Accessed: 2012-06-23. http://www-d0.fnal.gov/Run2Physics/top/singletop_observation/.

[71] ATLAS Collaboration, *Non-collision backgrounds as measured by the ATLAS detector during the 2010 proton-proton run*, Tech. Rep. ATLAS-CONF-2011-137, CERN, Geneva, Sep, 2011. `https://cds.cern.ch/record/1383840`.

[72] ATLAS Collaboration, *Data-Quality Requirements and Event Cleaning for Jets and Missing Transverse Energy Reconstruction with the ATLAS Detector in Proton-Proton Collisions at a Center-of-Mass Energy of $\sqrt{s} = 7$ TeV*, Tech. Rep. ATLAS-CONF-2010-038, CERN, Geneva, Jul, 2010. `https://cds.cern.ch/record/1277678`.

[73] ATLAS Collaboration, *Performance of the ATLAS Jet Trigger in the Early $\sqrt{s} = 7$ TeV Data*, Tech. Rep. ATLAS-CONF-2010-094, CERN, Geneva, Oct, 2010. `https://cdsweb.cern.ch/record/1299109`.

[74] I. Hristova, *The evolution and performance of the ATLAS calorimeter-based triggers in 2011 and 2012*, Tech. Rep. ATL-DAQ-PROC-2012-051, CERN, Geneva, Oct, 2012. `https://cds.cern.ch/record/1485638`.

[75] P. Conde Muino, *Performance and Improvements of the ATLAS Jet Trigger System*, Tech. Rep. ATL-DAQ-PROC-2012-047, CERN, Geneva, Aug, 2012. `https://cds.cern.ch/record/1473115`.

[76] ATLAS Collaboration, G. Aad et al., *Search for new phenomena in final states with large jet multiplicities and missing transverse momentum using $\sqrt{s} = 7$ TeV pp collisions with the ATLAS detector*, JHEP **1111** (2011) 099, `arXiv:1110.2299 [hep-ex]`.

[77] ATLAS Collaboration, *Measurement of the $t\bar{t}$ production cross section in the all-hadronic channel in ATLAS with $\sqrt{s} = 7$ TeV data*, Tech. Rep. ATLAS-CONF-2012-031, CERN, Geneva, Mar, 2012. `https://cds.cern.ch/record/1432196`.

[78] S. Frixione, P. Nason, and C. Oleari, *Matching NLO QCD computations with Parton Shower simulations: the POWHEG method*, JHEP **0711** (2007) 070, `arXiv:0709.2092 [hep-ph]`.

[79] H.-L. Lai, M. Guzzi, J. Huston, Z. Li, P. M. Nadolsky, et al., *New parton distributions for collider physics*, Phys.Rev. **D82** (2010) 074024, `arXiv:1007.2241 [hep-ph]`.

[80] T. Sjostrand, S. Mrenna, and P. Z. Skands, *PYTHIA 6.4 Physics and Manual*, JHEP **0605** (2006) 026, `arXiv:hep-ph/0603175 [hep-ph]`.

[81] G. Corcella, I. Knowles, G. Marchesini, S. Moretti, K. Odagiri, et al., *HERWIG 6: An Event generator for hadron emission reactions with interfering gluons (including supersymmetric processes)*, JHEP **0101** (2001) 010, `arXiv:hep-ph/0011363 [hep-ph]`.

[82] B. Andersson, G. Gustafson, G. Ingelman, and T. Sjostrand, *Parton fragmentation and string dynamics*, Physics Reports **97** (1983) no. 23, 31 – 145. `http://www.sciencedirect.com/science/article/pii/0370157383900807`.

[83] S. Adomeit, *Hard And Soft QCD Physics In ATLAS*, . `https://cds.cern.ch/record/1478972/files/ATL-PHYS-PROC-2012-200.pdf`.

[84] J. Butterworth, J. R. Forshaw, and M. Seymour, *Multiparton interactions in photoproduction at HERA*, Z.Phys. **C72** (1996) 637–646, `arXiv:hep-ph/9601371 [hep-ph]`.

[85] P. Z. Skands, *Tuning Monte Carlo Generators: The Perugia Tunes*, Phys.Rev. **D82** (2010) 074018, `arXiv:1005.3457 [hep-ph]`.

[86] ATLAS Collaboration, *New ATLAS event generator tunes to 2010 data*, Tech. Rep. ATL-PHYS-PUB-2011-008, CERN, Geneva, Apr, 2011. `https://cds.cern.ch/record/1345343`.

[87] *Geant4a simulation toolkit*, Nuclear Instruments and Methods in Physics Research Section A: Accelerators, Spectrometers, Detectors and Associated Equipment **506** (2003) no. 3, 250 – 303. `http://www.sciencedirect.com/science/article/pii/S0168900203013688`.

[88] *ATLAS Internal Documentation*, Accessed: 2012-06-23. `https://twiki.cern.ch/twiki/bin/viewauth/AtlasProtected/Top2011MCCrossSectionReference`.

[89] M. Aliev, H. Lacker, U. Langenfeld, S. Moch, P. Uwer, et al., *HATHOR: HAdronic Top and Heavy quarks crOss section calculatoR*, Comput.Phys.Commun. **182** (2011) 1034–1046, `arXiv:1007.1327 [hep-ph]`.

[90] A. Martin, W. Stirling, R. Thorne, and G. Watt, *Parton distributions for the LHC*, The European Physical Journal C **63** (2009) no. 2, 189–285. `http://dx.doi.org/10.1140/epjc/s10052-009-1072-5`.

[91] A. Martin, W. Stirling, R. Thorne, and G. Watt, *Uncertainties on α_S in global PDF analyses and implications for predicted hadronic cross sections*, Eur.Phys.J. **C64** (2009) 653–680, `arXiv:0905.3531 [hep-ph]`.

[92] M. Cacciari, M. Czakon, M. Mangano, A. Mitov, and P. Nason, *Top-pair production at hadron colliders with next-to-next-to-leading logarithmic soft-gluon resummation*, Phys.Lett. **B710** (2012) 612–622, `arXiv:1111.5869 [hep-ph]`.

[93] M. Czakon and A. Mitov, *Top++: a program for the calculation of the top-pair cross-section at hadron colliders*, `arXiv:1112.5675 [hep-ph]`.

[94] *ATLAS Internal Documentation*, Accessed: 2012-06-23.
`https://twiki.cern.ch/twiki/bin/viewauth/`
`AtlasProtected/ExtendedPileupReweighting`.

[95] J. Erdmann, K. Kroeninger, O. Nackenhorst, and A. Quadt, *Kinematic fitting of ttbar-events using a likelihood approach: The KLFitter package*, Tech. Rep. ATL-COM-PHYS-2009-551, CERN, Geneva, Sep, 2009.

[96] F. Beaujean, A. Caldwell, D. Kollar, and K. Kroninger, *BAT: The Bayesian analysis toolkit*, J.Phys.Conf.Ser. **331** (2011) 072040.

[97] R. Barlow, *Application of the bootstrap resampling technique to particle physics experiments*, Manchester University Preprint, MAN/HEP/99/4 (1999). `https: //www.hep.manchester.ac.uk/preprints/manhep99-4.ps`.

[98] S. Frixione and B. R. Webber, *Matching NLO QCD computations and parton shower simulations*, JHEP **0206** (2002) 029, `arXiv:hep-ph/0204244 [hep-ph]`.

[99] S. Frixione, P. Nason, and B. R. Webber, *Matching NLO QCD and parton showers in heavy flavor production*, JHEP **0308** (2003) 007, `arXiv:hep-ph/0305252 [hep-ph]`.

[100] B. P. Kersevan and E. Richter-Was, *The Monte Carlo event generator AcerMC version 2.0 with interfaces to PYTHIA 6.2 and HERWIG 6.5*, `arXiv:hep-ph/0405247 [hep-ph]`.

[101] ATLAS Collaboration, G. Aad et al., *Measurement of $t\bar{t}$ production with a veto on additional central jet activity in pp collisions at $\sqrt{s} = 7$ TeV using the ATLAS detector*, Eur.Phys.J. **C72** (2012) 2043, `arXiv:1203.5015 [hep-ex]`.

[102] CTEQ Collaboration Collaboration, H. Lai et al., *Global QCD analysis of parton structure of the nucleon: CTEQ5 parton distributions*, Eur.Phys.J. **C12** (2000) 375–392, `arXiv:hep-ph/9903282 [hep-ph]`.

[103] ATLAS Collaboration, *Measurement of the top quark mass with the template method in the $t\bar{t} \rightarrow$ lepton + jets channel using ATLAS data*, The European Physical Journal C **72** (2012) no. 6, .
`http://dx.doi.org/10.1140/epjc/s10052-012-2046-6`.

[104] ATLAS Collaboration, *Jet energy measurement and systematic uncertainties using tracks for jets and for b-quark jets produced in proton-proton collisions at $\sqrt{s} = 7$ TeV in the ATLAS detector*, Tech. Rep. ATLAS-CONF-2013-002, CERN, Geneva, Jan, 2013. `https://cds.cern.ch/record/1504739`.

[105] ATLAS Collaboration, *Jet energy resolution in proton-proton collisions at $\sqrt{s} = 7$ TeV recorded in 2010 with the ATLAS detector*, The European Physical Journal C **73** (2013) no. 3, .
`http://dx.doi.org/10.1140/epjc/s10052-013-2306-0`.

[106] ATLAS Collaboration Collaboration, G. Aad et al., *Jet energy measurement with the ATLAS detector in proton-proton collisions at $\sqrt{s} = 7$ TeV*, Eur.Phys.J. **C73** (2013) 2304, `arXiv:1112.6426 [hep-ex]`.

[107] ATLAS Collaboration, *Light-quark and Gluon Jets: Calorimeter Response, Jet Energy Scale Systematics and Properties*, Tech. Rep. ATLAS-CONF-2012-138, CERN, Geneva, Sep, 2012. `https://cds.cern.ch/record/1480629`.

[108] M. Bahr, S. Gieseke, M. Gigg, D. Grellscheid, K. Hamilton, et al., *Herwig++ Physics and Manual*, Eur.Phys.J. **C58** (2008) 639–707, `arXiv:0803.0883 [hep-ph]`.

[109] G. P. Salam, *Infrared safe definition of jet flavour*, `arXiv:hep-ph/0605270 [hep-ph]`.

[110] CDF Collaboration, *Measurement of the Top Quark Mass in the All-Hadronic Mode at CDF*, Phys.Lett. **B714** (2012) 24–31, `arXiv:1112.4891 [hep-ex]`.

[111] CMS Collaboration, *Measurement of the top-quark mass in all-jets final states*, Tech. Rep. CMS-PAS-TOP-11-017, CERN, Geneva, 2012. `https://cds.cern.ch/record/1477721/`.

[112] ATLAS Collaboration, *Measurement of the Top Quark Mass from $\sqrt{s} = 7$ TeV ATLAS Data using a 3-dimensional Template Fit*, Tech. Rep. ATLAS-CONF-2013-046, CERN, Geneva, May, 2013. `https://cds.cern.ch/record/1547327`.

List of Figures

Acknowledgements

First of all I would like to thank my Doktorvater Otmar Biebel – for the opportunity to write this thesis and the freedom in choosing which way to go for the analysis but also for his advice and guidance when needed. Special thanks for all the patience, for not losing confidence in my work and all the encouraging words in moments when I got stuck and was close to giving up. I am grateful for all the support without which there would not be a working background model up to now and which helped me to make it through the last rather stressful weeks of thesis writing.

I would like to thank Wolfgang Dünnweber for agreeing to write the second review of my thesis.

A huge thank you goes to Dorothee Schaile for giving me the opportunity to spend 8 months at CERN as well as for her valuable advice throughout the last three years.

To my (present and former) colleagues in Munich – for the opportunity to work within a wonderful group of people and providing help whenever needed. Special thanks goes to: Sebastian Becker - who appeared at exactly the same day in the group as I - for walking the long way from the very first diploma student moments to finishing the PhD thesis in parallel. Alexander Ruschke for being the bridge over troubled water when I lost confidence in me finishing my thesis. Johannes Elmsheuser for always trying to make me calm down when I got into panic (nearly every day?). The Sendling (=best place to live in Munich) people - Bonnie Chow, Johannes Ebke and Jonas Will - for the common ice cream, cooking and U-Bahn travelling sessions. To my co-top quark PhD student Christopher Schmitt - thanks for turning on the heating in my office when I came back from CERN. Thanks also to Julien de Graat, Markus Lichtnecker, Christian Meineck, Thomas Müller, Tobias Verlage, Josipa Vujaklija and Josephine Wittkowski for a great time in Munich.

Special thanks go to the hardware group in Munich: To Ralf Hertenberger for all the things he taught me when I was still working on my diploma thesis and from which I keep benefitting. Thanks to Ralf and the remaining members of the group – specifically Albert Engl, Alex Ruschke, André Zibell, David Heereman and Jona Bortfeldt for giving me the feeling that I am still part of the group even after moving from muons to top quarks.

A big thank you goes to my officemates - for managing to share their time at work with a 'not-so-easy' person together in one room: Albert Engl, Christina Galea (thanks for coming back and encouraging me a couple of days before my defence), Jeanette Lorenz (a big thank you for bringing chocolate from each and every "Dienstreise"), Alexander

work - but still making sure there'd always be the traditional bowl of potato salad on the table when I finally found my way back home. Thanks to Ines - for being the best sister I could think of.